別添

Magn Reson Med Sci
doi:10.2463/mrms.mp.2020-0084 Published Online: November 26, 2020

MAJOR PAPER

A National Survey on Safety Management at MR Imaging Facilities in Japan

Minako Azuma[1], Kanako K. Kumamaru[2], Toshinori Hirai[1*], Zaw Aung Khant[1], Ritsuko Koba[2,3], Shinpei Ijichi[2,4], Masahiro Jinzaki[5], Sadayuki Murayama[6], and Shigeki Aoki[2]

Purpose: To investigate safety management at Japanese facilities performing human MRI studies.

Materials and Methods: All Japanese facilities performing human MRI studies were invited to participate in a comprehensive survey that evaluated their MRI safety management. The survey used a questionnaire prepared with the cooperation of the Safety Committee of the Japanese Society for Magnetic Resonance in Medicine. The survey addressed items pertaining to the overall MRI safety management, questions on the occurrence of incidents, and questions specific to facility and MRI scanner or examination. The survey covered the period from October 2017 to September 2018. Automated machine learning was used to identify factors associated with major incidents.

Results: Of 5914 facilities, 2015 (34%) responded to the questionnaire. There was a wide variation in the rate of compliance with MRI safety management items among the participating facilities. Among the facilities responding to this questionnaire, 5% reported major incidents and 27% reported minor incidents related to MRI studies. Most major incidents involved the administration of contrast agents. The most influential factor in major incidents was the total number of MRI studies performed at the facility; this number was significantly correlated with the risk of major incidents ($P < 0.0001$).

Conclusion: There were large variations in the safety standards applied at Japanese facilities performing clinical MRI studies. The total number of MRI studies performed at a facility affected the number of major incidents.

Keywords: *accident, examination, magnetic resonance imaging, safety*

Introduction

Diagnostic MRI is used worldwide. The number of MRI units in Japan is about 7 times the global average, and the ratio of MRI scanners to the population is the highest in the world[1]. MRI presents safety risks associated with large static and changing magnetic fields, high-powered RF coil systems, and exogenous contrast agents[2–7]. Diagnosticians must be alert to these risks and their mitigations in order to protect their patients, themselves, and their colleagues from the avoidable harm. Consequently, strict compliance with safety regulations is required[2–7].

In 2014, the Safety Committee of the Japanese Society for Magnetic Resonance in Medicine (JSMRM) issued the second edition of "MRI Safety Principles, Standards and Clinical Concerns"[8]. However, it remained unknown how well the promulgated safety management standards were applied at Japanese MRI facilities. Therefore, we aimed to investigate safety management at facilities performing human MRI studies in Japan.

Materials and Methods

Facilities surveyed

All medical facilities in Japan with MRI equipment were invited to participate in a survey that evaluated their compliance with MRI safety standards. A list of these facilities was obtained from the website of the Ministry of Health, Labour and Welfare (https://www.mhlw.go.jp/stf/seisakunitsuite/bunya/kenkou_iryou/iryou/teikyouseido/index.html). A Japanese medical

[1]Department of Radiology, Faculty of Medicine, University of Miyazaki, Miyazaki, Miyazaki, Japan
[2]Department of Radiology, Graduate School of Medicine, Juntendo University, Tokyo, Japan
[3]Varian Medical Systems K.K., Tokyo, Japan
[4]DataRobot Inc., Tokyo, Japan
[5]Department of Radiology, Keio University School of Medicine, Tokyo, Japan
[6]Department of Radiology, Graduate School of Medical Science, University of the Ryukyu, Okinawa, Japan
*Corresponding author: Department of Diagnostic Radiology, Faculty of Life Sciences, Kumamoto University,
1-1-1, Honjo, Chuo-ku, Kumamoto 860-8556, Japan
Phone: +81-96-373-5258, Fax: +81-96-373-5342,
E-mail: t-hirai@kumamoto-u.ac.jp

Received: June 5, 2020 | Accepted: September 6, 2020

journal[9] was referred to identify the MRI scanners. Facilities whose addresses were unknown and facilities that had sold their MRI equipment were excluded. The total number of facilities invited to participate in the survey was 5914.

Questionnaire

Our survey questionnaire was prepared with the cooperation of the JSMRM. It included items specific to MRI safety management (Tables 1–5) and questions pertaining to the occurrence of major and minor incidents (Table 6). The questionnaire also contained information regarding the type of facility that hosted MRI equipment, MRI scanners, average time for 1 MRI examination, number of MRI studies, and personnel (Figs. 1–7).

Survey period and method

The survey covered the period from October 2017 to September 2018. On November 5, 2018, the survey questionnaires were sent by regular mail or by e-mail to 5914 facilities. Each survey packet sent by regular mail included a prepaid return envelope. Questionnaires sent by e-mail included commercially available Google forms (docs.google.com/forms); responses were collected electronically. The deadline for submitting the responses was November 30, 2018. Survey reminders were sent a few days before the deadline.

Statistical analysis

It was difficult to adopt conventional multivariate statistical methods because this study handled many types of questions including multiple-choice questions. Therefore, before conducting the survey, these survey questionnaires were designed to apply a machine learning analysis model. To adequately perform accurate statistical analysis for items with many variables, the variables in 7 questions were consolidated. To identify the factors associated with MRI-related major incidents that had affected the patient's health, the DataRobot enterprise artificial intelligence (AI) platform (DataRobot Automated Machine Learning version 6.0; DataRobot, Tokyo, Japan) was used to create machine learning models. The AI platform provides a method to create a more robust and accurate ensemble model by combining independent models created from multiple independent algorithms. The relative importance of a variable to the ensemble model was assessed using permutation importance as described by Breiman[10]. On the DataRobot platform, the following 5 steps were performed automatically:

1. The random seed controlling the random sampling condition in cross-validation (CV) partitioning was changed 10 times to run the "autopilot" 10 times.
2. Each time on autopilot, 7-fold CV was conducted with a 0% holdout. (Partitioning employs stratified extraction so that the ratio of true/false is the same for all folds.)
3. For model creation, hyperparameters were optimized; preprocessing and algorithm application were performed automatically.
4. With each autopilot run (n = 10), multiple ensemble models were generated; single machine learning models with different algorithmic predispositions (e.g., eXtreme gradient-boosted trees, random forest, and regularized regression such as Elastic Net and Neural Networks) were combined. The ensembles also applied various methods such as Average and Generalized Linear Model (GLM).
5. Permutation importance was calculated for the most accurate ensemble models created in step 4. Since going through these steps finally yielded 10 permutation importance values for each explanatory variable, its median value was calculated.

We then performed variable selection to ensure that no explanatory variables with relatively small median values were included in the model and again performed autopilot runs with different random seeds. We repeated the above steps to narrow down the results to only the important variables.

To understand the independent impact of individual variables on major incidents, we constructed a partial dependence plot as described by Friedman[11]. We used Light Gradient Boosted Machine Classifier, a machine learning model based on gradient boosting, to calculate the plotted values. The partial dependence plot can be interpreted as showing the effect of changing a variable in isolation; it demonstrates the relationship between the value of that variable and the probability value of the major incident. For each of the selected items, the risk ratio for major incidents was calculated; to obtain the correlation between two variables, the Pearson correlation coefficient (r) was calculated. Differences of $P < 0.05$ were considered significant.

Results

Of the 5914 medical facilities invited to participate in this survey, 2015 (34%) responded fully or partially to the questions—1923 responded by regular mail and 92 responded by e-mail.

As shown in Fig. 1, of the 2015 survey participants, 1930 (96%) indicated their type of facility—majority were general hospitals with fewer than 200 beds (n = 679, 35%), next were special functioning and regional medical care support hospitals (n = 446, 23%), followed by general hospitals with more than 200 beds (n = 379, 20%). The manufacturer and the magnetic field strength of the MRI scanners are shown in Fig. 2. Of the 2807 scanners in use from October 2017 to September 2018 at the surveyed facilities, 1853 (66%) were 1.5T instruments, 634 (23%) were 3T, and 267 (10%) were <1.5T scanners.

The average time for 1 MRI examination was 30 min at 965 (49%) of 1987 responding facilities and 20 min in 654 (33%) of them (Fig. 3). During the month of September 2018, 570 of 2015 facilities (28%) performed

up to 100 MRI studies, 441 (22%) performed between 100 and 200 examinations, and 312 (15%) performed between 200 and 300 MRI scans. The remaining facilities (n = 692, 34%) performed more than 300 MRI scans in that period (Fig. 4). We found that of 1977 facilities responding to the question regarding the number of MRI-specialized personnel in each facility, 1440 (73%) did not employ MRI-specialized personnel (Fig. 5). No full-time radiologists involved in MRI protocol instructions, scan interpretation, and face-to-face interactions with patients and/or colleagues were on-site in 1096 (57%) of 1921 responding facilities (Fig. 6); 1185 (60%) of 1971 the facilities did not employ part-time radiologists specialized in MRI issues (Fig. 7).

Table 1 Preparation of MRI safety management and manual

Item	Question[a]	Yes	No	MRI not performed[b]
1	Is there an MRI examination management team composed of the responsible doctor, other doctors, radiological technologists, nurses, etc., in the facility? (n = 2009)	256 (13%)	1753 (87%)	NA
2	Does the MRI examination management team hold meetings on safety management at least once a year? (n = 1880)	170 (9%)	1710 (91%)	NA
3	Does the MRI examination management team regularly give lectures to health-care professionals in the facility? (n = 1876)	357 (19%)	1519 (81%)	NA
4	Do you have a manual for safety management system before MRI inspection in the facility? (n = 1994)	1438 (72%)	556 (28%)	NA
5	Is there an operation manual for sedation of claustrophobic patients and is the cooperation with other department doctors established? (n = 2008)	298 (14%)	1710 (86%)	NA
6	Is there an operation manual that includes a communication system for dealing with magnet quench? (n = 1972)	894 (45%)	1078 (55%)	NA
7	Do you have a manual for dealing with disasters such as earthquakes, floods, and power outages? (n = 1994)	1197 (60%)	797 (40%)	NA
8	Is a system established to check for MRI findings requiring urgent action (such as vascular disorders requiring immediate treatment) and to promptly notify the requesting physician? (n = 1999)	1556 (78%)	443 (22%)	NA
9	Is there an operation manual for MRI examination of pregnant women? (n = 1966)	372 (19%)	666 (34%)	928 (47%)
10	For pediatric patients who need sedation, is an emergency backup system and a system for coordinating with other doctors (anesthesiologists, pediatricians, etc.) prepared and trained? (n = 1969)	201 (10%)	637 (32%)	1131 (58%)
11	Does your facility have an operation manual for patients with implantable medical devices (e.g., pacemakers)? (n = 1976)	640 (33%)	139 (7%)	1197 (60%)
12	Is an operation manual, emergency backup system, and a system to cooperate with doctors (emergency doctors, etc.) in other departments established for allergic reactions and extravasation after use of contrast agents in patients? (n = 2001)	1291 (65%)	423 (21%)	287 (14%)
13	Is there an operation manual and training for ensuring the safety of subjects in an emergency? (n = 1996)	359 (18%)	633 (32%)	1004[c] (50%)
14	As a postmarketing safety measure for gadolinium-contrast agents, have you cooperated with the Pharmacy Department to disseminate important information on postuse cautions in the hospital? (n = 1996)	783 (39%)	925 (46%)	288[d] (15%)
15	As a postmarketing safety measure for drugs used during MRI examinations other than gadolinium-contrast agents (ferucarbotran, scopolamine butyl bromide, glucagon, and manganese chloride), have you cooperated with the Pharmacy Department to disseminate important information about the revision of precautions in the hospital? (n = 1992)	604 (30%)	1030 (52%)	358[e] (18%)

Values are the number of facilities. NA, not available.
[a]The number in parentheses shows the number of facilities that responded to the question item.
[b]MRI examination was not performed for certain patients.
[c]There was an operation manual but no training for ensuring the safety of subjects in an emergency.
[d]The measure was not necessary because contrast-enhanced MRI studies had not been performed.
[e]The measure was not necessary because the MRI examination using drugs other than gadolinium-contrast agents had not been performed.

Table 2 Confirmation at the time of MRI examination request

Item	Question[a]	Yes	No
16	Is there a system to check for contraindicated devices when a doctor requests an examination? (n = 2006)	1658 (83%)	348 (17%)

Values are the number of facilities.
[a]The number in parentheses shows the number of facilities that responded to the question item.

Table 3 Confirmation before MRI examination

Item	Question[a]	Yes	No	MRI not performed[b]
17	Does the patient have sufficient information (such as the risk of metal in the body) necessary for safety management before the MRI examination? (n = 2005)	1962 (98%)	43 (2%)	NA
18	Do you check for the presence of patches in the skin (e.g., thermal patch, thermal wear)? (n = 2007)	1986 (99%)	21 (1%)	NA
19	Have you fully explained and understood how to tell the patient to cancel the test (use of emergency call)? (n = 2007)	1975 (98%)	32 (2%)	NA
20	Do you check for renal function and allergies (allergy to contrast agents, bronchial asthma, etc.) before contrast-enhanced MRI? (n = 2002)	1688 (84%)	22 (1%)	292 (15%)
21	Are measures taken to prevent NSF (checking renal function, eGFR, contrast agent dosage, etc.)? (n = 1999)	1567 (79%)	125 (6%)	307 (15%)
22	Have you checked the following information on the questionnaire for safety management before MRI examination? (Multiple answers are allowed.)			
	Implantable medical device	1977 (98%)		
	Magnetic material in the body	1971 (98%)		
	Tattoo	1897 (94%)		
	History of surgery	1845 (92%)		
	Magnetic material outside the body	1683 (84%)		
	Art makeup	1742 (86%)		
	No confirmation	33(2%)		
23	Have you checked the body for magnetic substances before MRI examination? (Multiple answers are allowed.)			
	Checked with metal detector	890 (44%)		
	Checked with magnetic detector	110 (5%)		
	Checked by doctor's interview	1421 (71%)		
	Checked by paramedical interview	1820 (90%)		
	No confirmation	3 (0.1%)		

Values are the number of facilities. eGFR, estimated glomerular filtration rate; NA, not available; NSF, nephrogenic systemic fibrosis.
[a]The number in parentheses shows the number of facilities that responded to the question item.
[b]The measure was not necessary because contrast-enhanced MRI studies had not been performed.

Table 4 Confirmation during MRI examination

Item	Question[a]	Yes	No
24	Is there an observation of heart rate, blood oxygen level, etc., during an MRI examination for patients who need them? (n = 2004)	1407 (70%)	597 (30%)
25	Are you taking measures against noise? (n = 2004)	1707 (85%)	297 (15%)

Values are the number of facilities.
[a]The number in parentheses shows the number of facilities that responded to the question item.

Table 5 MRI inspection and record

Item	Question[a]	Yes	No
26	Do you record and save examination times and imaging protocols? (n = 1996)	894 (45%)	1102 (55%)
27	Do you have a phantom for quality control of MRI equipment? (n = 2005)	1656 (83%)	349 (17%)
28	Have you checked the operation of the emergency stop function of the bed? (n = 2002)	1164 (58%)	838 (42%)
28	Do you record the temperature and humidity in the MRI room? (n = 2009)	789 (39%)	1220 (61%)
30	Do you record the oxygen concentration in the MRI room? (n = 2004)	730 (36%)	1274 (64%)
31	Have you checked the operation of the oxygen concentration monitor in the MRI room? (n = 2003)	1341 (67%)	662 (33%)
32	Do you record the temperature and humidity in the computer room? (n = 2008)	676 (34%)	1332 (66%)
33	Have you checked the operation of the patient emergency call? (n = 2004)	1721 (86%)	283 (14%)
34	Do you regularly perform maintenance inspections (manufacturer inspections or inspections by qualified personnel other than manufacturers)? (n = 1994)		
	At least once every 3 months	927 (46%)	
	At least once every 6 months	853 (43%)	
	At least once a year	94 (5%)	
	At least once every 2 years	14 (<1%)	
	No	35 (2%)	
	Others	71 (4%)	
35	Do you record and store the maintenance inspections in item 34? (n = 2006)		
	Yes	1968 (98%)	
	No	4 (<1 %)	
	No maintenance	34 (2%)	
36	Do you have a maintenance contract for MRI equipment? (n = 1975)		
	Yes	1632 (83%)	
	Inspection only	282 (14%)	
	Others	61 (3%)	
37	Is the MRI machine checked at the start and end of work? (n = 1961)		
	Every day	1663 (85%)	
	Once a week	46 (2%)	
	5 times a week	21 (1%)	
	6 times a week	18 (<1%)	
	Twice a week	10 (<1%)	
	Others	12 (<1%)	
	No	191 (10%)	
38	What are the evaluation items for the phantom scan at the start of the MRI system? (Multiple answers are allowed.)		
	Image artifacts	1175 (58%)	
	Noise	742 (37%)	
	Quantitative image quality	450 (22%)	
	Other items	167 (8%)	
	Unchecked	599 (30%)	

Values are the number of facilities.
[a]The number in parentheses shows the number of facilities that responded to the question item.

Table 6 MRI-related accidents

Item	Question[a]	Yes	No
39	In the past year (October 2017–September 2018), have there been any accidents (major incidents) related to MRI that affect patient health? (n = 1954)	90 (5%)	1864 (95%)
40	In the past year (October 2017–September 2018), have there been any accidents (minor incidents) related to MRI that have not affected the patient's health? (n = 1954)	519 (27%)	1435 (73%)

Values are the number of facilities.
[a]The number in parentheses shows the number of facilities that responded to the question item.

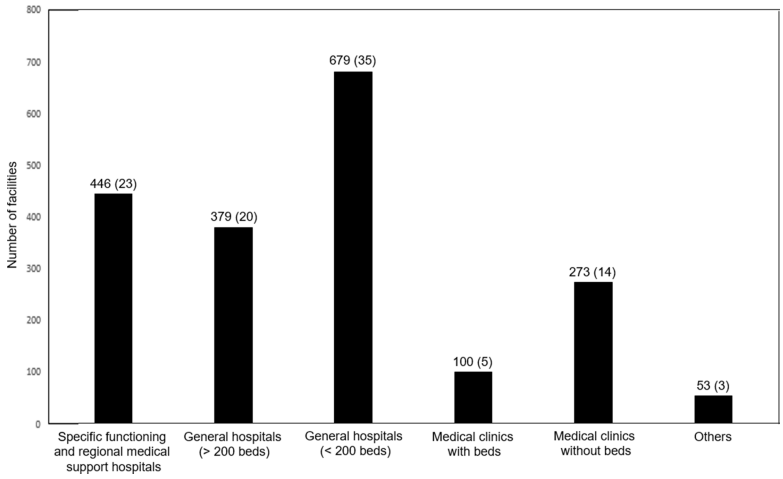

Fig. 1 Type of medical facilities (question 41).
Values are the number of facilities. Data in parentheses are percentage.

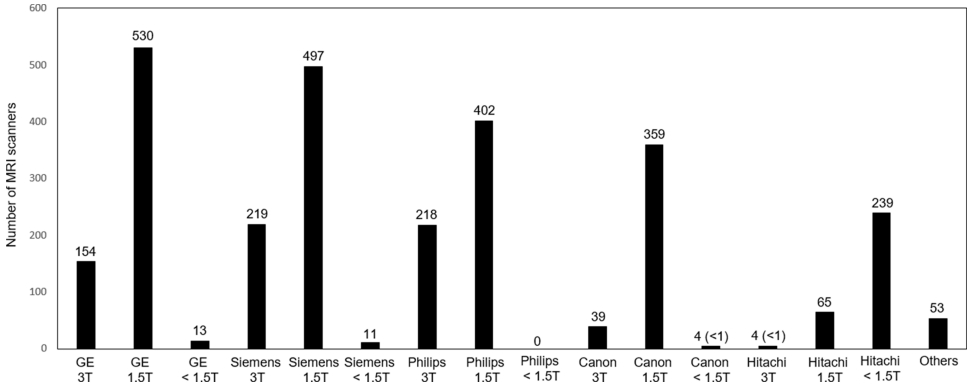

Fig. 2 Manufacturer and magnetic field strength of MRI scanners (multiple answers were allowed) (question 42).
Values are the number of MRI scanners. Data in parentheses are percentage.

Tables 1–6 list the answers submitted to the survey questionnaire. Of the 2015 responding facilities, some did not answer specific questions or did not perform MRI in certain patients.

As shown in Table 1, of 2009 responding facilities, only 256 (13%) had an on-site MRI management team and only 170 (9%) of 1880 facilities held management meetings at least once a year. Manuals were available at 1438 (72%) of 1994 facilities that responded to this item; however, 1004 (50%) of 1996 responders did not provide staff training to ensure the safety of patients and personnel in case of an emergency. The availability of manuals for dealing with different situations varied among the institutions. Only 298 (17%) of 1710 facilities provided a manual for the sedation of claustrophobic patients, and 201 (24%) of 838 facilities provided a manual for the management of sedated pediatric patients. Cooperation with the Pharmacy Department to assure the safe handling of gadolinium-contrast agents and of other drugs used during MRI studies was reported by 783 (46%) of 1708 and by 604 (37%) of 1634 MRI facilities, respectively.

Of 2006 facilities, 1658 (83%) checked their patients for implanted devices before MRI (Table 2). The rate of facilities that addressed the issues with potential effects before MRI examination is shown in Table 3. Of 2004 facilities, 1407 (70%) monitored the heart rate and blood

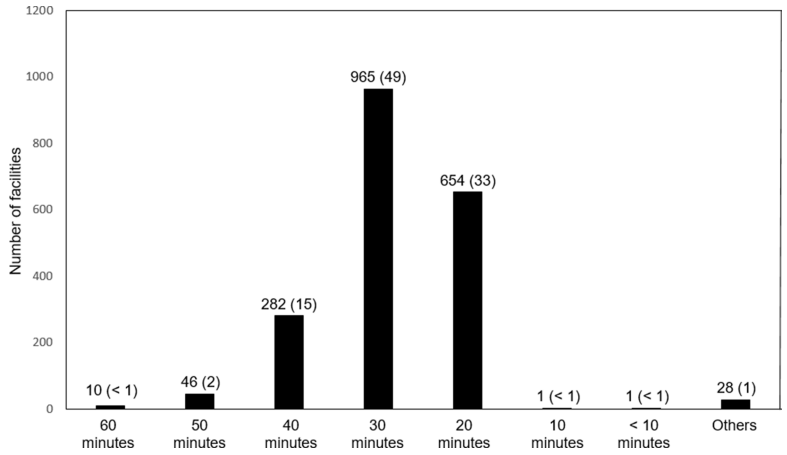

Fig. 3 Average time for 1 MRI examination (question 43).
Values are the number of facilities. Data in parentheses are percentage.

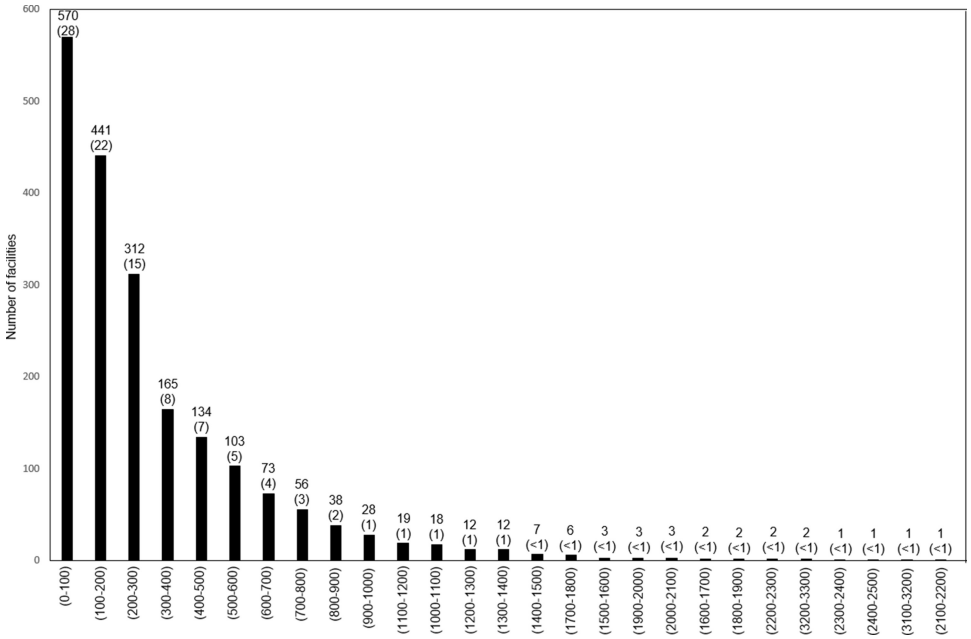

Fig. 4 Total number of MRI examinations during the month of September 2018 (question 44)
Values are the total number of MRI examinations. Data in parentheses are percentage.

oxygen level during MRI; noise reduction measures were implemented in 1707 of 2004 (85%) facilities (Table 4). The responses to questions related to the maintenance of MRI instruments and MRI records are shown in Table 5. About one-third of facilities kept records of the temperature, humidity, and oxygen concentration in the MRI room, and the temperature and humidity in the computer room. A phantom for quality control of the MRI equipment was present in 1656 (83%) of 2005 facilities. Phantom scans acquired at the start of the MRI system were examined for image artifacts in 1175 (58%) of 2015 facilities.

A summary of MRI-related accidents is shown in Table 6. During the period from October 2017 to September 2018, 90 (5%) of 1954 facilities experienced MRI-related major incidents that affected the patients' health and 519 (27%) minor incidents that did not. Factors that attributed to the occurrence of major and minor incidents are shown in Tables 7 and 8. Among 102 major incidents reported by 90 facilities, 31 (30%) were due to shock or death attributable to the administration of contrast agents; 519 facilities encountered 850 minor incidents, of which 28% were because of magnetic materials harbored by the patient, which were overlooked.

The automated machine learning platform identified 6 questions that were robust to varying sampling conditions and were strongly associated with major MRI-

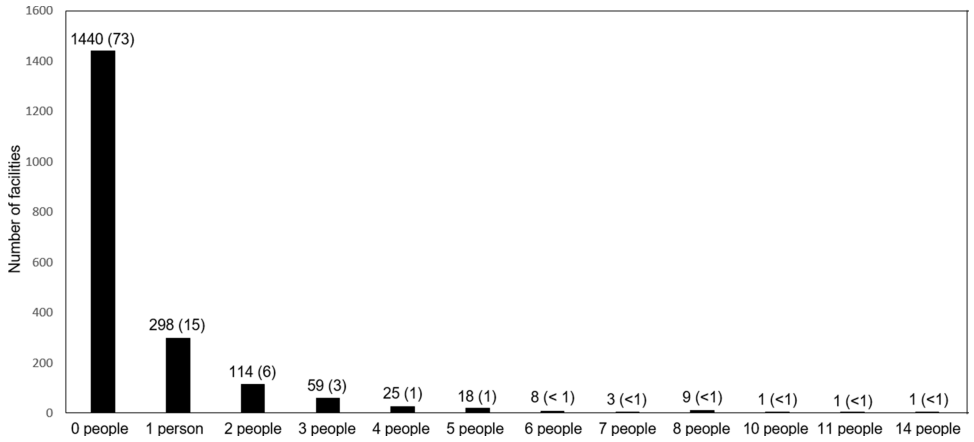

Fig. 5 Number of MRI-specialized personnel in each facility (question 45).
Values are the number of facilities. Data in parentheses are percentage.

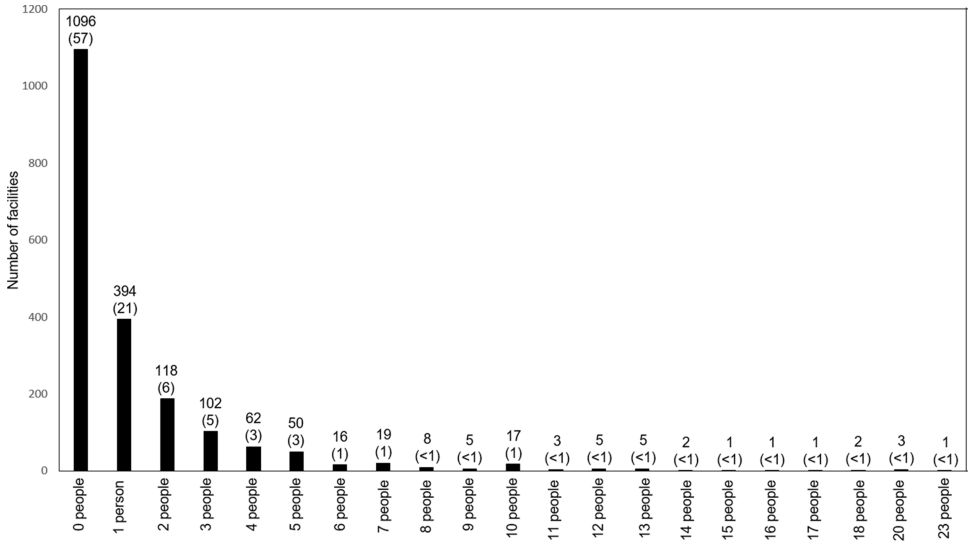

Fig. 6 Number of full-time radiologists involved in MRI protocol instructions, scan interpretation, and face-to-face interactions with patients and/or colleagues in each facility (question 46).
Values are the number of facilities. Data in parentheses are percentage.

related incidents (Fig. 8). The median, maximum, and minimum values of the permutation importance for the 6 items are also shown in the figure. Questions with higher permutation importance values are, in descending order, the total number of MRI examinations (question 44), post-marketing safety measures for drugs (question 15), manuals for the management of patients with implanted medical devices (question 11), the number of minor incidents (question 40), checking the body for magnetic substances before MRI examination (question 23), and regular maintenance inspection (question 34). There was a significant positive correlation between the total number of MRI studies and the partial dependence (the risk of major incidents) ($r = 0.8558$, $P < 0.0001$).

To assess the independent impact of individual variables on the occurrence of major incidents, we constructed partial dependence plots for 5 items (Fig. 9). After the total number of MRI studies (question 44), post-marketing safety measures for drugs (question 15) had the second largest impact. The risk ratio of a "no" to a "yes" answer was 1.53 (Fig. 9A). This was followed by a manuals for the management of patients with implanted medical devices (question 11), for which the risk ratio of a "yes" to a "no" answer was 1.17 (Fig. 9B); for the number of minor incidents (question 40), the risk ratio of a "yes" to "no" answer was 1.54 (Fig. 9C). Checking the body for magnetic substances before MRI examination (question 23) had a risk ratio of a "no" to a "yes" response of 2.7 (Fig. 9D). Last, regular maintenance inspections of the MRI equipment (question 34) at least once every 6 months had a risk ratio of a "no" to a "yes" response of 1.79 (Fig. 9E).

Discussion

There was a large variation among the responding facilities in the compliance rate with important specific MRI

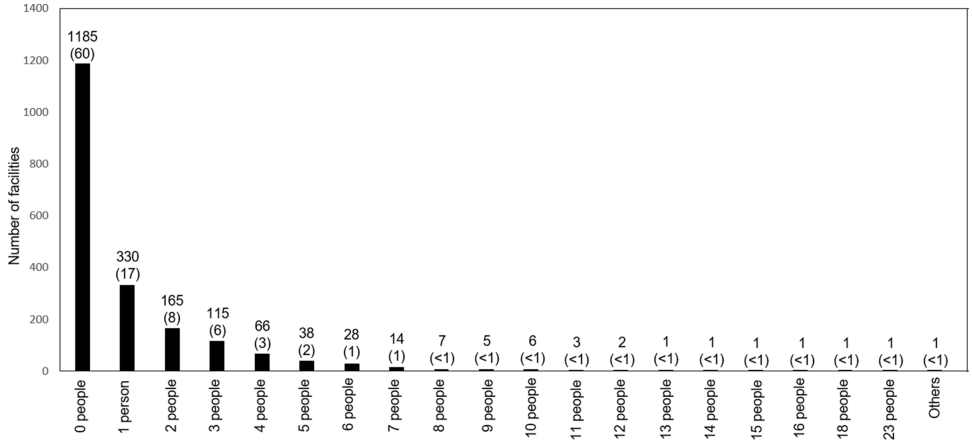

Fig. 7 Number of part-time radiologists specializing in MRI protocol instructions, scan interpretation, and face-to-face interactions with patients and/or colleagues in each facility (question 47).
Values are the number of facilities. Data in parentheses are percentage.

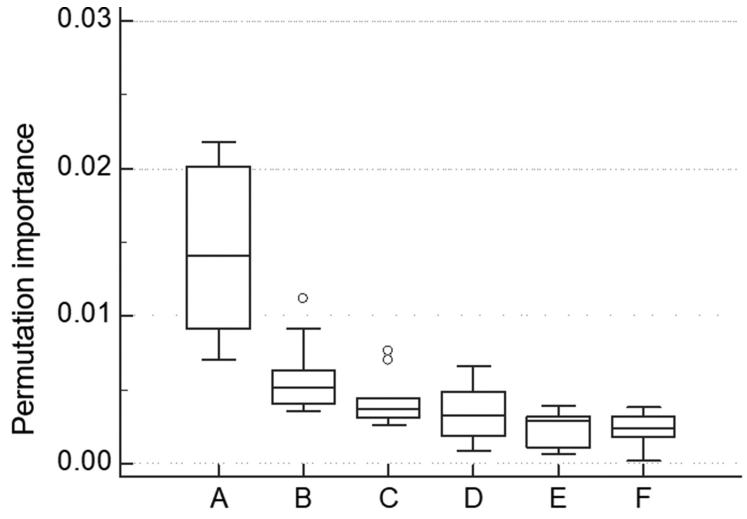

Permutation importance	A	B	C	D	E	F
Maximum	0.021873	0.01118	0.007657	0.006541	0.003938	0.003843
Median	0.014103	0.005128	0.003689	0.003271	0.002902	0.002387
Minimum	0.007043	0.003532	0.002555	0.000917	0.000585	0.000198

Fig. 8 The question items associated with major MRI incidents.
Box-and-whisker plots show the mean permutation importance for the 6 items (**A**–**F**). The lower and upper hinges of the boxes denote the 25th and 75th percentiles, respectively. The median (50th percentile) of each distribution is indicated by the line. The whiskers on each side denote the 10th and 90th percentiles. The median, maximum, and minimum values of each permutation importance are also shown.
(**A**) Question 44 (number of MRI examinations); (**B**) question 15 (post-marketing safety measure for drugs); (**C**) question 11 (manual for implantable medical devices); (**D**) question 40 (minor MRI-related incidents); (**E**) question 23 (body check before MRI examination); and (**F**) question 34 (maintenance inspections).

safety items. Highest compliance (99%) was with the requirement to check for transdermal patches (question 18) and the lowest compliance rate (9%) involved the holding of safety management meetings at least once a year (question 2). Only 13% of the respondents had an on-site management team (question 1).

The rates of major and minor incidents related to MRI studies were 5% and 27%, respectively, among facilities responding to this issue. To our knowledge, this is the first study that has presented on a facility-based basis the proportion of major and minor incidents associated with MRI. In 30% of major incidents, the administration of contrast agents was implicated. In a recent systematic review and meta-analysis[12], it was observed that immediate hypersensitivity reactions occurred in 31 (0.3%) of 14850 administrations (95% confidence interval: 0.2%–0.4%). The majority (90%; 28 of 31) of hypersensitivity reactions were mild; two (6%) were moderate; and one (3%) was severe. Since the study based its evaluations on the number of contrast-enhanced MRI studies rather than on the number of MRI facilities, we were not able to compare the rate of contrast medium–related incidents between their data and ours.

We found that the occurrence of major MRI-related incidents was strongly associated with the number of MRI studies performed at a facility and that the number

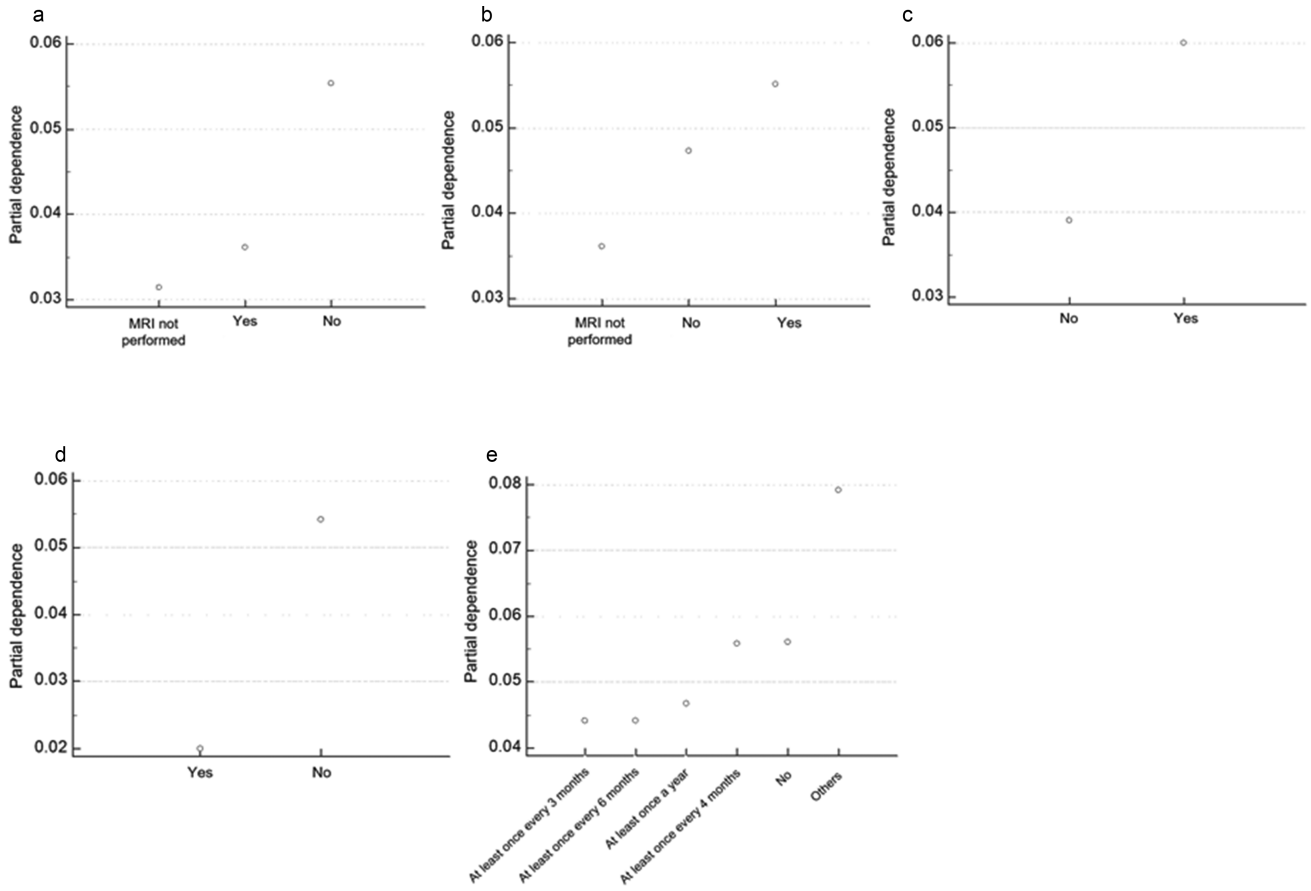

Fig. 9 Partial dependence plots showing independent impact of individual variables on 5 questions.
For question 15 (postmarketing safety measure for drugs) (**A**), "MRI not performed" indicates that the measure is not necessary because MRI examination using drugs other than gadolinium-contrast agents is not performed. The risk ratio of "no" to "yes" was 1.53.
For question 11 (manual for implantable medical devices) (**B**), "MRI not performed" indicates that MRI examination is not performed for patients with implantable medical devices (e.g., pacemakers). The risk ratio of "yes" to "no" was 1.17.
For question 40 (minor MRI-related incidents) (**C**), the risk ratio of "yes" to "no" was 1.54.
For question 23 (body check before MRI examination) (**D**), the risk ratio of "no" to "yes" was 2.7.
For question 34 (maintenance inspections) (**E**), the risk ratio of "no" to "at least once every 6 months" was 1.79 times.

Table 7 Summary of major incidents related to MRI examination (102 cases of 90 facilities)

Contents	No. of cases (%)
Shock or death from contrast agent administration	31 (30)
Burns from tattoos, permanent makeup, etc.	11 (11)
Failure of implantable medical device (pacemaker, etc.)	10 (10)
Tissue damage caused by equipment outside the body (power ankles, etc.)	3 (3)
Others	47 (46)

Table 8 Summary of minor incidents related to MRI examination (850 cases of 519 facilities)

Contents	No. of cases (%)
Overlooking magnetic material in the body	242 (28)
Overlooking equipment outside the body (power ankles, etc.)	146 (17)
Overlooking implantable medical devices (pacemakers, etc.)	127 (15)
Incidents regarding contrast agent administration	96 (11)
Overlooking tattoos, permanent makeup, etc.	22 (3)
Others	217 (26)

of minor incidents was also associated therewith. Our findings indicate that stronger safety standards must be implemented for facilities with a large number of examinations.

To avoid major incidents, manuals, staff training, drug information, and equipment maintenance are of great importance. According to a 2020 report of the Japan Medical Imaging and Radiological Systems Industries Association[13], the annual estimated number of MR device adsorption incidents in Japan was greater than 100. To reduce this rate, strong safety regulations must be implemented.

Our study revealed that many MRI facilities do not have adequate measures in place to guarantee the safety of MRI. Therefore, we encourage the involvement of academic societies and governmental and nongovernmental agencies. Points to be addressed are as follows:

- The presentation of educational lectures on MRI safety by the Japanese Society for Magnetic Resonance in Medicine
- The promulgation of guidelines by academic societies and government and nongovernment agencies
- The education of all personnel involved in MRI with respect to issues that pertain to MRI safety and the management of accidents
- The granting of more financial support to facilities with strong MRI safety standards by the Central Social Insurance Medical Council and the Ministry of Health, Labour and Welfare.

This study has some limitations. Although we contacted 5914 facilities that performed MRI, only 2015 (34%) responded fully or partially to all questions in the questionnaire. A full participation in the survey could have contributed to a more effective data. In the next questionnaire survey, it is suggested to create a questionnaire with fewer, more targeted questions to encourage higher participation in the survey of MRI facilities.

Conclusion

Among the participating facilities, there was a wide variation in the rate of compliance with the queried MRI safety issues. Nonetheless, our study revealed that overall compliance with safety standards was unsatisfactory. Between October 2017 and September 2018, major MRI-related incidents were reported by 5% of responding facilities and 27% encountered minor incidents. The most common factor implicated in major incidents was related to the administration of contrast agents. The most influential factor involved in major incidents was the total number of MRI studies performed at the facility. In addition to the total number of MRI studies, manuals, staff training, drug information, and equipment maintenance are very important to avoid major incidents. Our findings indicate that for the protection of patients and staff, strong safety standards must be promulgated and implemented and facilities with insufficient standards must be investigated to determine the cause for their inadequate safety management.

Funding

This work was supported by Health, Labour and Welfare Policy Research Grants for Research on Region Medical (H27-Iryo-Shitei-018).

Acknowledgments

The authors thank the members of an ad hoc committee (Guideline Creation Committee for Clinical MRI Safety Operation) in the Safety Committee of the JSMRM: Toshiaki Miyachi, PhD (Kanazawa University); Kagayaki Kuroda, PhD (Tokai University); Yoshiyuki Watanabe, MD (Shiga University); Kohsuke Kudo, MD (Hokkaido University); Masayuki Matsuo, MD (Gifu University); Shingo Kakeda, MD (Hirosaki University); Toshiaki Taoka, MD (Nagoya University); Tetsuya Yoneda, PhD (Kumamoto University); Keiko Toyota, MD (Jikei University of Medicine); Yoshiko Hayashida, MD (University of Occupational and Environmental Health); Atsushi Ono, PhD (Kawasaki University of Medical Welfare); Utaro Motosugi, MD (University of Yamanashi); Koji Uchida, PhD (Eda Clinic); and Kensuke Kyotani, PhD (Kobe University).

Conflicts of Interest

Ms. Koba is an employee of Varian Medical Systems Inc and Mr. Ijichi is an employee of DataRobot Inc. All data were entirely under the control of the corresponding author. Ms. Koba and Mr. Ijichi provided technical support for the survey and analyses. Dr. Murayama has received a research fund from Canon Medical Systems, Guerbet Japan KK, and Hitachi, Ltd. The other authors have no conflict of interest.

References

1. Organization for Economic Co-operation and Development. Health Data 2017. OECD Version: October 2019.
2. Expert Panel on MR Safety, Kanal E, Barkovich AJ, et al. ACR guidance document on MR safe practices: 2013. J Magn Reson Imaging 2013; 37:501–530.
3. Tsai LL, Grant AK, Mortele KJ, et al. A practical guide to MR imaging safety: what radiologists need to know. Radio Graphics 2015; 35:1722–1737.
4. Sammet S. Magnetic resonance safety. Abdom Radiol 2016; 41:444–451.
5. Chandra T, Chavhan GB, Sze RW, et al. Practical considerations for establishing and maintaining a magnetic resonance imaging safety program in a pediatric practice. Pediatr Radiol 2019; 49:458–468.
6. ACR Committee on MR Safety, Greenberg TD, Hoff MN, et al. ACR guidance document on MR safe practices: updates and critical information 2019. J Magn Reson Imaging 2020; 51: 331–338.

7. Lum M, Tsiouris AJ. MRI safety considerations during pregnancy. Clin Imaging 2020; 62:69–75.
8. The Safety Committee of the Japanese Society for Magnetic Resonance in Medicine (JSMRM). MRI safety-principles, standards and clinical concerns. 2nd ed. Tokyo: Gakken Medical Shujunsha, 2014. (in Japanese)
9. Data book of medical devices and systems. New Medicine in Japan 2018; 45:156–166. (in Japanese)
10. Breiman L. Random forests. Mach Learn 2001; 45:5–32.
11. Friedman JH. Greedy function approximation: a gradient boosting machine. Ann Stat 2001; 29:1189–1232.
12. Schieda N, van der Pol CB, Walker D, et al. Adverse events to the gadolinium-based contrast agent gadoxetic acid: systematic review and meta-analysis. Radiology 2020. May 26. doi:10.1148/radiol.2020200073. [Epub ahead of print]
13. Japan Medical Imaging and Radiological Systems Industries Association (JIRA). Number of estimated MR device adsorption accidents by year. April 1, 2020. http://www.jira-net.or.jp/anzenkanri/02_seizouhanbaigo/02-03.html#02-03_2018_0416 (Accessed: May 10, 2020) (in Japanese)

OPEN

Age-Related Changes in Relaxation Times, Proton Density, Myelin, and Tissue Volumes in Adult Brain Analyzed by 2-Dimensional Quantitative Synthetic Magnetic Resonance Imaging

Akifumi Hagiwara, MD, PhD, Kotaro Fujimoto, MD,*† Koji Kamagata, MD, PhD,* Syo Murata, PhD,* Ryusuke Irie, MD, PhD,* Hideyoshi Kaga, MD, PhD,‡ Yuki Someya, PhD,§ Christina Andica, MD, PhD,* Shohei Fujita, MD,*† Shimpei Kato, MD,*† Issei Fukunaga, PhD,|| Akihiko Wada, MD, PhD,* Masaaki Hori, MD, PhD,*¶ Yoshifumi Tamura, MD, PhD,‡§ Ryuzo Kawamori, MD, PhD,‡§ Hirotaka Watada, MD, PhD,‡§ and Shigeki Aoki, MD, PhD**

Objectives: Quantitative synthetic magnetic resonance imaging (MRI) enables the determination of fundamental tissue properties, namely, T1 and T2 relaxation times and proton density (PD), in a single scan. Myelin estimation and brain segmentation based on these quantitative values can also be performed automatically. This study aimed to reveal the changes in tissue characteristics and volumes of the brain according to age and provide age-specific reference values obtained by quantitative synthetic MRI.

Materials and Methods: This was a prospective study of healthy subjects with no history of brain diseases scanned with a multidynamic multiecho sequence for simultaneous measurement of relaxometry of T1, T2, and PD. We performed myelin estimation and brain volumetry based on these values. We performed volume-of-interest analysis on both gray matter (GM) and white matter (WM) regions for T1, T2, PD, and myelin volume fraction maps. Tissue volumes were calculated in the whole brain, producing brain parenchymal volume, GM volume, WM volume, and myelin volume. These volumes were normalized by intracranial volume to a brain parenchymal fraction, GM fraction, WM fraction, and myelin fraction (MyF). We examined the changes in the mean regional quantitative values and segmented tissue volumes according to age.

Results: We analyzed data of 114 adults (53 men and 61 women; median age, 66.5 years; range, 21–86 years). T1, T2, and PD values showed quadratic changes according to age and stayed stable or decreased until around 60 years of age and increased thereafter. Myelin volume fraction showed a reversed trend. Brain parenchymal fraction and GM fraction decreased throughout all ages. The approximation curves showed that WM fraction and MyF gradually increased until around the 40s to 50s and decreased thereafter. A significant decline in MyF was first noted in the 60s age group (Tukey test, $P < 0.001$).

Conclusions: Our study showed changes according to age in tissue characteristic values and brain volumes using quantitative synthetic MRI. The reference values for age demonstrated in this study may be useful to discriminate brain disorders from healthy brains.

Key Words: aging, MDME, myelin, quantitative synthetic MRI, relaxometry, volumetry

(*Invest Radiol* 2021;56: 163–172)

Quantitative magnetic resonance imaging (MRI) has revealed changes in brain tissue characteristics according to age.[1–13] Establishing normative reference values according to age is essential for discriminating disease from normal aging.[14] The signal intensity of conventional magnetic resonance (MR) images, such as T1- and T2-weighted images, is dependent on variations in acquisition parameters and scanners. Hence, the evaluation of such images is mainly performed by comparing with surrounding tissues.[15] Quantitative MRI can mitigate differences due to scanner differences and imperfections, as opposed to conventional MRI.[15,16] One method is simultaneous tissue relaxometry for quantifying T1 and T2 relaxation times (or their inverses, R1 and R2) and proton density (PD) with inherent alignment.[17] Recent studies of simultaneous relaxometry showed the changes in T1 and T2 values according to age using MR fingerprinting[18] in adults and quantitative synthetic MRI in children.[1] Quantitative synthetic MRI is typically performed through a commercial 2-dimensional (2D) multidynamic multiecho (MDME) sequence, providing simultaneous quantification of T1, T2, and PD, with a scan time of about 5 to 6 minutes for full head coverage.[16] Quantitative synthetic MRI has enabled objective evaluation of diseases such as Alzheimer disease,[19] multiple sclerosis,[20–22] brain infarction,[23] brain tumor,[24,25] and Sturge-Weber syndrome.[26] Using dedicated software, we can also automatically obtain brain parenchymal volume (BPV), white matter volume (WMV), and gray matter volume (GMV), based on these quantitative values.[27] Furthermore, voxel-wise myelin volume fraction (MVF) and myelin volume (MyV) in the whole brain can also be estimated from the same relaxometry values based on a 4-compartment model.[28] Myelin volume fraction derived from quantitative synthetic MRI has been validated by postmortem imaging[29,30] and comparison with other myelin imaging techniques.[22,31]

Received for publication June 12, 2020; and accepted for publication, after revision, July 20, 2020.

From the *Department of Radiology, Juntendo University Graduate School of Medicine; †Department of Radiology, Graduate School of Medicine, The University of Tokyo; ‡Department of Metabolism & Endocrinology, Juntendo University Graduate School of Medicine; §Sportology Center, Juntendo University Graduate School of Medicine; ||Department of Radiological Technology, Faculty of Health Science, Juntendo University; and ¶Department of Radiology, Toho University Omori Medical Center, Tokyo, Japan.

Conflicts of interest and source of funding: We have no conflicts of interest to declare. This work was supported by Japan Agency for Medical Research and Development (AMED) under grant number JP19lk1010025h9902; JSPS KAKENHI grant numbers 19K17150, 19K17177, and 18K07692; Health, Labour, and Welfare Policy Research Grants for Research on Region Medical; a grant-in-aid for Special Research in Subsidies for ordinary expenses of private schools from The Promotion and Mutual Aid Corporation for Private Schools of Japan; and Brain/MINDS program from AMED grant numbers JP19dm0307024 and JP19dm0307101.

Correspondence to: Akifumi Hagiwara, MD, PhD, Department of Radiology, Juntendo University School of Medicine, 1-2-1, Hongo, Bunkyo-ku, Tokyo, Japan 113-8421. E-mail: a-hagiwara@juntendo.ac.jp.

Supplemental digital contents are available for this article. Direct URL citations appear in the printed text and are provided in the HTML and PDF versions of this article on the journal's Web site (www.investigativeradiology.com).

ISSN: 0020-9996/21/5603–0163
DOI: 10.1097/RLI.0000000000000720

Quantifying the degree of brain atrophy is especially crucial in evaluating neurodegenerative disorders, such as Alzheimer disease,[14,32] vascular dementia,[33] and multiple sclerosis.[34] Although quantification of BPV may be useful for management and early diagnosis of these diseases, it can be challenging to determine whether the brain atrophy is caused by normal aging or pathological processes. Previous studies have shown age-related decreases in BPV,[35] GMV,[36–38] and WMV.[39,40] For brain volumetry, postprocessing software, such as FreeSurfer, FMRIB Software Library (FSL), and Statistical Parametric Mapping, has been used. These methods require relatively longer postprocessing times (from 10 minutes to a few hours),[21] hindering clinical use in a timely manner. On the other hand, quantitative synthetic MRI is already approved by the Food and Drug Administration and can perform tissue volumetry based on tissue relaxation times by dedicated software with a postprocessing time of less than 1 minute, which is feasible in clinical practice.[16] Previous studies have shown that the volumetric measurements, including BPV, GMV, WMV, and intracranial volume (ICV), performed on 2D quantitative synthetic MRI agreed with those on other volumetric software, such as FreeSurfer, FSL, and Statistical Parametric Mapping, using 3D T1-weighted images.[21,41]

Relaxometry, PD measurement, volumetry, and myelin measurements performed with quantitative synthetic MRI have been reported to be highly repeatable and reproducible across scanners from different vendors,[15,42] and age-related changes in these values have been demonstrated in children.[1–3] However, to our knowledge, there has been no study discussing the age-related changes in T1, T2, and PD, and GMV, WMV, and MyV obtained by quantitative synthetic MRI in adults. Integrating relaxometry and tissue volumetry, we can estimate age-related changes in the human brain in a multidimensional manner. Further, reference values for age are prerequisites to discriminate abnormal from normal in an individual brain. Therefore, this study aimed to describe the changes in regional relaxometry and brain tissue volumes as well as MyV according to age and to provide reference values obtained by an MDME sequence according to age.

MATERIALS AND METHODS

Subjects

A total of 134 subjects 20 years or older with no history of brain disorders were enrolled in this study, and written informed consent was obtained from all subjects. Subjects 65 years or older were recruited as part of the Bunkyo Health Study lasting over 10 years that included 1629 older people aimed at the prevention of disease requiring long-term care.[43] Subjects recruited from April 2017 until September 2018 in the Bunkyo Health Study were included in the current study. We classified white matter (WM) hyperintensity on fluid-attenuated inversion recovery (FLAIR) imaging using the Fazekas scale[44] and excluded subjects with a scale score of 3 or higher. We also excluded subjects with old hemorrhage, microbleeds, infarcts, and/or intracranial mass lesions detected on T2*-weighted images and FLAIR images.

MR Acquisition and Quantitative Maps

All subjects were scanned using an MDME sequence on a 3 T scanner (MAGNETOM Prisma, Siemens Healthcare, Erlangen, Germany) with a 64-channel head coil. This sequence is a multislice, multisaturation deslay, multiecho, fast spin-echo sequence, using combinations of 2 echo times (TEs) and 4 delay times to produce 8 complex images per slice.[17] The TEs were 22 and 99 milliseconds, and the delay times were 170, 620, 1970, and 4220 milliseconds. The repetition time (TR) was 4250 milliseconds. The other parameters used for MDME were as follows: field of view, 230 × 186 mm; matrix, 320 × 260; echo-train length, 10; bandwidth, 150 Hz/pixel; parallel imaging acceleration factor, 2; slice thickness/gap, 4.0/1.0 mm; 30 sections; and acquisition time, 5 minutes 8 seconds. The postprocessing was performed using SyMRI software (version 8.04; SyntheticMR AB, Linköping, Sweden) to retrieve T1, T2, and PD maps. The PD values are reported as percentage unit (pu), where the PD of pure water at 37°C corresponds to 100 pu.[17] The details of the postprocessing are described elsewhere.[17] We created T1-weighted and FLAIR images with postprocessing TR of 500 milliseconds and TE of 10 milliseconds, as well as TR of 15,000 milliseconds, TE of 100 milliseconds, and inversion time of 3000 milliseconds, respectively, based on T1, T2, and PD maps on SyMRI software (SyntheticMR AB). The patients were also scanned using T2*-weighted gradient-echo imaging. The scan parameters were as follows: TR, 500 milliseconds; TE, 12 milliseconds; flip angle, 20°; field of view, 230 × 201.3 mm; matrix, 320 × 176; echo-train length, 1; bandwidth, 230 Hz/pixel; parallel imaging acceleration factor, 3; slice thickness/gap, 5/1 mm; sections, 22; and acquisition time, 48 seconds.

Myelin volume fraction in each voxel was automatically calculated by using SyMRI software (SyntheticMR AB). The model of myelin calculation was based on the 4-compartment model in the brain: myelin, cellular, free water, and excess parenchymal water volume fractions.[21] The R1, R2, and PD values of free water and excess parenchymal water volume fractions were fixed to those of cerebrospinal fluid (CSF) (R1, 0.24 s^{-1}; R2, 0.87 s^{-1}; PD, 100%).[17] The R2 of MVF was fixed to the literature value of 77 s^{-1}.[45] Optimization of other model parameters was performed by simulation of running Bloch equations for observable R1, R2, and PD properties in a spatially normalized and averaged brain from a group of healthy subjects. In this model, the magnetization exchange rates between partial volume compartments are also considered. A lookup grid was made in R1-R2-PD space for all possible distributions (ranging from 0% to 100%) of the 4 volume fractions. The measured R1, R2, and PD values were projected onto the lookup grid for estimating the MVF in each voxel.

Volume of Interest Analysis

T1, T2, PD, and MVF maps were evaluated by volume of interest (VOI) analysis. We created 8 gray matter (GM) (frontal, parietal, temporal and occipital GM, insula, caudate, putamen, and thalamus) and 8 WM (frontal, parietal, temporal and occipital WM, genu and splenium of the corpus callosum, internal capsules, and middle cerebellar peduncles) VOIs in the Montreal Neurological Institute space as described previously.[42] Other than splenium of the corpus callosum, we combined the right and left components, because the right-left difference has been reported to be minimal for relaxometry.[46] We warped VOIs created in the Montreal Neurological Institute space to the space of each volunteer using FSL v 5.0.11 (http://fsl.fmrib.ox.ac.uk/fsl/fslwiki/FSL) linear and nonlinear image registration tools (FLIRT and FNIRT), based on the synthetic T1-weighted images. No smoothing was used. The GM and WM masks were generated from the synthetic T1-weighted images using FMRIB's Automated Segmentation Tool. These masks were then thresholded at 0.9 and used on the T1, T2, PD, and MVF maps to compute average values within the GM and WM. In other words, VOI analysis of GM and WM structures was performed only on voxels for which equal to or more than 90% of their volumes are GM and WM, respectively. Figure 1 shows an example of VOI measurements.

Brain Tissue Volume and MyV Calculation

Based on the acquired T1, T2 and PD, we also calculated GM/WM/CSF volume in the whole brain on the SyMRI software (SyntheticMR AB). The measured quantitative values of brain tissues were used as coordinates in the T1-T2-PD space. Based on the quantitative values for WM, GM, and CSF measured by SyMRI (SyntheticMR AB) for healthy controls, each brain tissue was defined and a numerical Bloch simulation was performed to investigate T1, T2, and PD for tissue mixtures and their partial volumes. Technical

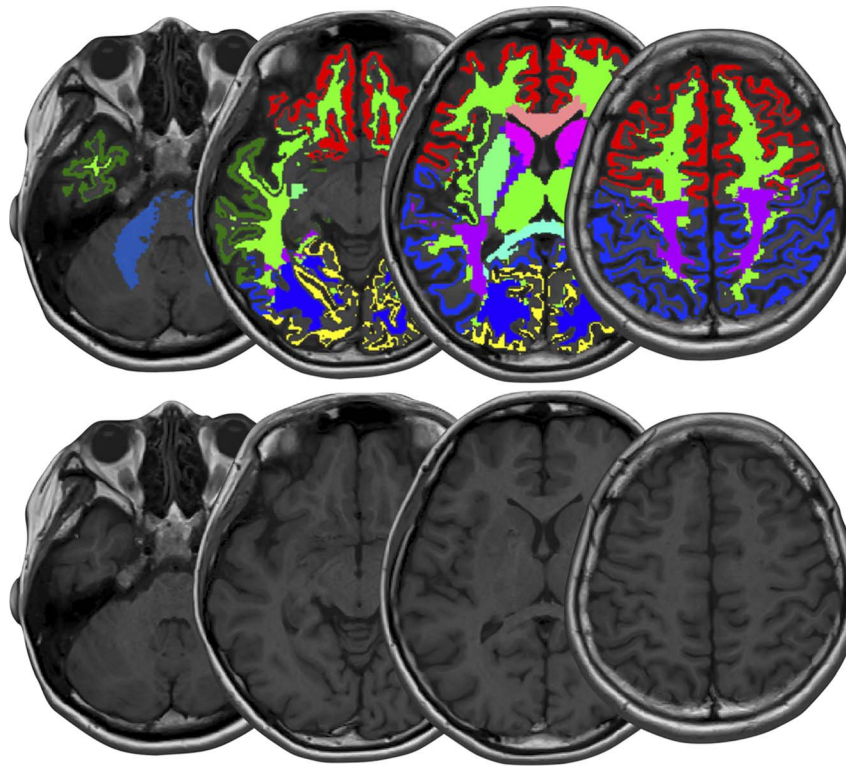

FIGURE 1. An example of VOI analysis. The upper and lower rows show T1-weighed images with and without, respectively, VOI overlay.

details are described elsewhere.[27] Voxels not classified as GM, WM, or CSF were called non-WM/GM/CSF (NoN). Total volumes of GM, WM, CSF, and NoN were summed up for each voxel in the intracranial tissue. The BPV was calculated as the sum of WM, GM, and NoN. Myelin volume fraction in each voxel was also summed up in the whole brain to represent the MyV. The border of the ICV was defined exactly at a PD of 50%, assuming that the edge of the ICV corresponds to the interface between CSF (PD = 100%) and bone (PD = 0%).[47] The ICV is automatically cut at the base of the skull.[48] The ICV corresponds to the sum of BPV and CSF. Acquired volumes were normalized by ICV, and we obtained the brain parenchymal fraction (BPF), WM fraction (WMF), GM fraction (GMF), and myelin fraction (MyF). Figure 2 shows representative quantitative and tissue volume maps.

Statistical Analysis

For statistical analysis, the normality of each variable was tested using the Shapiro-Wilk test. We compared the age, quantitative values (T1, T2, PD, and MVF) averaged in each segmented area, tissue volumes, and tissue fractions between men and women using a Mann-Whitney *U* test or Student *t* test. To verify the validity of adjusting each volume by ICV, we performed correlation analysis between age and ICV and between ICV and BPV.

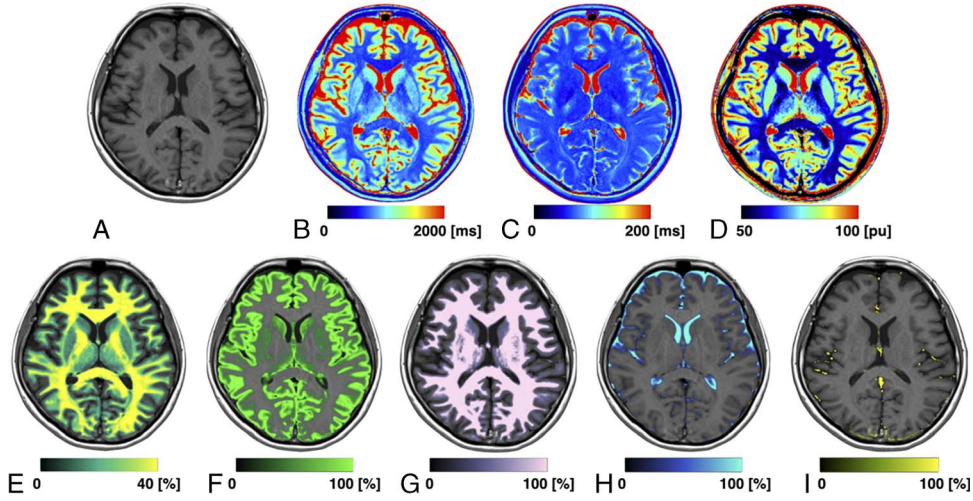

FIGURE 2. Representative images of a 24-year-old patient. Panels show a synthetic T1-weighted image (A) and maps of T1 (B), T2 (C), PD (D), MVF (E), GM (F), WM (G), CSF (H), and NoN (I). MVF, GM, WM, CSF, and NoN maps are overlaid on a T1-weighted image.

To investigate the relationship between age and quantitative values, we conducted regression analyses as a function of age. For tissue volume fraction (BPF, GMF, WMF, MyF), regression analyses were performed as a function of age separated by sex. We selected linear or quadratic approximation by choosing the one that showed the smaller Akaike information criterion (AIC).[44] We stratified the subjects into each decade (7 groups: 21–29, 30–39, 40–49, 50–59, 60–69, 70–79, and 80–86 years) and performed 2-way analysis of variance (ANOVA) to test the effect of age and sex on MyF. In case of a significant effect on the ANOVA, a post hoc Tukey test was performed for multiple comparisons. The level of statistical significance was set at $P < 0.05$. Statistical analyses were performed with Matlab (release R2015b; MathWorks, Natick, MA).

RESULTS

Of the 132 subjects included in this study, those with old hemorrhage, microbleeds, and/or infarctions (n = 17) and with an intracranial mass lesion (n = 1) were excluded. Hence, we excluded 18 subjects in total and the data of 114 subjects were finally analyzed (53 men; median age, 66.5 years; age range, 21–86 years). Each decade group from the 20s to 70s included at least 5 men and 5 women. There were 2 men and 6 women in their 80s.

VOI Analysis

No significant differences were found in T1, T2, PD, and MVF between men and women, except for T1 in the middle cerebellar peduncle (men vs women [mean ± SD], 830 ± 27 vs 816 ± 32 milliseconds; $P = 0.01$) and PD in the caudate (mean vs women [mean ± SD], 78.8 ± 2.1 vs 79.5 ± 1.6 pu; $P = 0.04$).

In all segmented areas, the approximate curves of T1, T2, PD, and MVF were the best fitted by quadratic curves (Figs. 3–6). The equations used to plot the T1, T2, PD, and MVF curves are provided, respectively, in Supplemental Digital Content 1 to 4, http://links.lww.com/RLI/A561. The AICs of linear and quadratic approximations for T1, T2, PD, and MVF are shown in Supplemental Digital Content 5, http://links.lww.com/RLI/A561. The coefficient of determination (R^2) was higher than 0.1 for all estimations, except for PD in the insula, middle cerebellar peduncle, and thalamus and MVF in the occipital GM, the middle cerebellar peduncle, putamen, and the thalamus. Overall, T1 and T2 were stable until around the 60s and increased thereafter. Proton density was stable in almost all areas until around the 60s, except for GM, which showed a variable degree of decrease, with frontal GM showing the highest rate of decrease. Overall, PD showed an increase after the 60s. Myelin volume fraction showed the opposite tendency to PD. For T1, T2, PD, and MVF, the middle cerebellar peduncle showed smaller changes compared with supratentorial regions. The occipital GM and WM showed slower demyelination in the senescence period compared with the frontal, parietal, and temporal GM and WM, respectively, with the frontal GM and temporal WM showing the fastest demyelination among these GM and WM structures, respectively, as indicated by Figure 6 and the first coefficients of MVF for age^2 (the first coefficients of MVF: frontal GM, −0.0031; parietal GM, −0.0020; temporal GM, −0.0015; occipital GM, −0.00048; frontal

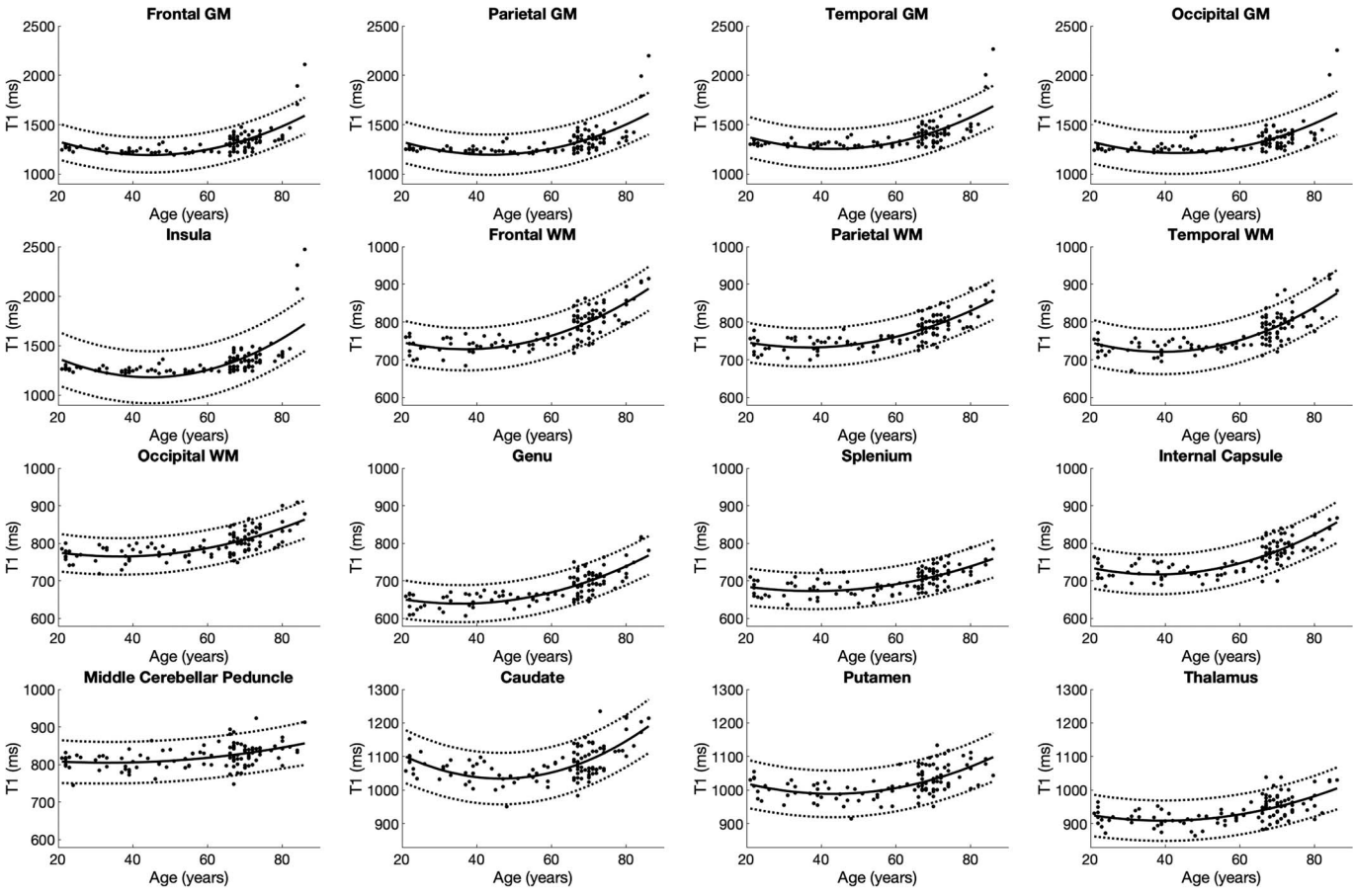

FIGURE 3. Scatterplots and approximate curves of T1 values in relation to age for each region. A regression line is shown with 95% confidence intervals (dotted lines).

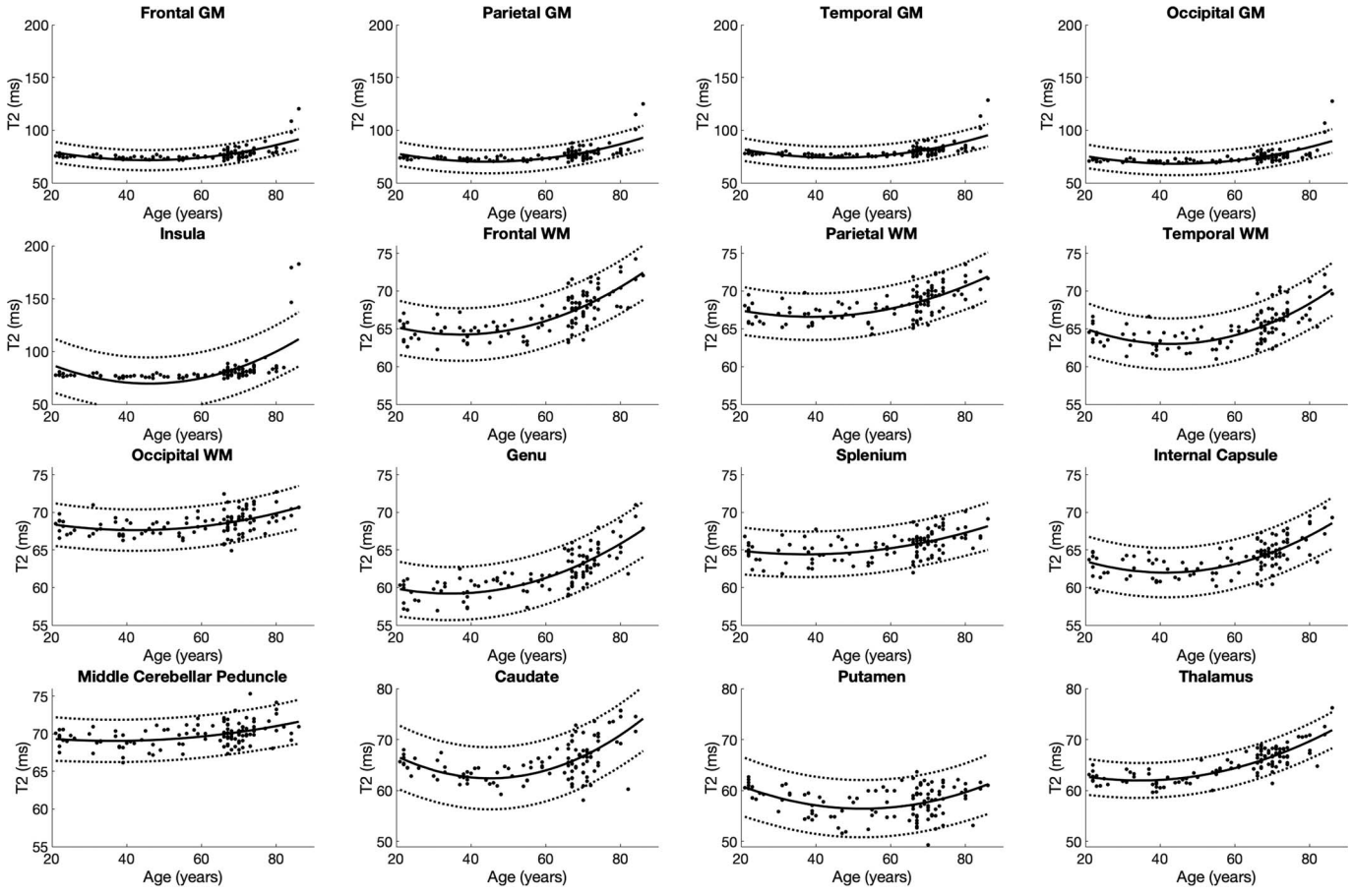

FIGURE 4. Scatterplots and approximate curves of T2 values in relation to age for each region. A regression line is shown with 95% confidence intervals (dotted lines).

WM, −0.0032; parietal WM, −0.0023; temporal WM, −0.0035; occipital WM, −0.0022) shown in Supplemental Digital Content 4, http://links.lww.com/RLI/A561.

Tissue Volumes and Volume Fractions

There was no significant correlation between ICV and age (Spearman correlation coefficient [95% confidence interval], −0.11 [−0.30 to 0.08]; $P = 0.26$), and there was a significant strong correlation between ICV and BPV (Pearson correlation coefficient [95% confidence interval], 0.82 [0.74–0.88]; $P < 0.001$) (Supplemental Digital Content 6, http://links.lww.com/RLI/A561). Hence, it was considered to be appropriate to normalize each tissue volume by ICV to evaluate the effect of aging on tissue volumes.

Mean tissue volumes and volume fractions are shown in Table 1. We found significantly larger brain tissue volumes in men than women. After normalization by ICV however, BPF, GMF, and WMF were significantly smaller in men than in women, whereas there was no significant difference in MyF between men and women ($P = 0.36$).

The changes in BPF, GMF, WMF, and MyF in relation to age are shown in Figure 7. The equations used to plot the curves are shown in Supplemental Digital Content 7, http://links.lww.com/RLI/A561. All of these metrics were best approximated by quadratic curves. The AICs of linear and quadratic approximations for BPF, GMF, WMF, and MyF are shown in Supplemental Digital Content 8, http://links.lww.com/RLI/A561. Brain parenchymal fraction monotonously decreased through all ages, and it decreased slightly faster after around the 50s. Gray matter fraction decreased until around the 60s and became stable. White matter fraction and MyF seemed to increase gradually until the 40s, and they were on the decline thereafter.

A 2-way ANOVA for age and sex factors with MyF as dependent variables showed a significant effect of age group on MyF ($P < 0.001$), but the effects of sex and interaction between age and sex were not significant ($P = 0.28$ and 0.97, respectively). Tukey multiple comparison test for MyF did not show significant differences among younger groups (equal to and under the 50s), whereas it showed a significant difference between the younger groups and the older groups (60s and over) and among older groups except between 60s and 70s (Fig. 8). In other words, the earliest decade of life where a significant decrease in MyF was found was in the 60s age group ($P < 0.001$ compared with the 50s age group).

DISCUSSION

We performed quantitative synthetic MRI on healthy adults aged 21 to 86 years and examined the change in T1, T2, PD, and MVF values and tissue volumes associated with aging. Regional T1, T2, and PD values showed similar patterns of change with aging, except for the middle cerebellar peduncle that showed smaller changes compared with supratentorial regions. Overall, T1, T2, and PD values were stable or slightly decreased until the 60s and increased thereafter, whereas MVF showed a reversed trend. Various microstructural changes have been shown to affect T1 and T2 values. Some reports indicated that changes in T1 and T2 values result from the change in water content,[49] myelin,[50] and iron.[51] In the normal aging process until about 50,

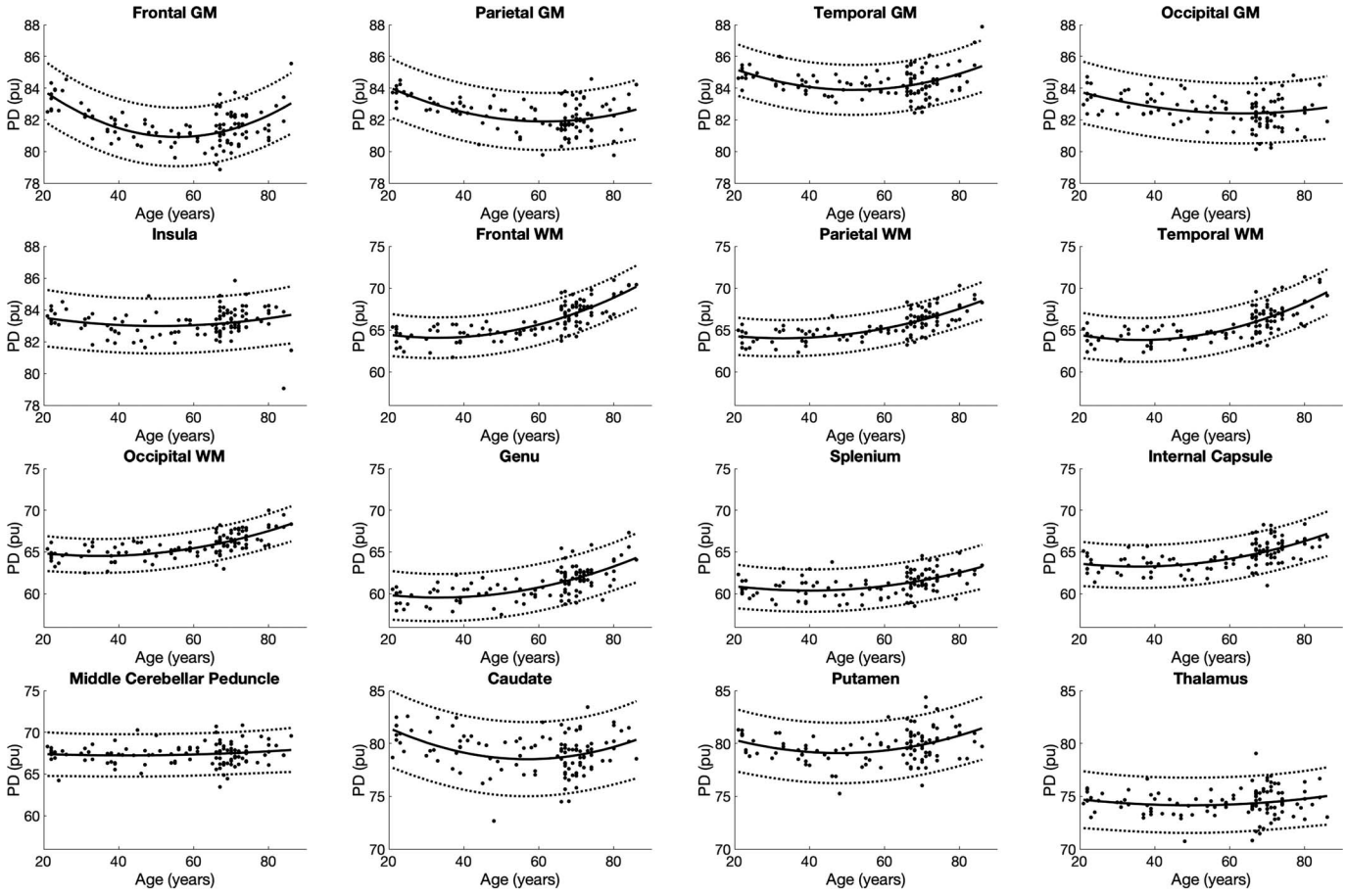

FIGURE 5. Scatterplots and approximate curves of PD in relation to age for each region. A regression line is shown with 95% confidence intervals (dotted lines).

myelination has been suggested to continue, which is followed by demyelination.[52] During continuing myelination in children, myelin increase and water decrease contribute to the decrease in T1 and T2 values.[53] Our results for adults until the 60s were partially congruent with this observation, with MVF in some regions, mainly GM, increasing along with a decrease in PD. The effect of sex on relaxometry was minimal in this study, in line with a previous study performed by MR fingerprinting.[18]

In our study, the T1, T2, and PD of GM started to increase from the 60s, and T1 showed a remarkable increase after 80 years, possibly because of an increase in water content. Stable T1 and T2 values from the 20s until 60s in both GM and WM and increases from 60s are in line with previous studies,[6,13,18,46] except for reports by Gracien et al[54] and Okubo et al.[55] Gracien et al showed a decrease in the T1 value of the cortical GM after the 60s over 7 years in 17 healthy subjects (51–77 years) and concluded that this observation was due to decreasing water and iron accumulation. This discrepancy may lie in the difference in methods used for relaxometry (quantitative synthetic MRI vs variable flip angle). Okubo et al[55] used 3D T1 map created by magnetization-prepared 2 rapid acquisition gradient echoes sequence to investigate the effect of aging on T1 values. Even though wide areas showed increases in T1 related to aging on voxel-based analysis, some structures (ie, inferior putamen, nucleus accumbens, and amygdala) showed decreases. The narrower age range in their study (ie, 20–76) than ours (ie, 21–86), usage of only linear regression in their study, and differences in sequences and analysis methods may have resulted in the discrepancy between the results of their and our studies. Notably, discrepancy in the T1 values obtained with different methods are discussed in previous literatures.[15,56] For example, Stikov et al[56] compared inversion recovery, Look-Locker, and variable flip angle techniques and reported that deviations from inversion recovery reached over 30% in the WM, from 750 milliseconds in the Look-Locker technique (underestimation) to 1070 milliseconds in the variable flip angle technique (overestimation). Even though we mitigated partial volume effects by thresholding the partial GM volume maps, the quantitative values could have been affected by partial volume effects because the cortex in elderly people is thinner than in younger people.[57] Because the tissue properties of the cortical GM are more different from the CSF than the WM, the partial volume effects, if any, would affect the quantitative values of the cortical GM by deviating them slightly near to those of the CSF (ie, leading to increases in T1, T2, and PD and a decrease in MVF). Likewise, enlarged perivascular spaces, which progress with aging,[58] may also have affected the quantitative values of subcortical GM and WM. Novel 3D quantitative synthetic MRI, which is still a research sequence but mitigates the partial volume effect, is desired to be used to further investigate the age-related changes in the quantitative values in the cortical GM.[59–61] Meanwhile, T1 value in the cortical GM has been reported to be stable in other studies, possibly because of the much smaller sample size of subjects over 60 compared with the younger population.[46,62,63]

Age-related myelin changes in adults have been investigated by myelin water imaging[10,11] and magnetization transfer imaging.[12,13,52] The quadratic inverted U-shape trend shown in our study, with stable or increasing myelin metrics until around the 60s and the following

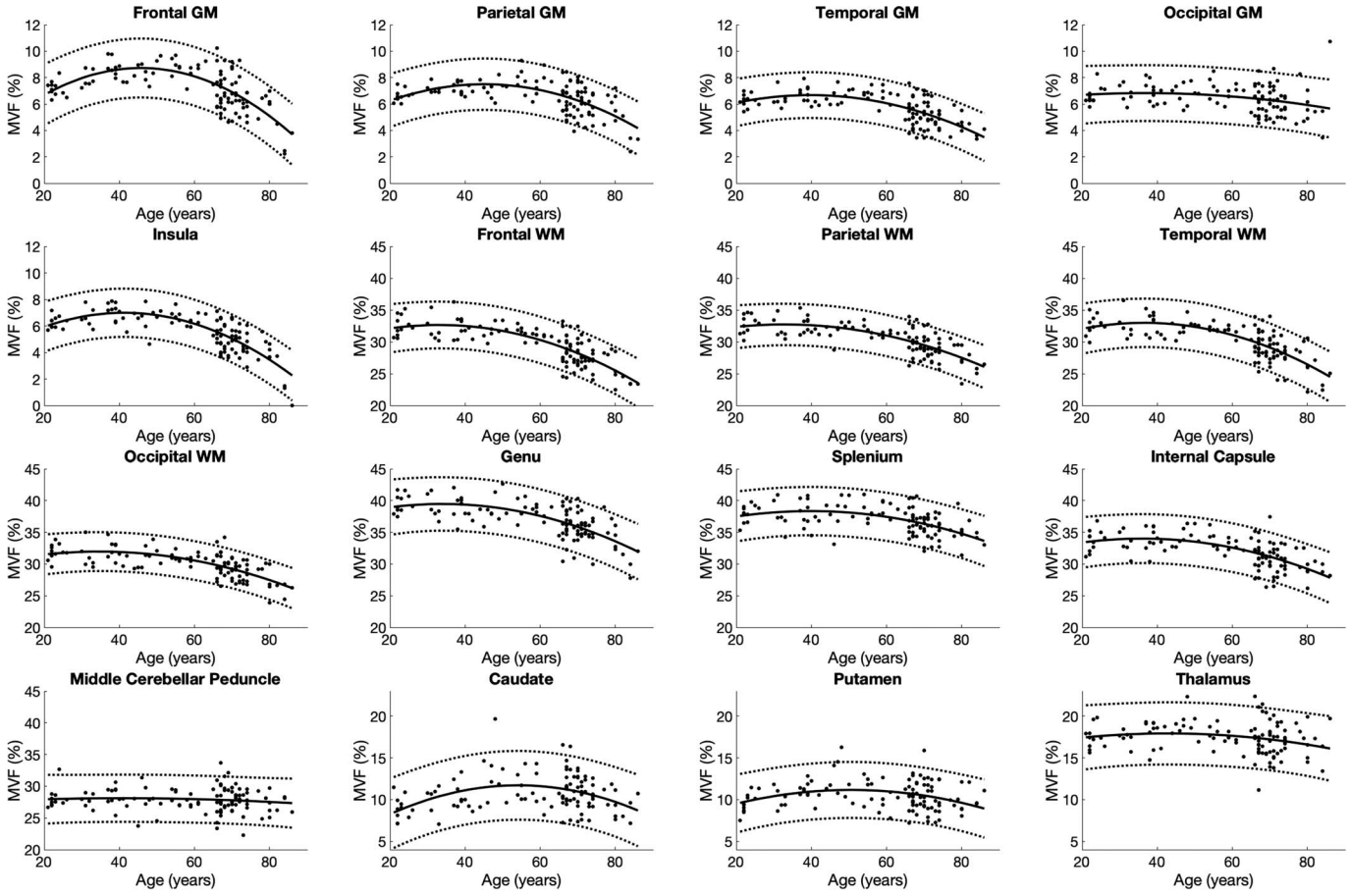

FIGURE 6. Scatterplots and approximate curves of MVF in relation to age for each region. A regression line is shown with 95% confidence intervals (dotted lines).

TABLE 1. The ICV, BPV, GMV, WMV, and MyV of Men and Women

	Men (n = 53)	Women (n = 61)	*P*
Age, median (range), y	67 (22–86)	66 (21–84)	0.88
Raw volume, mean ± SD, mL			
ICV	1530 ± 115	1350 ± 91	<0.001
BPV	1260 ± 120	1150 ± 91	<0.001
GMV	715 ± 69	650 ± 53	<0.001
WMV	523 ± 62	477 ± 52	<0.001
MyV	173 ± 24	154 ± 20	<0.001
Volume normalized by ICV, mean ± SD, %			
BPF	82.5 ± 5.1	84.9 ± 4.3	0.008
GMF	46.8 ± 3.5	48.2 ± 2.9	0.02
WMF	34.2 ± 2.8	35.3 ± 3.1	0.048
MyF	11.2 ± 1.2	11.4 ± 1.2	0.36

P values are for comparisons between men and women. All comparisons are performed with Student *t* test, except for age, which is analyzed using the Mann-Whitney *U* test. $P < 0.05$ is considered statistically significant.

Abbreviations: ICV, intracranial volume; BPV, brain parenchymal volume; GMV, gray matter volume; WMV, white matter volume; MyV, myelin volume; BPF, brain parenchymal fraction; GMF, gray matter fraction; WMF, white matter fraction; MyF, myelin fraction.

decease, was also shown in these studies, except for the linear decrease reported by Cercignani et al,[12] who included the fewest number of participants among these studies. In line with the observation by myelin water imaging,[10] the occipital lobes showed delayed demyelination compared with other lobes in the senescence period. This regional demyelination pattern agrees with the retrogenesis hypothesis (first-in-last-out), in which the posterior brain is spared from degeneration for healthy subjects in the senescence period and patients with Alzheimer disease compared with the late-myelinated anterior brain.[64–66]

Upon investigation of age-related changes in tissue volumes, we revealed that the original brain tissue volumes, namely, BPV, GMV, WMV, and MyV, were larger in men than in women; however, after normalization, these tissue volumes, except for MyF, were significantly larger in women than in men. Previous studies have shown that the brains of men are larger than those of women, while BPV is dependent on skull size.[7,67–69] In our study, BPV had a strong correlation with ICV, and ICV had no significant change upon aging, in line with the results of previous studies.[7,70,71] These results justified the appropriateness of normalization of tissue volumes using ICV. Previous studies investigating sex differences in GMF and WMF were only partially congruent with our results,[72,73] possibly owing to the small effect size of sex on normalized volumes.

We demonstrated that the inverted U-shaped quadratic curve was better fitted to BPF than a line as a function of age, with a constant decrease in BPF accelerating throughout adulthood. There is general agreement that BPF constantly declines in adulthood upon aging,[40,41,67] and some of them also fitted quadratic curves to BPF in relation to

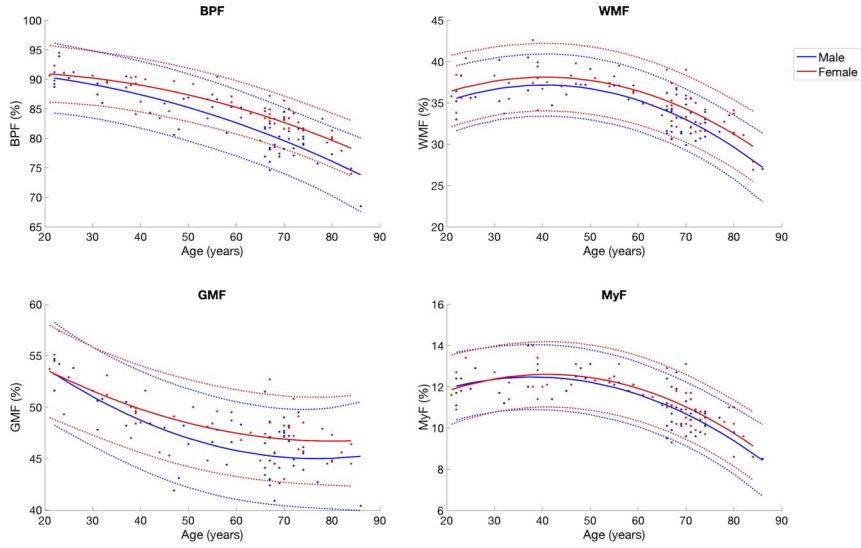

FIGURE 7. Scatterplots of BPF, GMF, WMF, and MyF in relation to age. Regression lines are shown with 95% confidence intervals (dotted lines).

aging.[41,67] Contrary to BPF, the rate of decrease in GMF was decelerated through adulthood and GMF became stable after around the 60s. This deceleration pattern is in line with previous studies,[7,46] although other studies reported a linear decrease in GMF.[36,73] Notably, a decrease in GMF and BPF was observed to begin even at a younger age around the 10s, after an increase during the developmental period.[2]

Similar quadratic inversed U-shapes are shown by WMF and MyF, with peaks at around the 40s to 50s. The Tukey multiple comparison test also supported this result for MyF, demonstrating the 60s age group to be the earliest decade of life showing a significant decrease in MyF. Previous studies have also reported an increase in WMF until around the 40s[7,36,37,72–74] and a decline after the 40s.[36,72–75] This gradual increase in WMF has been suggested to reflect myelination continuing until midlife shown by histology of human brains.[76] To our knowledge, our report is the first to show MyF changes with aging in adults.

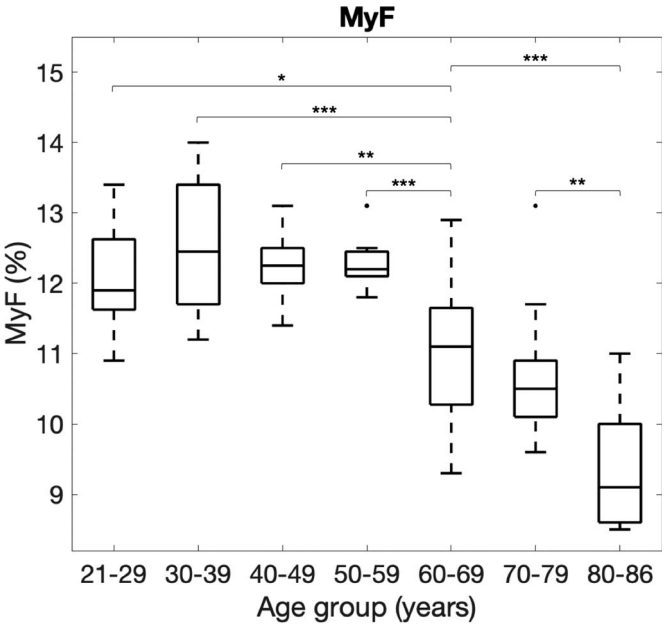

FIGURE 8. Boxplots of MyF stratified by decade-long age groups. A significant difference revealed by Tukey multiple comparisons is shown as a bracket. Comparisons between the 50s or younger and 70s or 80s, which also show significant differences, are omitted for visual clarity. *$P < 0.05$, **$P < 0.01$, ***$P < 0.001$.

Even though we focused only on quantitative values in this study, we can also create synthetic images with any contrast-weighing based on quantitative synthetic MRI,[16] as opposed to acquiring contrast-weighted images separately.[77] Regarding future perspectives, comparison of quantitative synthetic MRI with other sequences sensitive to cortical lesion detection would be interesting.[78,79] Further, multiparametric quantitative information acquired with quantitative synthetic MRI may improve the prediction of contrast enhancement and the quality of automatic lesion segmentation, as were previously performed by using contrast-weighted images.[80,81]

There were some limitations to our study. First, we did not consider the clinical background of the subjects, including race, hypertension, smoking, and drinking. However, the effect of these factors on T1 and T2 values in the brain have been reported to be minimal.[82] A future study is warranted to investigate the age-related changes in the brain using quantitative synthetic MRI considering the effects of these factors. The second limitation was the cross-sectional design of this study. A longitudinal design may enable us to avoid biases related to the inter-individual variability of brain tissues.[54] Third, we used quadratic regression models to fit the quantitative values to age. Even though a quadratic regression model is conventional and well represented in the literature, it has been revealed that the choice of age range affects the peak age of the quadratic curve.[83] Caution is warranted when comparing the peak ages reported for studies performed on populations with different age ranges. Nonetheless, our results would serve as a reference of quantitative values derived from 2D quantitative synthetic MRI for the age range investigated in the current study (ie, 21–86). Lastly, subjects 65 years or older were recruited differently from the younger subjects. This study design and the larger density of subjects in the 65 to 75 age range compared with the other age ranges may have introduced some biases in the results.

CONCLUSIONS

This study showed age-related changes in quantitative values and brain volumes derived from quantitative synthetic MRI. The results

were overall in line with those measured by other methods. Differences may lie in the quantitative technique, analysis method, and age range used in each study. Reference values according to age demonstrated in this study may be useful for discriminating brain disorders from healthy brains using quantitative synthetic MRI.

REFERENCES

1. Lee SM, Choi YH, You SK, et al. Age-related changes in tissue value properties in children: simultaneous quantification of relaxation times and proton density using synthetic magnetic resonance imaging. *Invest Radiol*. 2018;53:236–245.
2. McAllister A, Leach J, West H, et al. Quantitative synthetic MRI in children: normative intracranial tissue segmentation values during development. *AJNR Am J Neuroradiol*. 2017;38:2364–2372.
3. Kim HG, Moon WJ, Han J, et al. Quantification of myelin in children using multiparametric quantitative MRI: a pilot study. *Neuroradiology*. 2017;59: 1043–1051.
4. Wang J, Shaffer ML, Eslinger PJ, et al. Maturational and aging effects on human brain apparent transverse relaxation. *PLoS One*. 2012;7:e31907.
5. Kumar R, Delshad S, Macey PM, et al. Development of T2-relaxation values in regional brain sites during adolescence. *Magn Reson Imaging*. 2011;29:185–193.
6. Hasan KM, Walimuni IS, Abid H, et al. Multimodal quantitative magnetic resonance imaging of thalamic development and aging across the human lifespan: implications to neurodegeneration in multiple sclerosis. *J Neurosci*. 2011;31: 16826–16832.
7. Hasan KM, Walimuni IS, Kramer LA, et al. Human brain atlas-based volumetry and relaxometry: application to healthy development and natural aging. *Magn Reson Med*. 2010;64:1382–1389.
8. Siemonsen S, Finsterbusch J, Matschke J, et al. Age-dependent normal values of T2* and T2' in brain parenchyma. *AJNR Am J Neuroradiol*. 2008;29:950–955.
9. Faizy TD, Kumar D, Broocks G, et al. Age-related measurements of the myelin water fraction derived from 3D multi-echo GRASE reflect myelin content of the cerebral white matter. *Sci Rep*. 2018;8:14991.
10. Bouhrara M, Rejimon AC, Cortina LE, et al. Adult brain aging investigated using BMC-mcDESPOT-based myelin water fraction imaging. *Neurobiol Aging*. 2020; 85:131–139.
11. Arshad M, Stanley JA, Raz N. Adult age differences in subcortical myelin content are consistent with protracted myelination and unrelated to diffusion tensor imaging indices. *Neuroimage*. 2016;143:26–39.
12. Cercignani M, Giulietti G, Dowell NG, et al. Characterizing axonal myelination within the healthy population: a tract-by-tract mapping of effects of age and gender on the fiber g-ratio. *Neurobiol Aging*. 2017;49:109–118.
13. Slater DA, Melie-Garcia L, Preisig M, et al. Evolution of white matter tract microstructure across the life span. *Hum Brain Mapp*. 2019;40:2252–2268.
14. Vinke EJ, Huizinga W, Bergtholdt M, et al. Normative brain volumetry derived from different reference populations: impact on single-subject diagnostic assessment in dementia. *Neurobiol Aging*. 2019;84:9–16.
15. Hagiwara A, Fujita S, Ohno Y, et al. Variability and standardization of quantitative imaging: monoparametric to multiparametric quantification, radiomics, and artificial intelligence [published online ahead of print June 24, 2020]. *Invest Radiol*.
16. Hagiwara A, Warntjes M, Hori M, et al. SyMRI of the brain: rapid quantification of relaxation rates and proton density, with synthetic MRI, automatic brain segmentation, and myelin measurement. *Invest Radiol*. 2017;52:647–657.
17. Warntjes JB, Leinhard OD, West J, et al. Rapid magnetic resonance quantification on the brain: optimization for clinical usage. *Magn Reson Med*. 2008;60:320–329.
18. Badve C, Yu A, Rogers M, et al. Simultaneous T 1 and T 2 brain Relaxometry in asymptomatic volunteers using magnetic resonance fingerprinting. *Tomography*. 2015;1:136–144.
19. Park M, Moon Y, Han SH, et al. Myelin loss in white matter hyperintensities and normal-appearing white matter of cognitively impaired patients: a quantitative synthetic magnetic resonance imaging study. *Eur Radiol*. 2019;29:4914–4921.
20. Hagiwara A, Kamagata K, Shimoji K, et al. White matter abnormalities in multiple sclerosis evaluated by quantitative synthetic MRI, diffusion tensor imaging, and neurite orientation dispersion and density imaging. *AJNR Am J Neuroradiol*. 2019;40:1642–1648.
21. Granberg T, Uppman M, Hashim F, et al. Clinical feasibility of synthetic MRI in multiple sclerosis: a diagnostic and volumetric validation study. *AJNR Am J Neuroradiol*. 2016;37:1023–1029.
22. Saccenti L, Hagiwara A, Andica C, et al. Myelin measurement using quantitative magnetic resonance imaging: a correlation study comparing various imaging techniques in patients with multiple sclerosis. *Cell*. 2020;9:393.
23. Duchaussoy T, Budzik JF, Norberciak L, et al. Synthetic T2 mapping is correlated with time from stroke onset: a future tool in wake-up stroke management? *Eur Radiol*. 2019;29:7019–7026.
24. Warntjes M, Blystad I, Tisell A, et al. Synthesizing a contrast-enhancement map in patients with high-grade gliomas based on a postcontrast MR imaging quantification only. *AJNR Am J Neuroradiol*. 2018;39:2194–2199.
25. Kang KM, Choi SH, Hwang M, et al. Application of synthetic MRI for direct measurement of magnetic resonance relaxation time and tumor volume at multiple time points after contrast administration: preliminary results in patients with brain metastasis. *Korean J Radiol*. 2018;19:783–791.
26. Andica C, Hagiwara A, Hori M, et al. Aberrant myelination in patients with Sturge-Weber syndrome analyzed using synthetic quantitative magnetic resonance imaging. *Neuroradiology*. 2019;61:1055–1066.
27. West J, Warntjes JB, Lundberg P. Novel whole brain segmentation and volume estimation using quantitative MRI. *Eur Radiol*. 2012;22:998–1007.
28. Warntjes M, Engström M, Tisell A, et al. Modeling the presence of myelin and edema in the brain based on multi-parametric quantitative MRI. *Front Neurol*. 2016;7:16.
29. Ouellette R, Mangeat G, Polyak I, et al. Validation of rapid magnetic resonance myelin imaging in multiple sclerosis. *Ann Neurol*. 2020;87:710–724.
30. Warntjes JBM, Persson A, Berge J, et al. Myelin detection using rapid quantitative MR imaging correlated to macroscopically registered Luxol fast blue-stained brain specimens. *AJNR Am J Neuroradiol*. 2017;38:1096–1102.
31. Hagiwara A, Hori M, Kamagata K, et al. Myelin measurement: comparison between simultaneous tissue Relaxometry, magnetization transfer saturation index, and T1w/T2w ratio methods. *Sci Rep*. 2018;8:10554.
32. Simmons A, Westman E, Muehlboeck S, et al. MRI measures of Alzheimer's disease and the AddNeuroMed study. *Ann N Y Acad Sci*. 2009;1180:47–55.
33. Kim GH, Lee JH, Seo SW, et al. Hippocampal volume and shape in pure subcortical vascular dementia. *Neurobiol Aging*. 2015;36:485–491.
34. Rovira A, Leon A. MR in the diagnosis and monitoring of multiple sclerosis: an overview. *Eur J Radiol*. 2008;67:409–414.
35. Fotenos AF, Snyder AZ, Girton LE, et al. Normative estimates of cross-sectional and longitudinal brain volume decline in aging and AD. *Neurology*. 2005;64: 1032–1039.
36. Taki Y, Thyreau B, Kinomura S, et al. Correlations among brain gray matter volumes, age, gender, and hemisphere in healthy individuals. *PLoS One*. 2011; 6:e22734.
37. Abe O, Yamasue H, Aoki S, et al. Aging in the CNS: comparison of gray/white matter volume and diffusion tensor data. *Neurobiol Aging*. 2008;29:102–116.
38. Sullivan EV, Pfefferbaum A. Neuroradiological characterization of normal adult ageing. *Br J Radiol*. 2007;80 Spec No 2:S99–S108.
39. Lemaitre H, Crivello F, Grassiot B, et al. Age- and sex-related effects on the neuroanatomy of healthy elderly. *Neuroimage*. 2005;26:900–911.
40. Scahill RI, Frost C, Jenkins R, et al. A longitudinal study of brain volume changes in normal aging using serial registered magnetic resonance imaging. *Arch Neurol*. 2003;60:989–994.
41. Vågberg M, Ambarki K, Lindqvist T, et al. Brain parenchymal fraction in an age-stratified healthy population—determined by MRI using manual segmentation and three automated segmentation methods. *J Neuroradiol*. 2016;43: 384–391.
42. Hagiwara A, Hori M, Cohen-Adad J, et al. Linearity, bias, intrascanner repeatability, and interscanner reproducibility of quantitative multidynamic multiecho sequence for rapid simultaneous Relaxometry at 3 T: a validation study with a standardized phantom and healthy controls. *Invest Radiol*. 2019;54:39–47.
43. Someya Y, Tamura Y, Kaga H, et al. Skeletal muscle function and need for long-term care of urban elderly people in Japan (the Bunkyo health study): a prospective cohort study. *BMJ Open*. 2019;9:e031584.
44. Akaike H. A new look at the statistical model identification. *IEEE Trans Automat Control*. 1974;19:716–723.
45. Levesque IR, Pike GB. Characterizing healthy and diseased white matter using quantitative magnetization transfer and multicomponent T(2) relaxometry: a unified view via a four-pool model. *Magn Reson Med*. 2009;62:1487–1496.
46. Saito N, Sakai O, Ozonoff A, et al. Relaxo-volumetric multispectral quantitative magnetic resonance imaging of the brain over the human lifespan: global and regional aging patterns. *Magn Reson Imaging*. 2009;27:895–906.
47. Ambarki K, Lindqvist T, Wahlin A, et al. Evaluation of automatic measurement of the intracranial volume based on quantitative MR imaging. *AJNR Am J Neuroradiol*. 2012;33:1951–1956.
48. Warntjes JB, Tisell A, Landtblom AM, et al. Effects of gadolinium contrast agent administration on automatic brain tissue classification of patients with multiple sclerosis. *AJNR Am J Neuroradiol*. 2014;35:1330–1336.
49. Neeb H, Zilles K, Shah NJ. Fully-automated detection of cerebral water content changes: study of age- and gender-related H_2O patterns with quantitative MRI. *Neuroimage*. 2006;29:910–922.

50. Maniega SM, Valdes Hernandez MC, Clayden JD, et al. White matter hyperintensities and normal-appearing white matter integrity in the aging brain. *Neurobiol Aging*. 2015;36:909–918.
51. Stüber C, Morawski M, Schäfer A, et al. Myelin and iron concentration in the human brain: a quantitative study of MRI contrast. *Neuroimage*. 2014;93(pt 1): 95–106.
52. Wu M, Kumar A, Yang S. Development and aging of superficial white matter myelin from young adulthood to old age: mapping by vertex-based surface statistics (VBSS). *Hum Brain Mapp*. 2016;37:1759–1769.
53. Ding XQ, Kucinski T, Wittkugel O, et al. Normal brain maturation characterized with age-related T2 relaxation times: an attempt to develop a quantitative imaging measure for clinical use. *Invest Radiol*. 2004;39:740–746.
54. Gracien RM, Nurnberger L, Hok P, et al. Evaluation of brain ageing: a quantitative longitudinal MRI study over 7 years. *Eur Radiol*. 2017;27:1568–1576.
55. Okubo G, Okada T, Yamamoto A, et al. Relationship between aging and T 1 relaxation time in deep gray matter: a voxel-based analysis. *J Magn Reson Imaging*. 2017;46:724–731.
56. Stikov N, Boudreau M, Levesque IR, et al. On the accuracy of T1 mapping: searching for common ground. *Magn Reson Med*. 2015;73:514–522.
57. Hurtz S, Woo E, Kebets V, et al. Age effects on cortical thickness in cognitively normal elderly individuals. *Dement Geriatr Cogn Dis Extra*. 2014;4:221–227.
58. Heier LA, Bauer CJ, Schwartz L, et al. Large Virchow-Robin spaces: MR-clinical correlation. *AJNR Am J Neuroradiol*. 1989;10:929–936.
59. Fujita S, Hagiwara A, Hori M, et al. 3D quantitative synthetic MRI-derived cortical thickness and subcortical brain volumes: scan-rescan repeatability and comparison with conventional T1-weighted images. *J Magn Reson Imaging*. 2019; 50:1834–1842.
60. Fujita S, Hagiwara A, Hori M, et al. Three-dimensional high-resolution simultaneous quantitative mapping of the whole brain with 3D-QALAS: an accuracy and repeatability study. *Magn Reson Imaging*. 2019;63:235–243.
61. Fujita S, Hagiwara A, Otsuka Y, et al. Deep learning approach for generating MRA images from 3D quantitative synthetic MRI without additional scans. *Invest Radiol*. 2020;55:249–256.
62. Steen RG, Gronemeyer SA, Taylor JS. Age-related changes in proton T1 values of normal human brain. *J Magn Reson Imaging*. 1995;5:43–48.
63. Cho S, Jones D, Reddick WE, et al. Establishing norms for age-related changes in proton T1 of human brain tissue in vivo. *Magn Reson Imaging*. 1997;15: 1133–1143.
64. Bender AR, Volkle MC, Raz N. Differential aging of cerebral white matter in middle-aged and older adults: a seven-year follow-up. *Neuroimage*. 2016;125: 74–83.
65. Brickman AM, Meier IB, Korgaonkar MS, et al. Testing the white matter retrogenesis hypothesis of cognitive aging. *Neurobiol Aging*. 2012;33:1699–1715.
66. Reisberg B, Franssen EH, Souren LE, et al. Evidence and mechanisms of retrogenesis in Alzheimer's and other dementias: management and treatment import. *Am J Alzheimers Dis Other Demen*. 2002;17:202–212.
67. Fotenos AF, Mintun MA, Snyder AZ, et al. Brain volume decline in aging: evidence for a relation between socioeconomic status, preclinical Alzheimer disease, and reserve. *Arch Neurol*. 2008;65:113–120.
68. Hofman PA, Kemerink GJ, Jolles J, et al. Quantitative analysis of magnetization transfer images of the brain: effect of closed head injury, age and sex on white matter. *Magn Reson Med*. 1999;42:803–806.
69. Cowell PE, Turetsky BI, Gur RC, et al. Sex differences in aging of the human frontal and temporal lobes. *J Neurosci*. 1994;14:4748–4755.
70. Buckner RL, Head D, Parker J, et al. A unified approach for morphometric and functional data analysis in young, old, and demented adults using automated atlas-based head size normalization: reliability and validation against manual measurement of total intracranial volume. *Neuroimage*. 2004;23:724–738.
71. Mortamet B, Zeng D, Gerig G, et al. Effects of healthy aging measured by intracranial compartment volumes using a designed MR brain database. *Med Image Comput Comput Assist Interv*. 2005;8(pt 1):383–391.
72. Farokhian F, Yang C, Beheshti I, et al. Age-related gray and white matter changes in normal adult brains. *Aging Dis*. 2017;8:899–909.
73. Ge Y, Grossman RI, Babb JS, et al. Age-related total gray matter and white matter changes in normal adult brain, part I: volumetric MR imaging analysis. *AJNR Am J Neuroradiol*. 2002;23:1327–1333.
74. Walhovd KB, Fjell AM, Reinvang I, et al. Effects of age on volumes of cortex, white matter and subcortical structures. *Neurobiol Aging*. 2005;26:1261–1270; discussion 1275–1268.
75. Jernigan TL, Archibald SL, Fennema-Notestine C, et al. Effects of age on tissues and regions of the cerebrum and cerebellum. *Neurobiol Aging*. 2001;22: 581–594.
76. Benes FM. Myelination of cortical-hippocampal relays during late adolescence. *Schizophr Bull*. 1989;15:585–593.
77. Kazmierczak PM, Duhrsen M, Forbrig R, et al. Ultrafast brain magnetic resonance imaging in acute neurological emergencies: diagnostic accuracy and impact on patient management. *Invest Radiol*. 2020;55:181–189.
78. Beck ES, Gai N, Filippini S, et al. Inversion recovery susceptibility weighted imaging with enhanced T2 weighting at 3 T improves visualization of subpial cortical multiple sclerosis lesions. *Invest Radiol*. 2020;Publish Ahead of Print.
79. Eichinger P, Hock A, Schön S, et al. Acceleration of double inversion recovery sequences in multiple sclerosis with compressed sensing. *Invest Radiol*. 2019;54: 319–324.
80. Kleesiek J, Morshuis JN, Isensee F, et al. Can virtual contrast enhancement in brain MRI replace gadolinium?: a feasibility study. *Invest Radiol*. 2019;54: 653–660.
81. Fartaria MJ, Sati P, Todea A, et al. Automated detection and segmentation of multiple sclerosis lesions using ultra-high-field MP2RAGE. *Invest Radiol*. 2019;54: 356–364.
82. Breger RK, Yetkin FZ, Fischer ME, et al. T1 and T2 in the cerebrum: correlation with age, gender, and demographic factors. *Radiology*. 1991;181:545–547.
83. Fjell AM, Walhovd KB, Westlye LT, et al. When does brain aging accelerate? Dangers of quadratic fits in cross-sectional studies. *Neuroimage*. 2010;50: 1376–1383.

Magnetic Resonance Imaging 78 (2021) 90–97

Contents lists available at ScienceDirect

Magnetic Resonance Imaging

journal homepage: www.elsevier.com/locate/mri

Original Contribution

Effect of hybrid of compressed sensing and parallel imaging on the quantitative values measured by 3D quantitative synthetic MRI: A phantom study

Syo Murata [a], Akifumi Hagiwara [a,*], Shohei Fujita [a,b], Takuya Haruyama [a], Shimpei Kato [a,b], Christina Andica [a], Koji Kamagata [a], Masami Goto [c], Masaaki Hori [a,d], Masami Yoneyama [e], Nozomi Hamasaki [a], Haruyoshi Hoshito [a], Shigeki Aoki [a]

[a] Department of Radiology, Juntendo University Hospital, Tokyo, Japan
[b] Department of Radiology, Graduate School of Medicine, The University of Tokyo, Tokyo, Japan
[c] Department of Radiological Technology, Faculty of Health Science, Juntendo University, Tokyo, Japan
[d] Department of Radiology, Toho University Omori Medical Center, Tokyo, Japan
[e] MR Clinical Science, Philips Japan, Tokyo, Japan

ARTICLE INFO

Keywords:
Compressed sensing
Quantitative MRI
Sensitivity encoding
Synthetic MRI
Three-dimensional imaging

ABSTRACT

Introduction: Recently, three-dimensional (3D) quantitative synthetic magnetic resonance imaging (MRI), which quantifies tissue properties and creates multiple contrast-weighted images, has been enabled by 3D-quantification using an interleaved Look-Locker acquisition sequence with a T2 preparation pulse (3D-QALAS). However, the relatively long scan time has hindered its introduction into clinical practice. A hybrid of compressed sensing and parallel imaging (Compressed sensing-sensitivity encoding: CS-SENSE) can accelerate 3D-QALAS; however, whether CS-SENSE affects the quantitative values acquired by 3D-QALAS remains unexplored. Therefore, this study aimed to examine the effects of reduction factors of CS-SENSE (R_{CSS}) on the quantitative values derived from 3D-QALAS, by assessing the signal-to-noise ratio (SNR) of the quantitative maps, as well as accuracy (linearity and bias) and repeatability of measured quantitative values.

Methods: In this study, the ISMRM/NIST standardized phantom was scanned on a 1.5-T MRI scanner with 3D-QALAS using R_{CSS} in the range between 1 and 3, with intervals of 0.2, and between 3 and 10 with intervals of 0.5. The T1, T2, and proton density (PD) values were calculated from the imaging data. For each quantitative value, the SNR, the coefficient of determination (R^2) of a linear regression model, the error rate, and the within-subject coefficient of variation (wCV) were calculated for each R_{CSS} and compared.

Results: Within the clinically-relevant dynamic range of the brain of T1 and T2 (T1: 200–1400 ms; T2; 50–400 ms) and PD value of 15–100% calculated from 3D-QALAS, the effects of R_{CSS} on quantitative values was small between 1 and 2.8, with SNR $\geqq$ 10, $R^2 \geqq 0.9$, error rate $\leqq$ 10%, and wCV $\leqq$ 10%, except for T2 values of 186.1 and 258.4 ms.

Conclusions: CS-SENSE enabled the reduction of the scan time of 3D-QALAS by 63.5% (R_{CSS} = 2.8) while maintaining the SNR of quantitative maps and accuracy and repeatability of the quantitative values.

1. Introduction

Quantitative synthetic magnetic resonance imaging (MRI) is an imaging technique that quantifies tissue properties and creates multiple contrast-weighted images based on the measured quantitative values obtained from a single scan [1,2]. The utility of the quantitative synthetic MRI has been shown for normal development, aging, and disease evaluation [3–7]. However, the multi-dynamic multi-echo sequence, which is conventionally used for quantitative synthetic MRI, is a two-dimensional (2D) multi-slice sequence and has a relatively low resolution in the slice direction compared to three-dimensional (3D) acquisition [8,9]. Recently, 3D-quantification using an interleaved Look-Locker acquisition sequence with a T2 preparation pulse (3D-QALAS) sequence has been developed for simultaneous quantification of T1 and T2 in

* Corresponding author at: Department of Radiology, Juntendo University School of Medicine, 1-2-1, Hongo, Bunkyo-ku, Tokyo 113-8421, Japan.
E-mail address: a-hagiwara@juntendo.ac.jp (A. Hagiwara).

https://doi.org/10.1016/j.mri.2021.01.001
Received 6 August 2020; Received in revised form 8 December 2020; Accepted 8 January 2021
Available online 11 January 2021

cardiac imaging [10–12] (Fig. 1). 3D quantitative synthetic MRI using 3D-QALAS showed high accuracy and precision not only in the heart, [11] but also in the human brain [13]. However, the relatively long scan time of 3D-QALAS has hindered its introduction into clinical practice [8]. One solution would be the usage of compressed sensing (CS), which is an acceleration technique of acquiring highly undersampled data and reconstructing an image with little degradation in image quality compared with the fully-sampled data [14–16]. CS is particularly compatible with images that have an inherently sparse nature, such as MR cholangiography and MR angiography. However, 3D-QALAS is less sparse than these MR imaging techniques. A combination of CS and parallel imaging developed to accelerate less sparse images [17] may be useful for accelerating 3D-QALAS and maintain the image quality. Compressed sensing-sensitivity encoding (CS-SENSE) [18–23] is a hybrid technique by combining SENSE, a version of the parallel imaging technique using phased array coils, and CS. The CS-SENSE adopts a variable density compressive sampling system that automatically optimizes the balance between random-basis and SENSE-basis sampling for each acquisition [17]. Morita et al. reported that CS-SENSE reduced the acquisition time of 3D isotropic T2-weighted turbo spin-echo imaging of the lumbar spine by 39.2%, without sacrificing image quality compared to SENSE alone [17]. To the best of our knowledge, there has not been a report about how the CS-SENSE affects the quantitative values derived from 3D-QALAS. Therefore, the purpose of this study was to examine the effect of reduction factors of CS-SENSE (R_{CSS}) on the quantitative values derived from 3D-QALAS, by assessing signal-to-noise ratio (SNR) of quantitative maps, and the accuracy (linearity and bias) and repeatability of measured quantitative values.

2. Materials and methods

2.1. Devices and scan parameters

In this study, the ISMRM/NIST system phantom (High Precision Devices, Inc., Boulder, Colorado, USA) [24,25], which consists of three layers of sphere arrays with known T1, T2, and proton density (PD) values, was scanned on a 1.5-T MRI scanner (A patched R5.4.1 Ingenia, Philips Healthcare, Best, The Netherlands) equipped with a 15-channel head coil, after being placed in the center of the gantry for more than 30 min. After imaging, the temperature of the phantom was measured and recorded. Imaging was performed with 3D-QALAS with R_{CSS} changed between 1 and 3 with intervals of 0.2, and between 3 and 10 with intervals of 0.5 (the denoising level is "no" for all R_{CSS}). Each image session was performed 10 times at intervals of at least 24 h. All scan parameters were the same for all R_{CSS}. Prior to this study, it was confirmed that there was no remarkable difference between the images obtained from R_{CSS} = no and $R_{CSS} = 1$; hence, the image obtained from $R_{CSS} = 1$ was used as the reference image. The other scan parameters of the 3D-QALAS were as follows: axial acquisition; repetition time/echo time, 6.6/3.0 ms; inversion delay times, 100, 1000, 1900, and 2800 ms; T2-prep echo time, 100 ms; field-of-view, 250 × 250 × 120 mm; voxel size, 1.5 × 1.5 × 1.5 mm^3; flip angle, 4°; receiver bandwidth, 230 Hz/pixel; number of average, 1. Coil sensitivity was corrected using the constant level appearance (CLEAR) technique. Table 1 summarizes the acquisition time for each R_{CSS}.

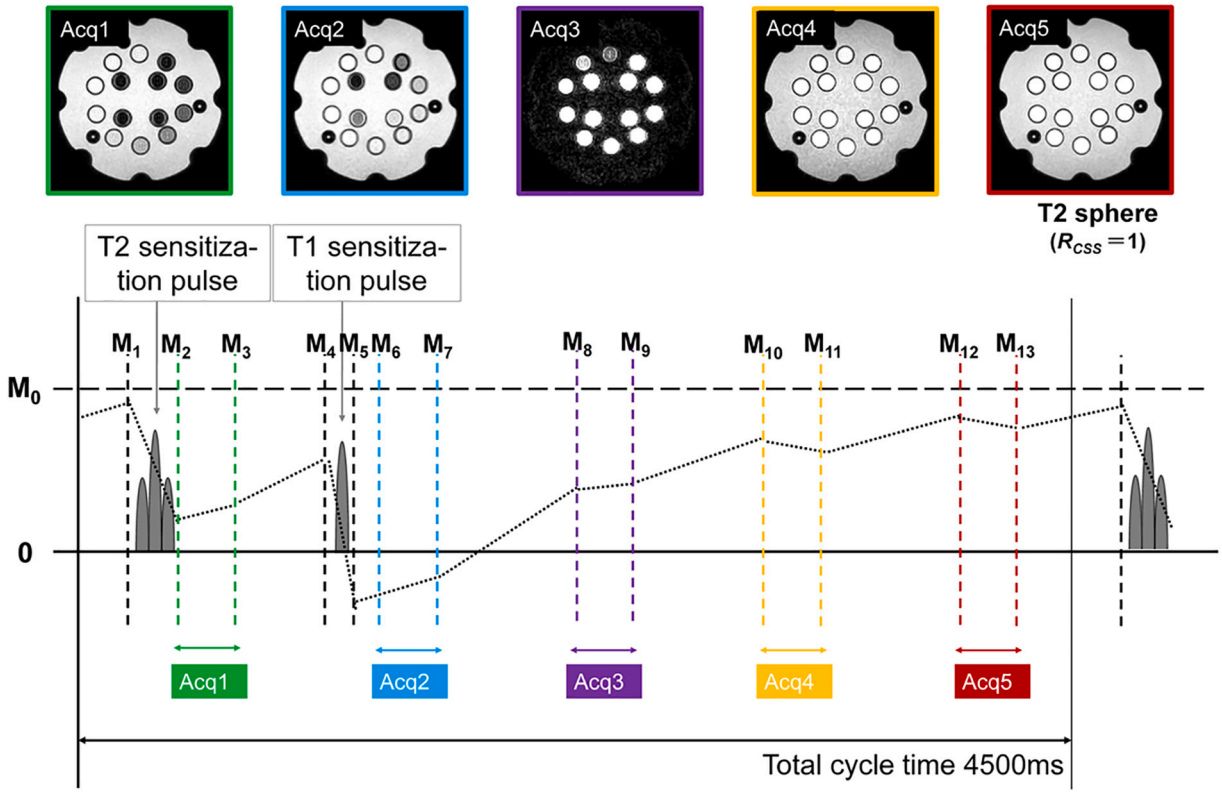

Fig. 1. Diagrammatic overview of the acquisition kernel for 3D-QALAS. The typical Mz magnetization evolution is displayed as the dotted line. Before the first acquisition, a T2-sensitizing phase decreases the Mz magnetization proportional to the T2 relaxation. Before the second acquisition, a T1-sensitizing phase is applied to invert the Mz magnetization. The total cycle time is 4500 ms and 5 source images can be acquired in one series.

Table 1
The acquisition times for each R_{CSS}.

R_{css}	1	1.2	1.4	1.6	1.8	2	2.2	2.4	2.6	2.8	3	3.5	4
Scan time[min]	6:51	5:44	4:59	4:23	3:56	3:29	3:11	2:57	2:44	2:30	2:21	2:03	1:45
R_{css}	4.5	5	5.5	6	6.5	7	7.5	8	8.5	9	9.5	10	
Scan time[min]	1:36	1:27	1:18	1:09	1:05	1:00	0:56	0:51	0:51	0:47	0:42	0:42	

Abbreviation: R_{CSS}, reduction factor of compressed sensing-sensitivity encoding.

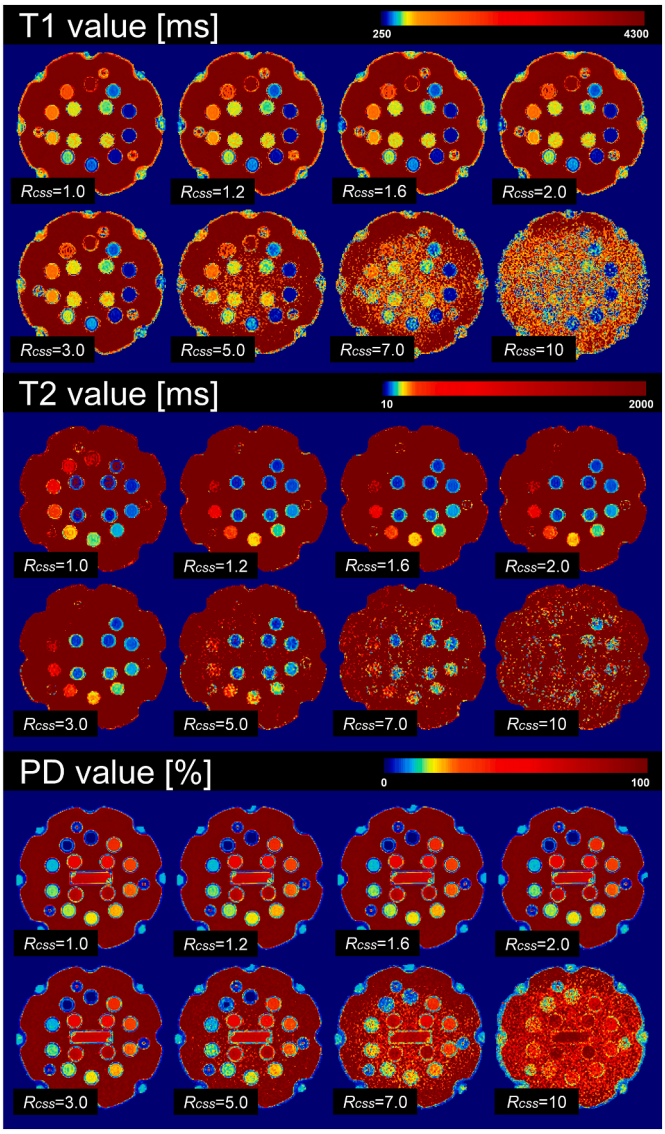

Fig. 2. T1, T2, and PD maps of the ISMRM/NIST system phantom in cross sections of the 14 array spheres of T1, T2, and PD, respectively, with varying values of reduction factors of CS-SENSE (R_{CSS}) are shown. Only representative values of R_{CSS} are shown.

2.2. Data analysis

T1, T2, and PD values [26] were calculated from the imaging data using SyMRI software (version 0.45.11, SyntheticMR, Linköping, Sweden) (Fig. 2). A spherical volume of interest (VOI) with a diameter of 10 mm was placed for each quantitative value at the center of the spheres in the phantom using ITK-SNAP (version 3.6.0) software, and the mean values were recorded. In this study, 7 T1 and 12 T2 spheres in the ISMRM/NIST phantom with values within the computable dynamic ranges of SyMRI software (250–4300 ms and 10–2000 ms, respectively) were analyzed; for PD, all 14 spheres were analyzed. The average and standard deviation (SD) were calculated for each quantitative value acquired 10 times. In order to evaluate the noise of the quantitative maps, the SNR was calculated by dividing the mean value by the SD for the R_{CSS} for each quantitative value, because the background signal, such as that of air, was set at zero by the correction method for coil sensitivity (i.e., CLEAR). Each SNR was averaged over 10 measurements. Heat maps of SNR with respect to the change of the R_{CSS} were created. The heat maps of SNR were classified into an increase of ≧100, ≧50, ≧10, ≧5, ≧3, ≧1, and < 1.

To evaluate the linearity, linear regression analysis was performed for quantitative values acquired with each R_{CSS} compared with the reference values acquired with R_{CSS} of 1. Here, 7 T1 spheres and 12 T2 spheres with T1 and T2 values within the clinically-relevant dynamic ranges of the brain (200–1400 ms and 50–400 ms, respectively) were used [13].

The assumption of linearity was deemed met with the coefficient of determination (R^2) higher than 0.90 [27].

Bias introduced by CS-SENSE was evaluated as an error rate, comparing the average values between the quantitative value acquired with each R_{CSS} and the reference value acquired with the R_{CSS} of 1. The error rates of T1, T2, and PD values were calculated by the following equations:

$$Error\ rate_{T1} = \left|T1_{(R_{CSS}=1)} - T1_{(R_{CSS}=i)}\right| \times 100 / T1_{(R_{CSS}=1)} \quad (1)$$

$$Error\ rate_{T2} = \left|T2_{(R_{CSS}=1)} - T2_{(R_{CSS}=i)}\right| \times 100 / T2_{(R_{CSS}=1)} \quad (2)$$

$$Error\ rate_{PD} = \left|PD_{(R_{CSS}=1)} - PD_{(R_{CSS}=i)}\right| \times 100 / PD_{(R_{CSS}=1)} \quad (3)$$

We also investigated the repeatability of the quantitative values using a within-subject coefficient of variation (wCV) for each quantitative value calculated over 10 measurements. The heat maps of the error rate and wCV of the T1, T2, and PD values with varying R_{CSS} were created and classified into an increase of >75%, ≦75%, ≦50%, ≦30%, ≦10%, ≦5%, and ≦1%.

3. Results

The temperature of the phantom after image acquisition was 20.1 ± 0.2 °C (mean ± SD). For PD values 5% and 10% (true values), the measurement yielded approximately 0%; It was not possible to calculate the SNR, error rates, and wCV and were excluded in the calculation of R^2.

In the examination of the noise, visual inspection of the quantitative maps with varying R_{CSS} revealed that the noise was more remarkable with the larger R_{CSS} values (Fig. 2). Heat maps of SNR for each

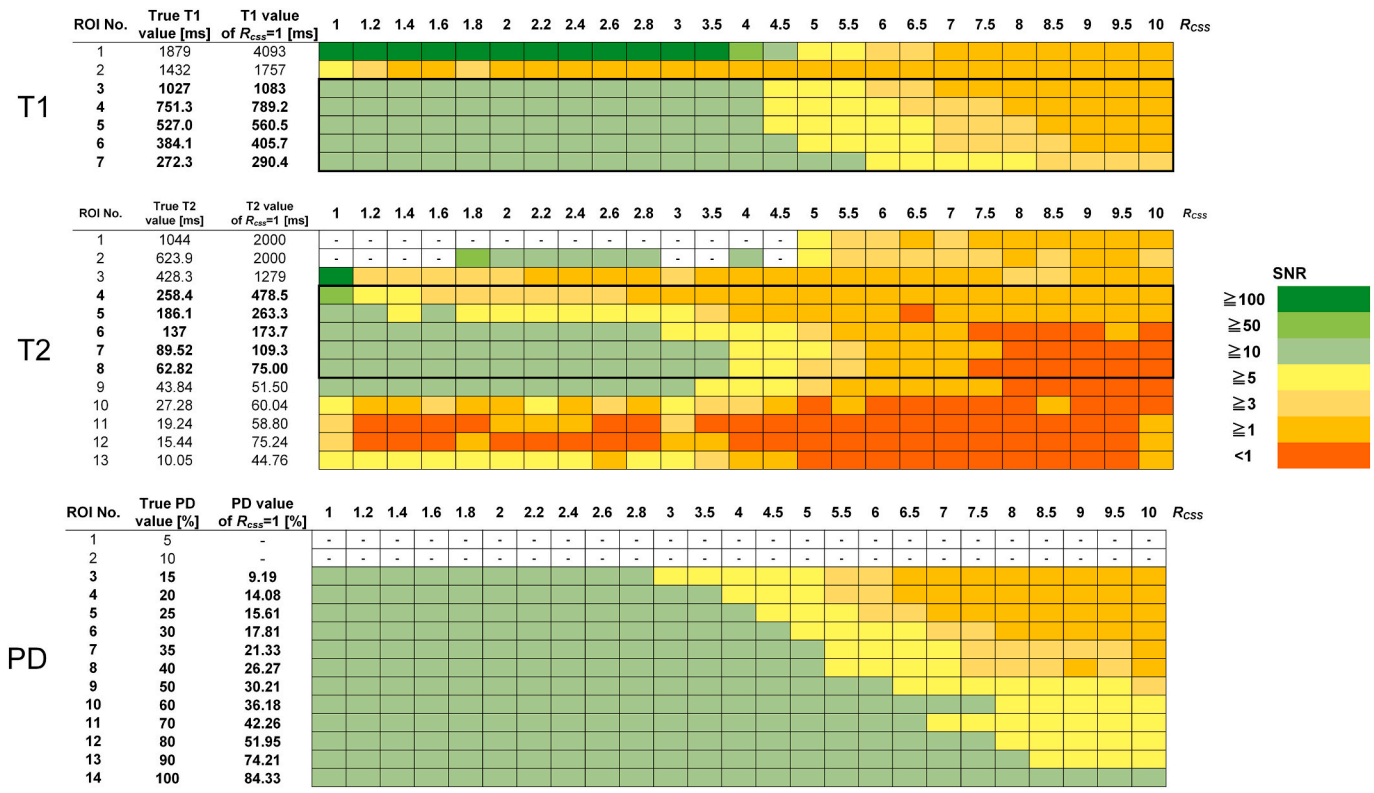

Fig. 3. Heat maps of the SNR of T1 values, T2 values, and PD values. The horizontal axis shows the value of reduction factors of CS-SENSE (R_{CSS}), and the vertical axis shows the VOI number, the true value of the quantitative value, and the reference value measured at $R_{CSS} = 1$. The areas surrounded by the thick black border are areas of quantitative values within the clinically-relevant dynamic range of the brain (T1 value: 200–1400 ms, T2 value: 50–400 ms) [13]. The SNR of PD values with 5% and 10% are omitted because of a calculation error of PD values on SyMRI software. Also, the SNR of some spheres with T2 values of 623.9 and 1044 ms are omitted. All T2 values within these VOIs were calculated as 2000 ms (upper limit) by SyMRI software and SD became 0. The SNR of the sphere with T1 value of 1879 ms was large overall because most of the T1 values in the VOI were calculated near the upper limit of the dynamic range and the SD was small.

Table 2
The coefficient of determination for each quantitative value.

R_{css}	1.2	1.4	1.6	1.8	2.0	2.2	2.4	2.6	2.8	3.0	3.5	4.0
T1 value	**1.000**	**0.993**	**1.000**	**1.000**	**1.000**	**0.999**	**0.996**	**0.997**	**0.999**	**0.989**	**0.992**	**0.983**
T2 value	**1.000**	**0.999**	**0.989**	**1.000**	**0.998**	**0.999**	**0.998**	**0.998**	**0.999**	**0.986**	**0.992**	**0.990**
PD value	**1.000**	**1.000**	**1.000**	**1.000**	**1.000**	**1.000**	**1.000**	**1.000**	**1.000**	**1.000**	**1.000**	**1.000**
R_{css}	4.5	5.0	5.5	6.0	6.5	7.0	7.5	8.0	8.5	9.0	9.5	10.0
T1 value	**0.970**	**0.976**	**0.982**	**0.967**	**0.954**	**0.930**	**0.905**	**0.904**	0.831	0.783	0.860	0.758
T2 value	**0.969**	**0.980**	**0.940**	**0.939**	**0.920**	0.867	0.832	0.712	0.689	0.751	0.720	0.698
PD value	**1.000**	**0.999**	**0.996**	**0.990**	**0.983**	**0.970**	**0.958**	**0.947**	**0.938**	**0.932**	**0.919**	**0.908**

Note. Assumption of linearity was deemed met with $R^2 > 0.9$ and the $R^2 > 0.9$ is represented as bold face. For T1 and T2 values, the coefficient of determination was calculated from the data of the true value within the dynamic range of SyMRI software (T1 value = 250–4300 ms, T2 value = 10–2000 ms). For PD values, the coefficient of determination was calculated excluding the 5% and 10% data that were not appropriately calculated on SyMRI software.
Abbreviation: R^2, coefficient of determination; R_{CSS}, reduction factor of compressed sensing-sensitivity encoding.

quantitative value (Fig. 3) showed that the SNR of T1, T2, and PD values tended to decrease as R_{CSS} increased. In the T1 and T2 values, the SNR was higher in spheres having quantitative values inside the clinically-relevant dynamic range of the brain. The SNR was more than 10 for $R_{CSS} = 4.0$ or less when the spheres with T1 values ranged between 272.3 and 1027 ms. The SNR was more than 10 for $R_{CSS} = 2.8$ or less in the spheres with T2 values in the range of 43.84–137.0 ms. For spheres with PD value of 15% or more, the SNR was more than 10 when R_{CSS} was 2.8 or less.

For the assessment of the linearity, the R^2 was higher than 0.9 with R_{CSS} of 8 or less, 6.5 or less, and 10 or less, respectively, for T1, T2, and PD (Table 2). Overall, the T1 values were similar to the reference values regardless of R_{CSS}, except for T1 values of 1432 and 1879 ms (true values outside the clinically-relevant dynamic range of the brain), showing deviation from the reference values with R_{CSS} of 5.0% or higher (Fig. 4). Within the clinically-relevant dynamic range of the brain (50–400 ms), the T2 values tended to be estimated higher as the R_{CSS} increased. The entire range of PD values tended to be higher as the R_{CSS} increased.

To examine bias, heat maps of the error rate for each quantitative value (Fig. 5) showed that the error rate of T1, T2, and PD values tended to increase as R_{CSS} increased. For the T1 and T2 values, the error rates were larger in spheres having quantitative values outside the clinically-relevant dynamic range of the brain than inside. The error rates were less than 10% for $R_{CSS} = 6.0$ or less in the spheres with T1 value in the range 272.3–1027 ms. The error rates were less than 10% for $R_{CSS} = 2.8$ or less in the spheres with T2 value in the range 43.84–186.1 ms. For spheres of PD value 15% or more, the error rates were less than 10% when R_{CSS} was 5.5 or less.

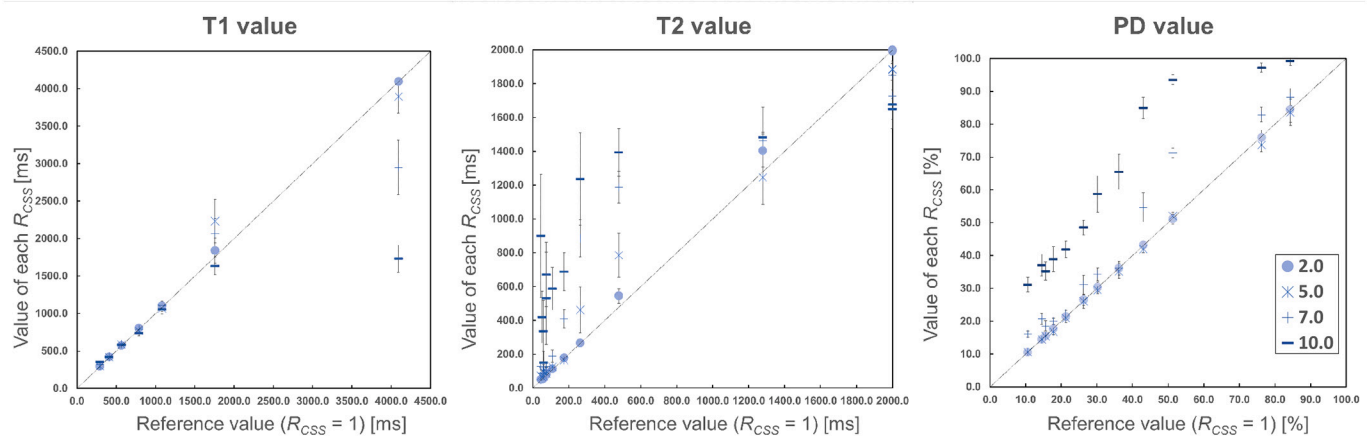

Fig. 4. Scatter plots of T1, T2, and PD values in various reduction factors of CS-SENSE (R_{CSS}) against the reference values ($R_{CSS} = 1$). Only representative values of R_{CSS} are shown. Error bars represent ±1 standard deviation. Solid lines indicate identity.

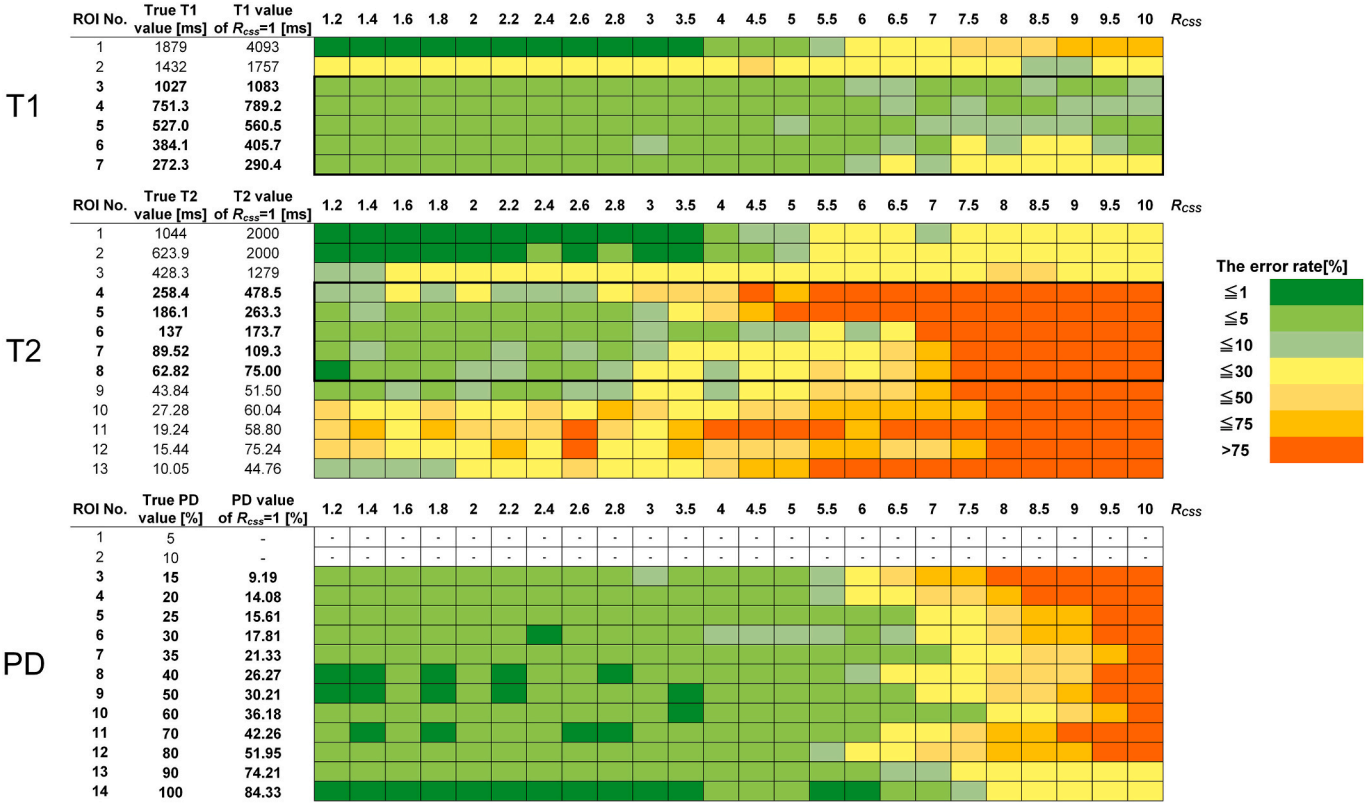

Fig. 5. The Heat maps of the error rates of T1, T2 values, and PD values. The horizontal axis shows the value of reduction factors of CS-SENSE (R_{CSS}), and the vertical axis shows the VOI number, the true value of the quantitative value, and the reference value measured at $R_{CSS} = 1$. The areas surrounded by the thick black border are areas of quantitative values within the clinically-relevant dynamic range of the brain (T1 value: 200–1400 ms, T2 value: 50–400 ms) [13]. The error rate of PD values with 5% and 10% are omitted because of the measurement error of PD values on the SyMRI software.

For the assessment of repeatability, heat maps of the wCV for each quantitative value (Fig. 6) showed that the wCVs in all spheres of T1 values inside the clinically-relevant dynamic range of the brain were less than 10%. The wCV of T2 values tended to increase as R_{CSS} increased. The wCVs in all spheres of PD value with 15% or more were less than 10%.

4. Discussion

In this study, we examined the effect of R_{CSS} on the quantitative values derived from 3D-QALAS by assessing noise, linearity, bias, and repeatability. The SNR, the error rates, and the wCV of PD values with 5% and 10% could not be properly estimated because of the automatic masking of low values in the SyMRI software. However, precise quantification of tissues with such small PD values is of little importance in the clinical setting [13,28].

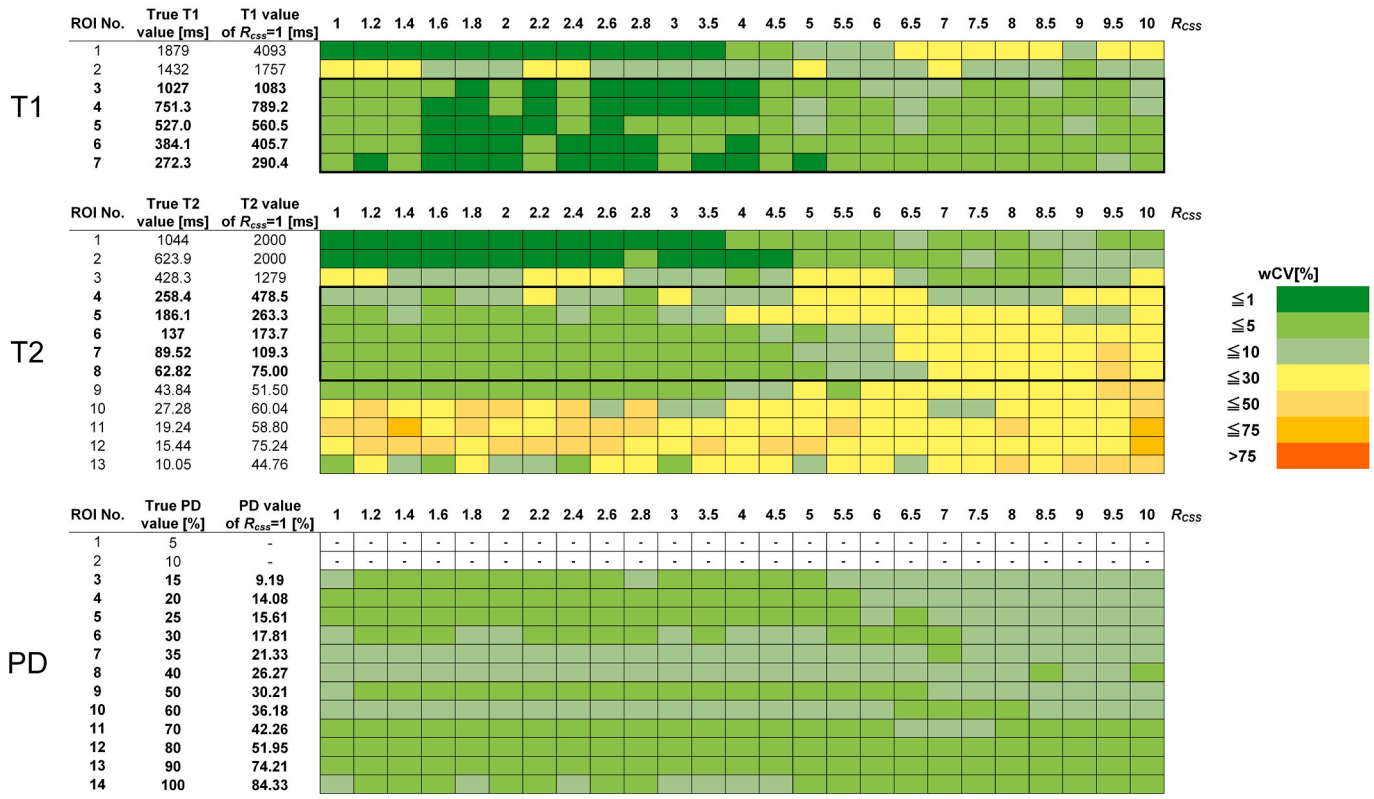

Fig. 6. The heat maps of the within-subject coefficient of variation (wCV) of T1, T2, and PD values. The horizontal axis shows the value of reduction factors of CS-SENSE (R_{CSS}), and the vertical axis shows the VOI number, the true value of the quantitative value, and the reference value measured at $R_{CSS} = 1$. The areas surrounded by the thick black border are areas of quantitative values within the clinically-relevant dynamic range of the brain (T1 value: 200–1400 ms, T2 value: 50–400 ms) [13]. The wCV of PD values with 5% and 10% are omitted because of the measurement error of PD values on the SyMRI software.

The noise of the quantitative maps was more evident with larger R_{CSS}. The SNR of T1, T2, and PD maps tended to decrease as R_{CSS} increased. This may be because of a decrease in the sampling data volume of the original k-space acquired by 3D-QALAS [20,22]. In the clinically-relevant dynamic range of the brain, except for the T2 values of 186.1 and 258.4 ms, the SNR of T2 value tended to be smaller than that of T1 value: the SNR of T2 value was 10 or more when R_{CSS} was 2.8 or less, while the SNR of T1 value was 10 or more when R_{CSS} was 4.0 or less. Even though the SNR is generally inversely proportional to the square root of a reduction factor, this relationship is expected to be invalid for quantitative maps acquired with 3D-QALAS because each map is based on a combination of five source images. In this study, the SNR of the quantitative maps within a VOI was defined as the mean value divided by the SD. However, evaluating SNR only for the quantitative maps is problematic because the software that handles the calculation of relaxation parameters may threshold values that are considered out of range, which may result in artificially low SD and high SNR for the phantom measurements. Hence, as a supplementary study, the SNR of the five source images was measured and evaluated (Supplementary document 1). However, since 3D-QALAS uses an inversion recovery pulse and the signals can come close to zero, it is difficult to set an acceptable range in the SNR measurement of the source images. It is difficult to distinguish between the effects of longitudinal relaxation and those of R_{CSS} on SNR. Therefore, in this study, the acceptable range of R_{CSS} was determined from the SNR of quantitative maps.

Linearities of the T1 and T2 values were not maintained when R_{CSS} was large which can be explained by the increase in error rates. Outside of the clinically-relevant dynamic range of the brain the T1 values fluctuated more than within the clinically-relevant dynamic range of the brain when the R_{CSS} was large. The reason may be that the SyMRI software was optimized to characterize human brain tissue. With increasing R_{CSS}, T2 value lost linearity at smaller values of R_{CSS} than T1 and PD. The PD values tended to be estimated higher as the R_{CSS} increased. The cause of this phenomenon is unclear but may be because of the salt-and-pepper like noise in PD maps accompanying the calculation errors in the quantitative value at high R_{CSS}.

In the examination of bias, the error rate of T1, T2, and PD values tended to increase as R_{CSS} increased. It is likely because when R_{CSS} increased, the error and variation in the measured quantitative value became larger because of decreases in the SNR of the original images of 3D-QALAS [22]. The error rate of the T2 value was generally larger than that of the T1 value. Also, among T1, T2, and PD, the error rate of T2 value exceeded 10% at smaller R_{CSS}. In the spheres with T2 values of 623.9 and 1044 ms, and with T1 value of 1879 ms, the error rates were small, even though they were outside the clinically-relevant dynamic range of the brain. This may be because most of the pixels in the VOI for T1 and T2 were calculated near the upper limit of the dynamic range of SyMRI software regardless of R_{CSS}.

In the examination of repeatability, the wCVs in the entire range of T1 values inside the clinically-relevant dynamic range of the brain and in PD values of 15% or more were less than 10%. The wCV of T2 values within the clinically-relevant dynamic range of the brain tended to increase as R_{CSS} increased. In the spheres with T2 values of 623.9 and 1044 ms, and with T1 value of 1879 ms, the wCV was small although they were outside the clinically-relevant dynamic range of the brain. Again, this may be because most of the pixels in the VOI for T1 and T2 were calculated near the upper limit of the dynamic range of SyMRI software.

In summary, the effect of R_{CSS} on quantitative values within the clinically-relevant dynamic range of the brain of T1 and T2 (T1 value: 200–1400 ms, T2 value: 50–400 ms) and PD value of 15% or over (enough number of protons as signal source) calculated from 3D

quantitative synthetic MRI was small (between 1 and 2.8), with SNR ≧10, R^2 ≧0.9, the error rate ≦10%, and wCV ≦10%, except for T2 values of 186.1 and 258.4 ms. It is considered that one of the reasons why the measurement accuracy of the long T2 value was low is that 3D-QALAS has few measurement points for calculating the T2 value. In addition, since SyMRI software targets values close to living organisms, it is possible that it is not good at measuring long T2 values. In contrast, it was reported that the T2 value of normal GM is 95 ± 8 ms and normal WM is 72 ± 4 ms [29]. Hence, low measurement accuracy of T2 values of 186.1 and 258.4 ms may not largely affect a clinical brain scan. Therefore, using CS-SENSE, it may be possible to reduce the imaging time by 63.5% with R_{CSS} of 2.8, while maintaining the SNR of quantitative maps and accuracy and precision of the quantitative values.

The major limitation of this study is that it was based on only phantom experiments. Human brain and phantom have different sparsity and contrast. CS presents with a higher noise processing efficiency for data with higher sparsity [17,30]. CS-SENSE is more effective in higher-contrast areas, while the efficiency decreases in lower contrast regions [17]. The difference in sparsity and contrast between the human brain and phantom may affect the calculation process of CS-SENSE. Thus, the results of our study will require verification using human anatomical data relevant to clinical application. Further, this study focused on quantitative values and did not qualitatively examine the image quality. Care should be taken when using each quantitative map for visual diagnosis. In addition, Philips' commercial CS-SENSE technology—"Compressed SENSE"—does not clearly separate CS and SENSE. In Compressed SENSE, the ratio of CS and SENSE to reduction factor is automatically optimized based on (1) the positional relationship between the target part and coil, (2) the size of the region of interest, and (3) geometry factor information. Therefore, in this study, it was not possible to separately determine the effect of CS and SENSE on the quantitative values.

5. Conclusion

The effect of CS-SENSE on T1, T2, and PD values calculated from 3D quantitative synthetic MRI was small with R_{CSS} of 1–2.8. By using CS-SENSE, it may be possible to reduce the imaging time by 63.5% while maintaining the SNR of quantitative maps and accuracy and repeatability of the quantitative value.

Conflict of interests

Masami Yoneyama is currently employed at Philips Japan. The authors declare that they have no other conflicts of interest.

Grant support

This work was supported by Japan Agency for Medical Research and Development (AMED) under Grant Number JP19lk1010025h9902; JSPS KAKENHI grant number 19K17150, 19K17177, 18K07692, and 18H02772; Health, Labour and Welfare Policy Research Grants for Research on Region Medical; a Grant-in-Aid for Special Research in Subsidies for ordinary expenses of private schools from The Promotion and Mutual Aid Corporation for Private Schools of Japan; Brain/MINDS Beyond program from AMED Grant Number JP19dm0307024 and JP19dm0307101.

Appendix A. Supplementary data

Supplementary data to this article can be found online at https://doi.org/10.1016/j.mri.2021.01.001.

References

[1] Maitra R, Besag J. Bayesian reconstruction in synthetic magnetic resonance imaging. SPIE 1998;3459:39–47. https://doi.org/10.1117/12.323818.
[2] Hagiwara A, Warntjes M, Hori M, Andica C, Nakazawa M, Kumamaru KK, et al. SyMRI of the brain: rapid quantification of relaxation rates and proton density, with synthetic MRI, automatic brain segmentation, and myelin measurement. Invest Radiol 2017;52(10):647–57. https://doi.org/10.1097/RLI.0000000000000365.
[3] Andica C, Hagiwara A, Hori M, Haruyama T, Fujita S, Maekawa T, et al. Aberrant myelination in patients with Sturge-weber syndrome analyzed using synthetic quantitative magnetic resonance imaging. Neuroradiology 2019;61(9):1055–66. https://doi.org/10.1007/s00234-019-02250-9.
[4] McAllister A, Leach J, West H, Jones B, Zhang B, Serai S. Quantitative synthetic MRI in children: normative intracranial tissue segmentation values during development. Am J Neuroradiol 2017;38(12):2364–72. https://doi.org/10.3174/ajnr.A5398.
[5] Hagiwara A, Kamagata K, Shimoji K, Yokoyama K, Andica C, Hori M, et al. White matter abnormalities in multiple sclerosis evaluated by quantitative synthetic MRI, diffusion tensor imaging, and Neurite orientation dispersion and density imaging. Am J Neuroradiol 2019;40(10):1642–8. https://doi.org/10.3174/ajnr.A6209.
[6] Fujita S, Nakazawa M, Hagiwara A, Ueda R, Horita M, Maekawa T, et al. Estimation of gadolinium-based contrast agent concentration using quantitative synthetic MRI and its application to brain metastases: a feasibility study. Magn Reson Med Sci 2019;18(4):260–4. https://doi.org/10.2463/mrms.mp.2018-0119.
[7] Lee SM, Choi YH, You S-K, Lee WK, Kim WH, Kim HJ, et al. Age-related changes in tissue value properties in children: simultaneous quantification of relaxation times and proton density using synthetic magnetic resonance imaging. Invest Radiol 2018;53(4):236–45. https://doi.org/10.1097/RLI.0000000000000435.
[8] Fujita S, Hagiwara A, Hori M, Warntjes M, Kamagata K, Fukunaga I, et al. 3D quantitative synthetic MRI-derived cortical thickness and subcortical brain volumes: scan-rescan repeatability and comparison with conventional T1 -weighted images. J Magn Reson Imaging 2019;50(6):1834–42. https://doi.org/10.1002/jmri.26744.
[9] Fujita S, Hagiwara A, Otsuka Y, Hori M, Takei N, Hwang K-P, et al. Deep learning approach for generating MRA images from 3D quantitative synthetic MRI without additional scans. Invest Radiol 2020;55(4):249–56. https://doi.org/10.1097/RLI.0000000000000628.
[10] Kvernby S, Warntjes M, Carlhäll C-J, Engvall J, Ebbers T. 3D-quantification using an interleaved look-locker acquisition sequence with T2-prep pulse (3D-QALAS). J Cardiovasc Magn Reson 2014;16(1):1–2. https://doi.org/10.1186/1532-429X-16-S1-O82.
[11] Kvernby S, Warntjes MJ, Haraldsson H, Carlhall CJ, Engvall J, Ebbers T. Simultaneous three-dimensional myocardial T1 and T2 mapping in one breath hold with 3D-QALAS. J Cardiovasc Magn Reson 2014;16(1):1–14. https://doi.org/10.1186/s12968-014-0102-0.
[12] Kvernby S, Warntjes M, Engvall J, Carlhäll C-J, Ebbers T. Clinical feasibility of 3D-QALAS–single breath-hold 3D myocardial T1-and T2-mapping. Magn Reson Imaging 2017;38:13–20. https://doi.org/10.1016/j.mri.2016.12.014.
[13] Fujita S, Hagiwara A, Hori M, Warntjes M, Kamagata K, Fukunaga I, et al. Three-dimensional high-resolution simultaneous quantitative mapping of the whole brain with 3D-QALAS: an accuracy and repeatability study. Magn Reson Imaging 2019;63:235–43. https://doi.org/10.1016/j.mri.2019.08.031.
[14] Chang C-H, Ji J. Compressed sensing MRI with multichannel data using multicore processors. Magn Reson Med 2010;64(4):1135–9. https://doi.org/10.1002/mrm.22481.
[15] Geethanath S, Reddy R, Konar AS, Imam S, Sundaresan R, RB DR, et al. Compressed sensing MRI: a review. Crit Rev Biomed Eng 2013;41(3):183–204. https://doi.org/10.1615/CritRevBiomedEng.2014008058.
[16] Jaspan ON, Fleysher R, Lipton ML. Compressed sensing MRI: a review of the clinical literature. Br J Radiol 2015;88(1056):20150487. https://doi.org/10.1259/bjr.20150487.
[17] Morita K, Nakaura T, Maruyama N, Iyama Y, Oda S, Utsunomiya D, et al. Hybrid of compressed sensing and parallel imaging applied to three-dimensional isotropic T₂−weighted Turbo spin-echo MR imaging of the lumbar spine. Magn Reson Med Sci 2020;19(1):48–55. https://doi.org/10.2463/mrms.mp.2018-0132.
[18] Pruessmann KP, Weiger M, Scheidegger MB, Boesiger P. SENSE: sensitivity encoding for fast MRI. Magn Reson Med 1999;42(5):952–62. https://doi.org/10.1002/(SICI)1522-2594(199911)42:5<952::AID-MRM16>3.0.CO;2-S.
[19] Vranic JE, Cross NM, Wang Y, Hippe DS, de Weerdt E, Mossa-Basha M. Compressed sensing-sensitivity encoding (CS-SENSE) accelerated brain imaging: reduced scan time without reduced image quality. AJNR Am J Neuroradiol 2019;40(1):92–8. https://doi.org/10.3174/ajnr.A5905.
[20] Liang D, Liu B, Wang J, Ying L. Accelerating SENSE using compressed sensing. Magn Reson Med 2009;62(6):1574–84. https://doi.org/10.1002/mrm.22161.
[21] Lustig M, Donoho D, Pauly JM. Sparse MRI: the application of compressed sensing for rapid MR imaging. Magn Reson Med 2007;58(6):1182–95. https://doi.org/10.1002/mrm.21391.
[22] Liu F, Duan Y, Peterson BS, Kangarlu A. Compressed sensing MRI combined with SENSE in partialk-space. Phys Med Biol 2012;57(21):N391–403. https://doi.org/10.1088/0031-9155/57/21/n391.
[23] Huang F, Chen Y, Yin W, Lin W, Ye X, Guo W, et al. A rapid and robust numerical algorithm for sensitivity encoding with sparsity constraints: self-feeding sparse SENSE. Magn Reson Med 2010;64(4):1078–88. https://doi.org/10.1002/mrm.22504.

[24] Russek S, Boss M, Jackson E, Jennings D, Evelhoch J, Gunter J, et al. Characterization of NIST/ISMRM MRI system phantom. In: In Proceedings of the 20th Annual Meeting of ISMRM. Melbourne, Victoria, Austraia; 2012. p. 2456.
[25] Keenan KE, Stupic KF, Boss MA, Russek SE, Chenevert TL, Prasad PV, et al. Multi-site, multi-vendor comparison of T1 measurement using ISMRM/NIST system phantom. In: In Proceedings of the 24th Annual Meeting of ISMRM. Singapore; 2016. p. 3290.
[26] Tofts PS. PD: proton density of tissue water. In: Quantitative MRI of the Brain: Measuring Changes Caused by Disease. Chichester, UK: Wiley & Sons; 2003. p. 85–110. https://doi.org/10.1002/0470869526.ch4.
[27] Hagiwara A, Fujita S, Ohno Y, Aoki S. Variability and standardization of quantitative imaging: monoparametric to multiparametric quantification, radiomics, and artificial intelligence. Invest Radiol 2020;55(9):601–16. https://doi.org/10.1097/RLI.0000000000000666.
[28] Hagiwara A, Hori M, Cohen-Adad J, Nakazawa M, Suzuki Y, Kasahara A, et al. Linearity, Bias, Intrascanner repeatability, and Interscanner reproducibility of quantitative multidynamic multiecho sequence for rapid simultaneous Relaxometry at 3 T: a validation study with a standardized phantom and healthy controls. Invest Radiol 2019;54(1):39–47. https://doi.org/10.1097/rli.0000000000000510.
[29] Stanisz GJ, Odrobina EE, Pun J, Escaravage M, Graham SJ, Bronskill MJ, et al. T1, T2 relaxation and magnetization transfer in tissue at 3T. Magn Reson Med 2005;54(3):507–12. https://doi.org/10.1002/mrm.20605.
[30] Küstner T, Würslin C, Gatidis S, Martirosian P, Nikolaou K, Schwenzer N, et al. MR image reconstruction using a combination of compressed sensing and partial Fourier acquisition: ESPReSSo. IEEE Trans Med Imaging 2016;35(11):2447–58. https://doi.org/10.1109/TMI.2016.2577642.

OPEN

Accelerated Isotropic Multiparametric Imaging by High Spatial Resolution 3D-QALAS With Compressed Sensing

A Phantom, Volunteer, and Patient Study

Shohei Fujita, MD,† Akifumi Hagiwara, MD, PhD,* Naoyuki Takei, MS,‡ Ken-Pin Hwang, PhD,§ Issei Fukunaga, PhD,* Shimpei Kato, MD,*† Christina Andica, MD, PhD,* Koji Kamagata, MD, PhD,* Kazumasa Yokoyama, MD,|| Nobutaka Hattori, MD, PhD,|| Osamu Abe, MD, PhD,† and Shigeki Aoki, MD, PhD**

Objectives: The aims of this study were to develop an accelerated multiparametric magnetic resonance imaging method based on 3D-quantification using an interleaved Look-Locker acquisition sequence with a T2 preparation pulse (3D-QALAS) combined with compressed sensing (CS) and to evaluate the effect of CS on the quantitative mapping, tissue segmentation, and quality of synthetic images.

Materials and Methods: A magnetic resonance imaging system phantom, containing multiple compartments with standardized T1, T2, and proton density (PD) values; 10 healthy volunteers; and 12 patients with multiple sclerosis were scanned using the 3D-QALAS sequence with and without CS and conventional contrast-weighted imaging. The scan times of 3D-QALAS with and without CS were 5:56 and 11:11, respectively. For healthy volunteers, brain volumetry and myelin estimation were performed based on the measured T1, T2, and PD. For patients with multiple sclerosis, the mean T1, T2, PD, and the amount of myelin in plaques and contralateral normal-appearing white matter (NAWM) were measured. Simple linear regression analysis and Bland-Altman analysis were performed for each metric obtained from the datasets with and without CS. To compare overall image quality and structural delineations on synthetic and conventional contrast-weighted images, case-control randomized reading sessions were performed by 2 neuroradiologists in a blinded manner.

Results: The linearity of both phantom and volunteer measurements in T1, T2, and PD values obtained with and without CS was very strong (R^2 = 0.9901–1.000). The tissue segmentation obtained with and without CS also had high linearity (R^2 = 0.987–0.999). The quantitative tissue values of the plaques and NAWM obtained with CS showed high linearity with those without CS (R^2 = 0.967–1.000). There were no significant differences in overall image quality between synthetic contrast-weighted images obtained with and without CS (P = 0.17–0.99).

Conclusions: Multiparametric imaging of the whole brain based on 3D-QALAS can be accelerated using CS while preserving tissue quantitative values, tissue segmentation, and quality of synthetic images.

Key Words: 3D-QALAS, compressed sensing, magnetic resonance imaging, parallel imaging, quantitative mapping, synthetic MRI

(*Invest Radiol* 2020;00: 00–00)

Quantitative magnetic resonance imaging (MRI) techniques allow objective rather than the current subjective evaluation.[1] Simultaneous multiparametric mapping techniques provide tissue property maps, including T1 and T2 maps, in a single scan, and have attracted much attention owing to their high acquisition efficiency.[2–4] Their clinical feasibility in the evaluation of the brain has been reported in many studies assessing and characterizing brain conditions, such as multiple sclerosis (MS) and brain tumors, as well as brain development.[5–9] Rapid myelin estimation has also been developed on the basis of multiparametric mapping techniques.[10,11] These techniques were validated on histology[12,13] and compared with other myelin imaging techniques,[14,15] and applied to diseases such as MS and Sturge-Weber syndrome.[16,17] From the quantitative maps acquired in a single time-efficient scanning process, multiparametric mapping techniques have the potential to reduce the long MRI time by producing any of the contrast-weighted images, such as T1-weighted, T2-weighted, and fluid-attenuated inversion recovery (FLAIR) images.[2]

In recent years, there has been an increasing interest in improving the spatial resolution of multiparametric mapping techniques by acquiring the whole-brain data in 3D. One of these techniques, namely, 3D-quantification using an interleaved Look-Locker acquisition sequence with a T2 preparation pulse (3D-QALAS) sequence, has been applied to the brain and has demonstrated high repeatability and reproducibility both in vivo and in vitro.[18–20] Compared with a 2D acquisition, a 3D acquisition enables thinner slices, which are contiguous and more amenable to interpolation in the slice direction. Furthermore, a 3D acquisition with isotropic resolution would allow visualization of the subject from any orientation, enabling improved depiction of structures and characterization of the pathologies. Despite their potential, current 3D quantitative imaging techniques require long acquisition times, thereby limiting its clinical use.

Compressed sensing (CS) is an acceleration technique that reconstructs images from subsampled data by leveraging the sparsity of the image.[21] Using incoherently undersampled k-space data, CS accelerates image acquisition by reducing the amount of data acquired and filling in unacquired data points in a manner that minimizes the incoherent artifacts. Generally, CS and 3D acquisitions are highly compatible owing to the compressibility of the volume data and the increased incoherence offered in the added spatial dimension. It has been observed previously that utilization of CS in combination with parallel imaging (PI), another acceleration technique, could achieve a higher

Received for publication August 10, 2020; and accepted for publication, after revision, October 3, 2020.

From the *Department of Radiology, Juntendo University; †Department of Radiology, The University of Tokyo; ‡MR Applications and Workflow, GE Healthcare Japan, Tokyo, Japan; §Department of Radiology, MD Anderson Cancer Center, Houston, TX; and ||Department of Neurology, Juntendo University, Tokyo, Japan.

Conflicts of interest and sources of funding: N.T. is an employee of GE Healthcare Japan. This work was supported by Japan Agency for Medical Research and Development under grant number JP19lk1010025h9902; JSPS KAKENHI grant numbers 19K17150, 19K17177, 18H02772, and 18K07692; Health, Labor and Welfare Policy Research Grants for Research on Region Medical; and a grant-in-aid for special research in subsidies for ordinary expenses of private schools from The Promotion and Mutual Aid Corporation for Private Schools of Japan; Brain/MINDS beyond program from Japan Agency for Medical Research and Development grant numbers JP19dm0307024 and JP19dm0307101.

Correspondence to: Akifumi Hagiwara, MD, PhD, Department of Radiology, Juntendo University School of Medicine, 2-1-1, Hongo, Bunkyo-ku, Tokyo, Japan, 113-8421. E-mail: a-hagiwara@juntendo.ac.jp.

Supplemental digital contents are available for this article. Direct URL citations appear in the printed text and are provided in the HTML and PDF versions of this article on the journal's Web site (www.investigativeradiology.com).

ISSN: 0020-9996/20/0000–0000
DOI: 10.1097/RLI.0000000000000744

acceleration rate than application of either method alone,[22] while preserving the quality of 3D MRI scans.[23–27] However, the effects of CS on quantitative values obtained with multiparametric mapping techniques, including 3D-QALAS, have been largely unexplored.[28–30]

This study aimed to propose an application of CS combined with PI to the 3D-QALAS sequence, a multiparametric mapping technique, to enable the whole-brain 1-mm isotropic T1, T2, and proton density (PD) quantification and myelin estimation within a span of 6 minutes. We assessed whether an accelerated acquisition could allow reliable T1, T2, and PD quantification and myelin estimation while maintaining the quality of the contrast-weighted images. Furthermore, we also compared 3D-QALAS with and without CS and conventional contrast-weighted images in patients with MS for assessing lesion quantitative values and diagnostic image quality.

MATERIALS AND METHODS

Magnetic Resonance Imaging Settings

We implemented an acceleration technique that serially combined CS and data-driven PI to 3D-QALAS according to the procedure proposed by King et al.[31,32] The overview of the procedure is illustrated in Supplemental Digital Content Figure 1, http://links.lww.com/RLI/A587 showing a reconstruction based on the serial combination of CS and PI. K-space data were first undersampled in a Gaussian random distribution outside of a fully sampled small area around the center of the k-space. The standard deviation of the Gaussian random distribution was set to 0.28, which was determined empirically. The unacquired points in this step were filled with CS reconstruction to restore uniformly undersampled k-space data. This CS reconstruction was performed on each channel of the coil, based on a total variation sparsifying transform and an iterative nonlinear conjugate gradient method described by Lustig et al.[21] The image from the undersampled k-space data was reconstructed by using the following formula:

$$\hat{m} = argmin \, \|\Psi m\|_1 \; s.t. \; \|E\hat{m} - y\|_2^2 \leq \varepsilon$$

where $\hat{m}$ is the reconstructed image, Ψ is sparsifying transform, m is all the pixel values, y is the acquired k-space data samples, E is coil and gradient encoding, and ε is noise standard deviation in y controlling the fidelity of the reconstruction to the measured data. The maximum number of CS iteration was set to 10. Finally, PI reconstruction based on the Autocalibrating Reconstruction for Cartesian imaging method[33] restored the rest of the k-space on each coil channel, followed by fast Fourier transform and sum of squares reconstruction.

A 3-T scanner (Discovery 750w; GE Healthcare, Waukesha, WI) with a 32-channel head coil was utilized for image acquisition in the standardized phantom and all the human subjects. To evaluate the effects of CS on quantitative mapping and tissue segmentation, we have acquired 3D-QALAS with and without CS for each subject. The sequence used a Look-Locker inversion acquisition-based technique with acquisition parameters shown in Table 1. The imaging parameters were all identical between the 2 acquisitions, except for the incorporation of CS acceleration with an undersampling factor of 1.9, corresponding to 53% of the full k-space points. The scan times for the 3D-QALAS sequence with and without CS were 5:56 and 11:11, respectively. For patient data acquisition, we additionally acquired conventional T1-weighted, T2-weighted, and FLAIR images for comparison of diagnostic image quality (Table 1).

Phantom Study

A standardized NIST/ISMRM (National Institute of Standards and Technology/International Society for Magnetic Resonance in Medicine) system phantom (High Precision Devices, Inc, Boulder, CO) with 3 layers of sphere arrays was designed to assess a range of specific T1, T2, and PD values (Supplemental Digital Content Table 1, http://links.lww.com/RLI/A587).[34] Each sphere was filled with either $NiCl_2$ or $MnCl_2$ doped water. Over a period of 1 month, this phantom was scanned 10 times on different days. Moreover, to minimize the effects of motion on the measurements, the phantom was positioned 30 minutes before commencement of each scan. The images produced by 3D-QALAS sequences were postprocessed using a prototype version 0.45.5 of SyMRI software (SyntheticMR, Linköping, Sweden) to generate T1, T2, and PD maps. A spherical volume of interest (VOI) was manually placed at the center of each sphere on the T1, T2, and PD maps, and the respective mean values were recorded. To minimize the effects of the artifacts near

TABLE 1. Sequence Parameters for 3D-QALAS With CS, 3D-QALAS Without CS, and Conventional Imaging

	3D-QALAS		Conventional		
Parameter	**With CS**	**Without CS**	**T1WI**	**T2WI**	**FLAIR**
Acquisition dimension	3D	3D	3D	2D	2D
Acquisition plane	Axial		Axial	Axial	Axial
Repetition time, ms	8.6		7.7	4500	9000
Echo time, ms	3.5		3.1	122.3	120
Flip angle, degree	4		11	—	—
Bandwidth, Hz/pixel	244.1		244.1	162.8	195.3
Field of view, mm	256 × 205 × 146		256 × 218	240 × 240	240 × 240
Matrix	256 × 205 × 146		256 × 218	320 × 224	320 × 224
Interpolated matrix	512 × 410 × 292		256 × 218	320 × 224	320 × 224
Slice thickness, mm	1 (0.5)*		1 (0.5)*	4	4
Slice gap, mm	—		—	1	1
Parallel imaging (ARC)	2 × 1		2 × 1	2 × 1	2 × 1
Compressed sensing	1.9	—	—	—	—
Acquisition time	5:56	11:11	5:45	2:06	2:33

*Slice thicknesses after zero-fill interpolation.

3D-QALAS, 3D-quantification using an interleaved Look-Locker acquisition sequence with a T2 preparation pulse; ARC, Autocalibrating Reconstruction for Cartesian imaging; CS, compressed sensing; FLAIR, fluid-attenuated inversion recovery images; T1WI, T1-weighted imaging; T2WI, T2-weighted imaging.

the edge of the sphere, the spherical VOI was set to 10-mm diameter within each sphere with an inner diameter of 15 mm.

In Vivo Quantitative Assessment

This study was approved by the local institutional review board. Ten healthy volunteers (7 men, 3 women; mean age ± standard deviation, 29.7 ± 4.7 years) and 12 patients with relapsing-remitting MS (1 man, 11 women; 42.3 ± 10.9 years) diagnosed using the McDonald criteria[35] were included in the study. Patient characteristics were as follows: disease duration, 11.3 ± 7.8 years; and median Expanded Disability Status Scale score, 1.0 (range, 0–4.5). Written informed consent was obtained from all the study participants. In addition to T1, T2, and PD maps as described in the phantom study, SyMRI software was used to create myelin volume fraction (MVF) maps for each human subject based on a 4-compartment model.[10] To compare the quantitative T1, T2, PD, and MVF values in vivo, quantitative maps that were derived from 3D-QALAS with and without CS were compared by adopting semiautomated VOI analyses proposed by Hagiwara et al.[36] In brief, 16 VOIs were automatically created in the Montreal Neurological Institute space and registered to each subject's space using the FMRIB Software Library (http://fsl.fmrib.ox.ac.uk/fsl/fslwiki/FSL).[37] Of the 16 VOIs, 8 were gray matter (frontal, parietal, temporal and occipital GM, insula, caudate, putamen, and thalamus) and 8 were white matter (frontal, parietal, temporal, and occipital WM, genu and splenium of the corpus callosum, internal capsules, and middle cerebellar peduncles). Circular ROIs with a diameter of 5 mm were manually placed by a neuroradiologist with 6 years of experience (S.F.) in the anterior horns of the lateral ventricles. The ROIs were carefully placed so as not to include the brain parenchyma or the choroid plexus. To topologically show the differences in T1, T2, and PD values obtained with and without CS, the difference divided by their mean on a group level in the Montreal Neurological Institute space was calculated in a voxelwise manner.

For 3D-QALAS data with and without CS, voxelwise T1, T2, and PD values were used to derive the following tissue fraction maps: WM, white matter; GM, gray matter; and CSF, cerebrospinal fluid fraction maps.[38] By integrating the tissue fraction maps across all voxels, the following tissue volumes were calculated: WM volume, GM volume, CSF volume, myelin volume, and intracranial volume. The effects of CS on the tissue fraction maps obtained with 3D-QALAS were evaluated by comparing those obtained with and without CS.

To compare the quantitative values of the plaques and normal-appearing white matter (NAWM) of MS patients obtained with and without CS, VOI analysis was performed. A neuroradiologist (S.F.) identified plaques that were larger than 5 mm in diameter using all the available images. A spherical VOI with 4-mm diameter was placed on each plaque and contralateral NAWM to measure the mean T1, T2, PD, and MVF values (see Supplemental Digital Content Figure 2, http://links.lww.com/RLI/A587, an example of spherical VOI placement in a patient with MS).

In Vivo Qualitative Assessment

To evaluate the effects of CS on image quality, all patient images were blinded and independently assessed by 2 neuroradiologists (C.A. and S.K.) with 10 and 6 years of experience, respectively. The evaluation was performed with at least 4 weeks of washout period between reading sessions to minimize the recall bias. The images were presented in a random order in 3 sessions during which each reader was presented only once with each case per session from one of the following 3 datasets: 3D-QALAS with CS, 3D-QALAS without CS, and conventional contrast-weighted image dataset. For 3D-QALAS datasets, the following contrast-weighted images were generated using SyMRI software: T1WI, T1-weighted images; T2WI, T2-weighted images; FLAIR, fluid-attenuated inversion recovery images; DIR, double-inversion recovery images; and PSIR, phase-sensitive inversion recovery images. TR, TE, and TI used for image synthesis were virtually set as follows: T1WI, 650/10/− milliseconds; T2WI, 4500/100/− milliseconds; FLAIR, 15,000/75/3000 milliseconds; DIR, 15,000/100/3600 milliseconds; and PSIR, 6000/10/500 milliseconds, respectively. The conventional contrast-weighted image dataset consisted only of T1WI, T2WI, and FLAIR images.

For each contrast-weighted view, the overall image quality and visibility of brain structures (how easily the margins and structures of an anatomic region can be detected) were rated on a 5-point Likert scale, which was defined as follows: 1, unacceptable; 2, poor; 3, acceptable; 4, good; and 5, excellent. The structures included the central sulcus, head of the caudate nucleus, posterior limb of the internal capsule, cerebral peduncle, and middle cerebellar peduncle.[39] Conspicuity of plaques was also rated by using the same 5-point Likert scale. Further, readers recorded whether any of the following artifacts were present in each image: truncation and ringing artifacts, motion artifacts, aliasing artifacts, chemical shift artifacts, and any other artifacts (eg, spike noise, banding, and blurring).[40] Readers were provided with a free text column to record any other observations.

Statistical Analysis

All statistical analyses were performed on R program version 3.5.1 (R Core Team [2018], R).[41] Simple linear regression analyses were performed for each quantitative metric obtained from the datasets with and without CS. A Bland-Altman analysis was performed to assess the agreement and biases between the metrics derived from 3D-QALAS with and without CS. Agreement of categorical data between readers was assessed using Kendall's coefficient of concordance. The overall image quality and structural delineations for each contrast-weighted image were compared among 3D-QALAS with and without CS and conventional images using the pairwise Dunn-Bonferroni post hoc test when there were significant differences in the Friedman test. Agreement of overall image quality between 3D-QALAS with and without CS was assessed using Kendall's coefficient of concordance. A P value of less than 0.05 was considered statistically significant.

RESULTS

Phantom Study

The temperature of the phantom immediately after the scan was 19.6°C ± 0.4°C. The T1, T2, and PD values that were measured using the data acquired with CS showed strong linear associations with the values acquired without CS (R^2 = 0.999, 0.993, and 0.996, respectively; see Supplemental Digital Content Figure 3, http://links.lww.com/RLI/A587: Scatterplots and Bland-Altman plots comparing T1, T2, and PD values). The linear fits had slopes of 0.99 for T1, 0.90 for T2, and 1.0 for PD, and the intercepts were 8.3 milliseconds for T1, 15.2 milliseconds for T2, and −0.1% for PD. The mean biases for T1, T2, and PD were −3.3 milliseconds, 9.6 milliseconds, and −0.3%, respectively. The 95% agreement limits for T1, T2, and PD were −30.0 milliseconds to 23.5 milliseconds, −114.5 milliseconds to 133 milliseconds, and −2.5% to 1.9%, respectively.

In Vivo Quantitative Assessment

Figure 1 shows representative T1, T2, and PD maps and tissue fraction maps of the brain obtained from a healthy volunteer using 3D-QALAS with and without CS. The relative difference of T1, T2, and PD values obtained with and without CS are shown in Figure 2. The difference was very small on the brain parenchyma, whereas T2 values on the brain surface tended to be smaller when using CS. Representative quantitative maps, tissue fraction maps, and contrast-weighted images of an MS patient created from data acquired by 3D-QALAS with CS are shown in Figure 3. Figure 4 summarizes the agreement of the T1, T2, PD, and MVF values between the data acquired with

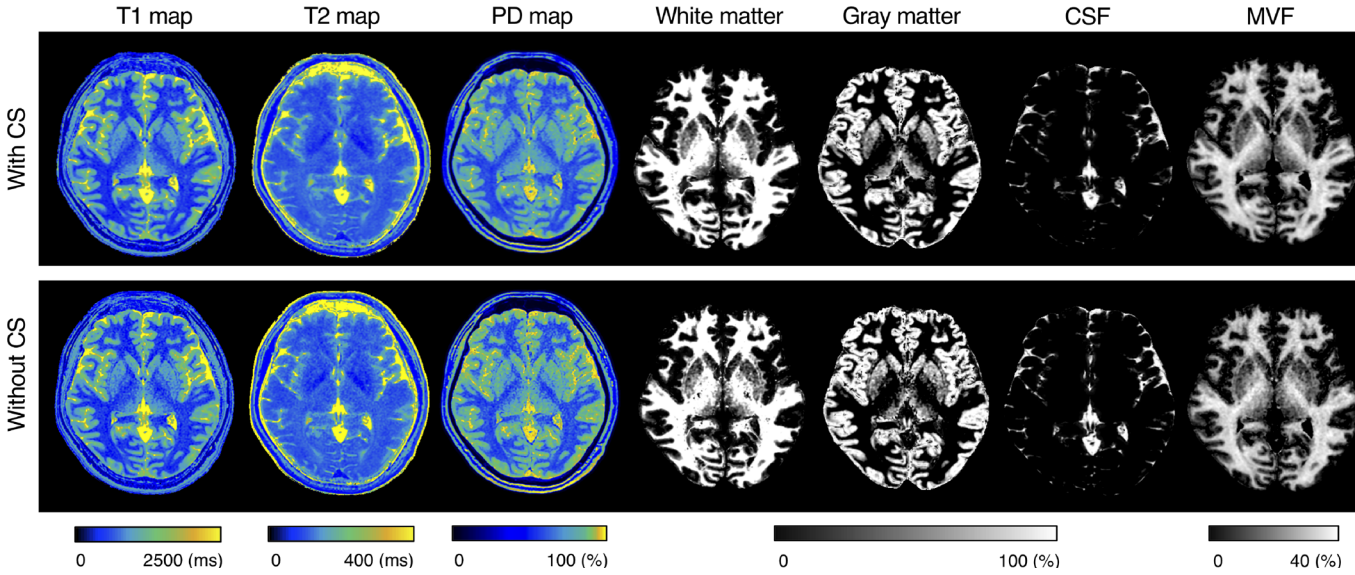

FIGURE 1. Representative quantification maps and tissue fraction maps of a healthy volunteer. Axial images of T1, T2, and PD maps, and segmentation results for white matter, gray matter, cerebrospinal fluid, and myelin volume fraction. Minimal differences are observed between the maps obtained with and without CS. PD, proton density; CSF, cerebrospinal fluid; MVF, myelin volume fraction; CS, compressed sensing.

and without CS in different brain regions. The linearity of measurements in T1, T2, PD, and MVF values obtained with and without CS were very strong (R^2 = 0.990–0.998). The T1, T2, and PD values of the CSF with CS were 4216 ± 45.6 milliseconds, 1997 ± 7.3 milliseconds, and 101% ± 3.2%, respectively, whereas the mean T1, T2, and PD without CS were 4181 ± 36.0 milliseconds, 1998 ± 3.9 milliseconds, and 98.2 ± 2.9, respectively. Figure 5 shows the agreement of the tissue fraction volumes that were calculated using 3D-QALAS with and without CS. The tissue segmentation obtained with and without CS also showed a high linearity (R^2 = 0.987–0.999).

A total of 140 plaques were analyzed in 12 patients with MS. Supplemental Digital Content Figure 4, http://links.lww.com/RLI/A587 shows 3D scatterplots comparing the quantitative properties of the plaques and NAWM; a clear differentiation of the plaques and NAWM using quantitative values was observed regardless of the application of CS. Figure 6 shows the linearity and biases of T1, T2, and PD values of the plaques evaluated from the images obtained with and without CS. The quantitative tissue values of the plaques and NAWM obtained with CS showed a high linearity with those obtained without CS (R^2 = 0.967–1.000).

In Vivo Qualitative Assessment

Representative examples of synthetic contrast-weighted images of 3D-QALAS with and without CS are presented in Figure 7. Another representative case of MS is presented in Supplemental Digital Content Figure 5, http://links.lww.com/RLI/A587 (a representative example of a patient with MS shown in reformatted sagittal views). Because the interrater agreement between the 2 readers was high, with Kendall's coefficient of concordance of 0.82, the pooled overall image quality and structural delineation, that is, the results of the 2 readers, were simultaneously used for further analysis. Figure 8 shows the overall image quality and structural delineation of contrast-weighted images scored on a 5-point Likert scale. On Friedman test, there was no significant difference in the overall image quality of T1WI among the examined

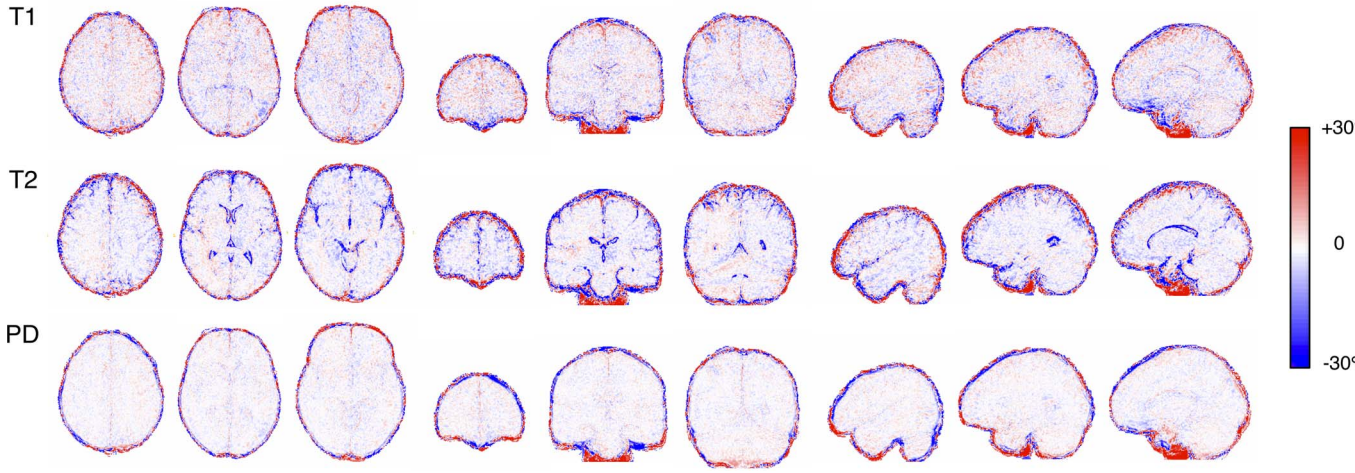

FIGURE 2. Images show relative differences in T1, T2, and PD values between with and without CS. Maps were calculated by subtraction (quantitative values acquired with CS minus those without) divided by their mean on a group level. Different metrics (rows) and sections (columns) are shown. Red and blue indicates larger and smaller value with CS than without, respectively.

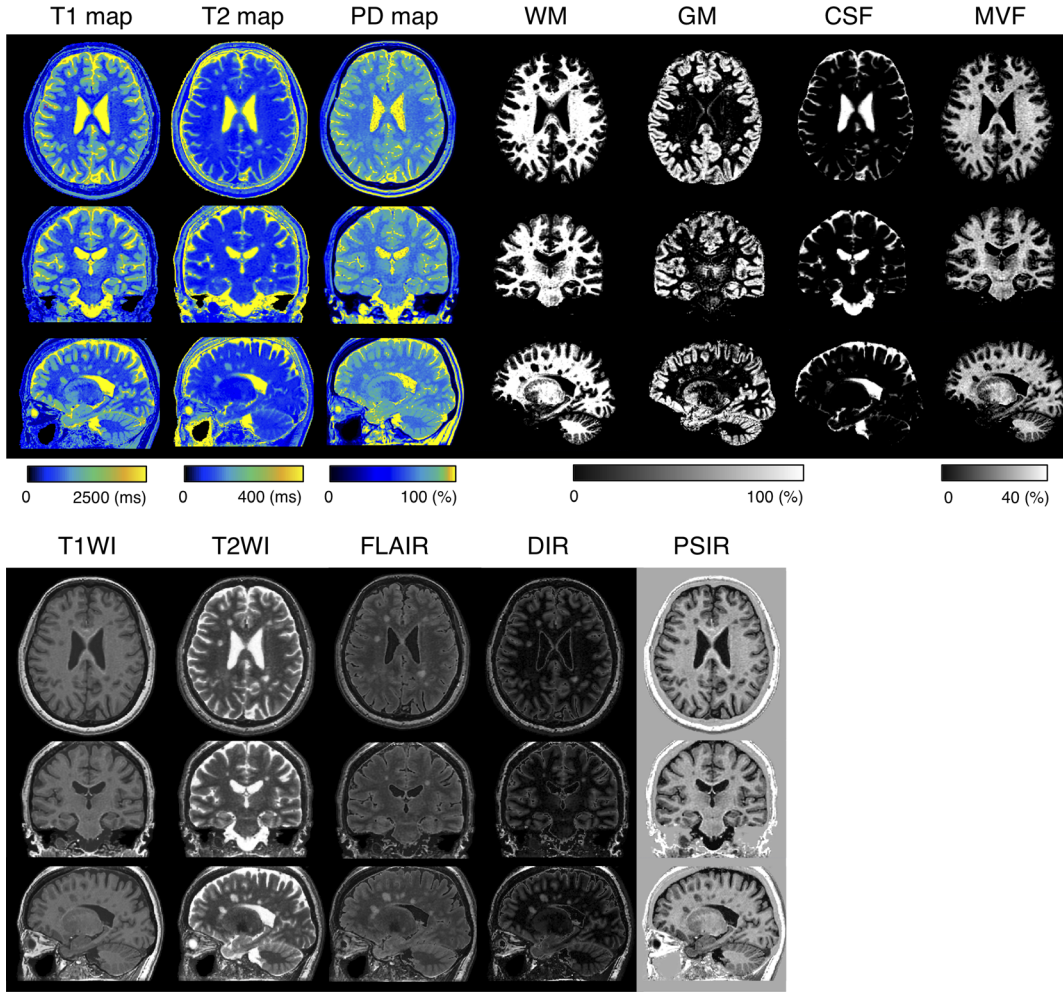

FIGURE 3. Representative quantitative maps, tissue fraction maps, and contrast-weighted images of a multiple sclerosis patient created from data acquired by 3D-QALAS with CS. All images are reformatted in 3 directions. Note that all of these maps are acquired in a single scan. WM, white matter; GM, gray matter; CSF, cerebrospinal fluid; MVF, myelin volume fraction; T1WI, T1-weighted images; T2WI, T2-weighted images; FLAIR, fluid-attenuated inversion recovery images; DIR, double-inversion recovery images; and PSIR, phase-sensitive inversion recovery images.

datasets (ie, 3D-QALAS with CS, 3D-QALAS without CS, and conventional contrast-weighted images) ($P = 0.17$). Pairwise Dunn-Bonferroni post hoc test revealed that the overall image quality of the synthetic images acquired with T2WI and FLAIR sequences, with and without CS, was significantly lower than that of the conventional images ($P < 0.001$). No significant differences were present between the synthetic images with and without CS for all contrast weightings (P values for T2WI, FLAIR, DIR, and PSIR were 0.53, 0.98, 0.99, and 0.99, respectively). Overall image quality between 3D-QALAS with and without CS across all contrast-weighted images showed high agreement with Kendall's coefficient of concordance of 0.83. Among the target structures examined, there were no significant differences between contrast-weighted images acquired with and without CS for all contrast weightings.

Truncation artifacts were seen in 4.2% (3/72) of the conventional contrast-weighted images, 5% (3/60) of 3D-QALAS–acquired images with CS, and 3.3% (2/60) of 3D-QALAS–acquired images without CS. Parenchymal-CSF interface hyperintensities[39,42,43] were found in 8.3% (5/60) of the 3D-QALAS–acquired images with CS and without CS (8.3%; 5/60). None of the images exhibited a global ringing artifact, which is known to be associated with CS.[44] No artifacts were noted in conventional contrast-weighted images.

DISCUSSION

The long acquisition times of quantitative MRI have made the procedure suboptimal for routine clinical practice. Although faster imaging is desirable, assuring reproducible quantitative values and sufficient image quality is a prerequisite for utilization in clinical settings.[45] Hence, to address both these issues and evaluate the performance of quantitative MRI, we have implemented CS acceleration for high spatial resolution multiparametric imaging by 3D-QALAS; we also assessed the quantitative values and tissue segmentation performance with and without CS acceleration. The accelerated acquisition protocol of 3D-QALAS with CS enabled isotropic, 1-mm, multiparametric imaging of the whole brain in less than 6 minutes, while maintaining the tissue quantitative values and segmentation quality. This technology can alleviate the problem of long MRI scanning times and provide objective information of the brain to supplement the contrast-weighted imaging commonly used in clinical settings.

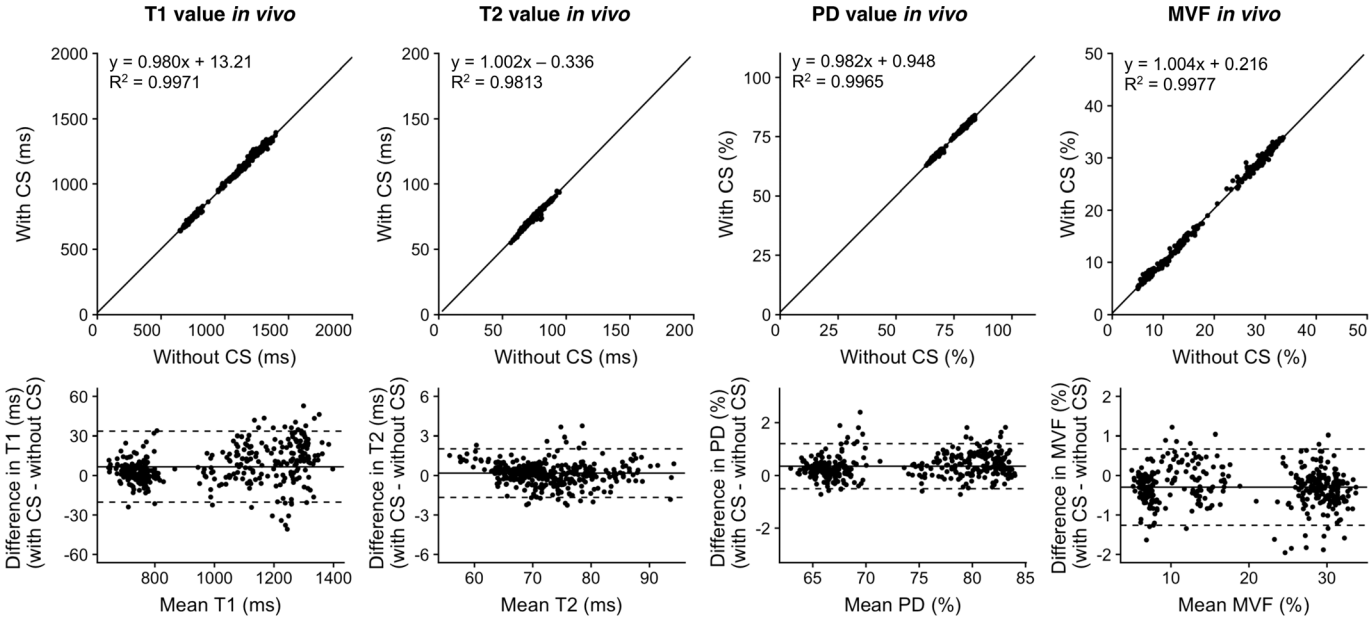

FIGURE 4. Scatterplots and Bland-Altman plots comparing T1, T2, PD, and MVF values of 16 brain regions of 10 volunteers and 12 patients with MS, which were calculated from 3D-QALAS with CS compared with those calculated without CS. Solid black lines in the scatterplots represent the linear regression fit, and the center solid lines in the Bland-Altman plots represent mean differences. The upper and lower dotted lines represent the agreement limit, which was defined as the mean difference ± 1.96 × SD of the difference between the values acquired with and without CS. SD, standard deviation. PD, proton density; MVF, myelin volume fraction.

The relaxometry parameters and tissue volumes obtained with 3D-QALAS with and without CS showed a high agreement with both in vitro and in vivo settings. The bias caused by the presence or absence of CS was estimated to be approximately 0.99% (mean difference of 9.9 milliseconds divided by 1000 milliseconds), 0.24% (mean difference of 0.19 milliseconds divided by 80 milliseconds), 0.49% (mean difference of 0.34% divided by 70%), and −1.7% (mean difference of −0.33% divided by 20%) for T1, T2, PD, and MVF, respectively, which is sufficiently small. The robustness of the quantitative value could be attributed to the fact that the center of the k-space, which dominates the contrast, was fully sampled. Acceleration with CS was effective for high-resolution imaging with 3D-QALAS, partly because the proportion of high-frequency components, which have a high undersampling ratio, increases as the resolution increases. Although only small differences were observed between values obtained with and without CS, the differences in T2 were noticeable on brain surfaces and ventricular walls. This may be due to partial volume effects: the T2 value was forcefully calculated using Bloch equation supposing a monoexponential behavior, but the relaxation behavior in these regions is expected to be multiexponential.

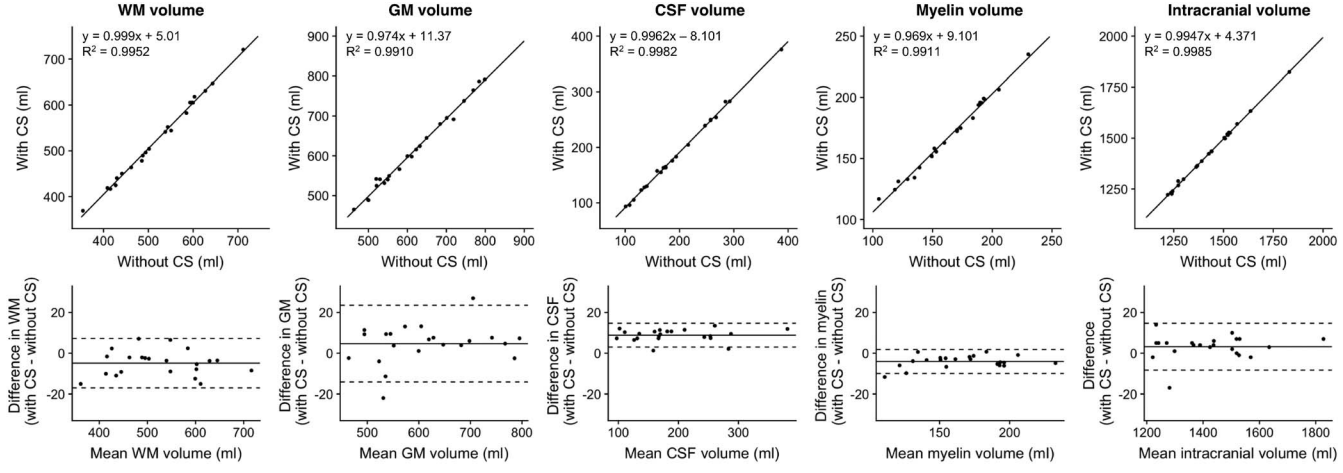

FIGURE 5. Scatterplots and Bland-Altman plots comparing GM, WM, CSF, myelin, and intracranial volumes of 10 volunteers and 12 patients with MS, calculated from 3D-QALAS acquired with and without CS. The center solid lines in the Bland-Altman plots represent mean differences, whereas the upper and lower dotted lines represent the limit of agreement, which is defined as the mean difference ± 1.96 × SD of the difference between the values acquired with and without CS. SD, standard deviation, WM, white matter; GM, gray matter; CSF, cerebrospinal fluid.

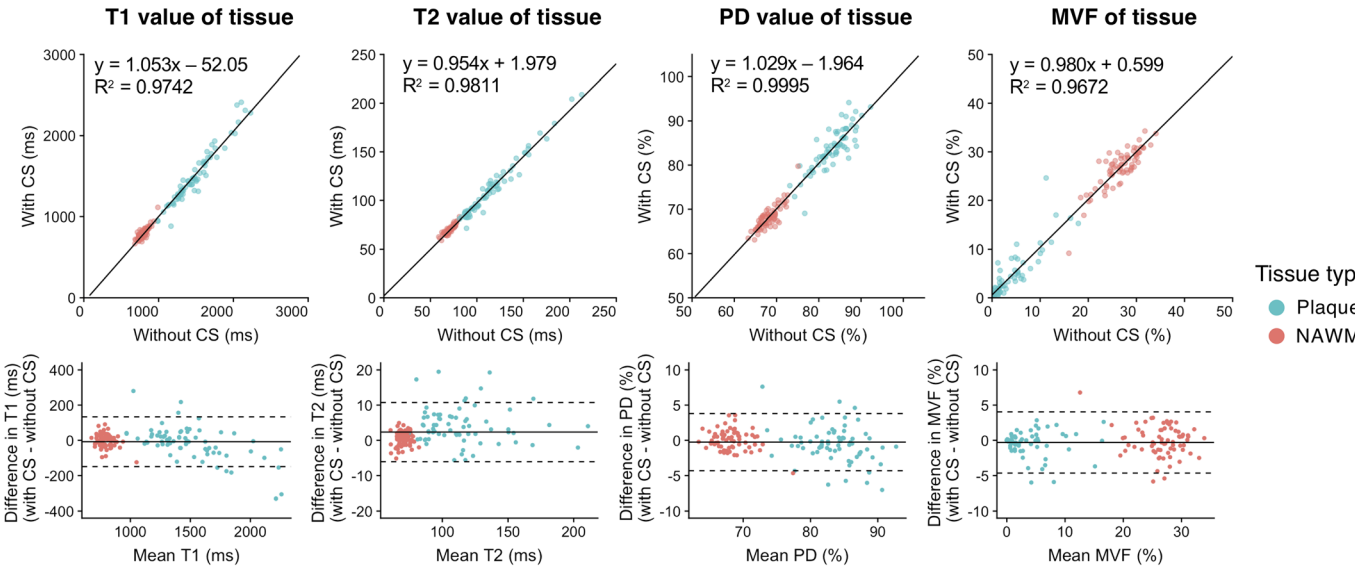

FIGURE 6. Scatterplots and Bland-Altman plots comparing T1, T2, and PD values of plaques and NAWM calculated from 3D-QALAS acquired with and without CS. The solid black lines in the scatterplots represent the linear regression fit, and the center solid lines of the Bland-Altman plots represent mean differences. The dotted lines represent the agreement limit, which was defined as the mean difference ± 1.96 × SD of the difference between the measurements with and without CS. SD, standard deviation; CS, compressed sensing; PD, proton density; MVF, myelin volume fraction; NAWM, normal-appearing white matter.

The overall image quality of contrast-weighted images acquired with 3D-QALAS in patients was maintained with the combination of CS. However, the image quality of the synthetic T2-weighted and FLAIR images, either with and without CS, was inferior than the corresponding conventional images. This difference in image quality has been observed in published literature,[39,42] whereas another study applied deep learning to improve the image quality of synthetic FLAIR images.[43] It may be possible to reduce artifacts by creating synthetic contrast-weighted images directly from the original source images, bypassing the quantitative maps.[46] In the current study, parenchymal-CSF interface hyperintensities were observed in both synthetic FLAIR images with and without CS. Although this artifact did not affect the delineation of MS plaques ($P = 0.33$), it may mimic certain pathologies involving the meninges, such as subarachnoid hemorrhage and meningitis.

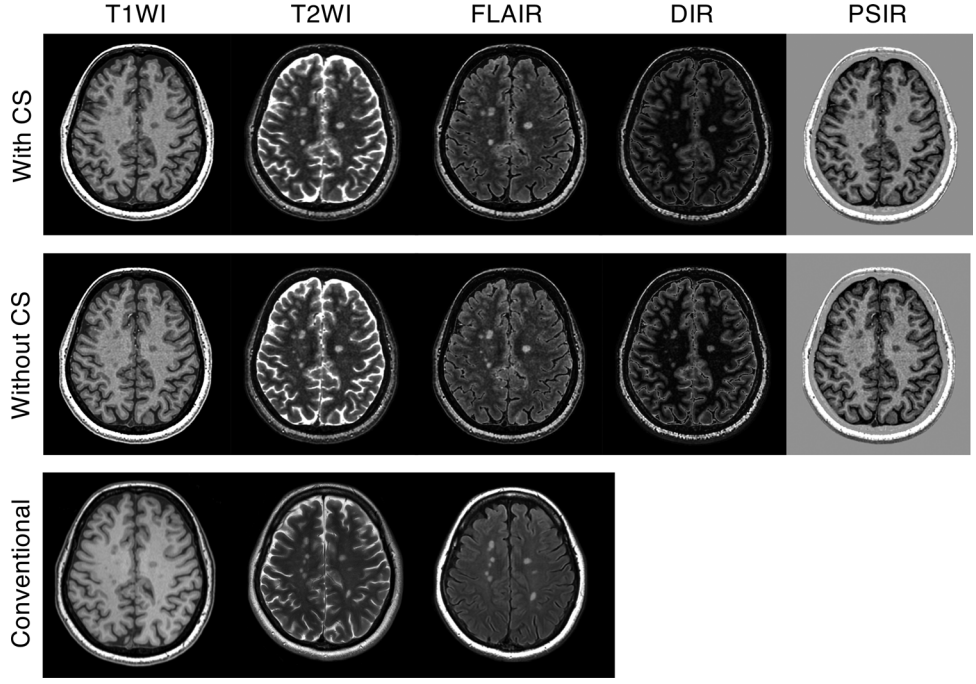

FIGURE 7. Representative contrast-weighted images of a multiple sclerosis patient. Minimal differences are seen between the contrast-weighted images that were obtained with and without CS. CS, compressed sensing; T1WI, T1-weighted images; T2WI, T2-weighted images; FLAIR, fluid-attenuated inversion recovery images; DIR, double-inversion recovery images; and PSIR, phase-sensitive inversion recovery images.

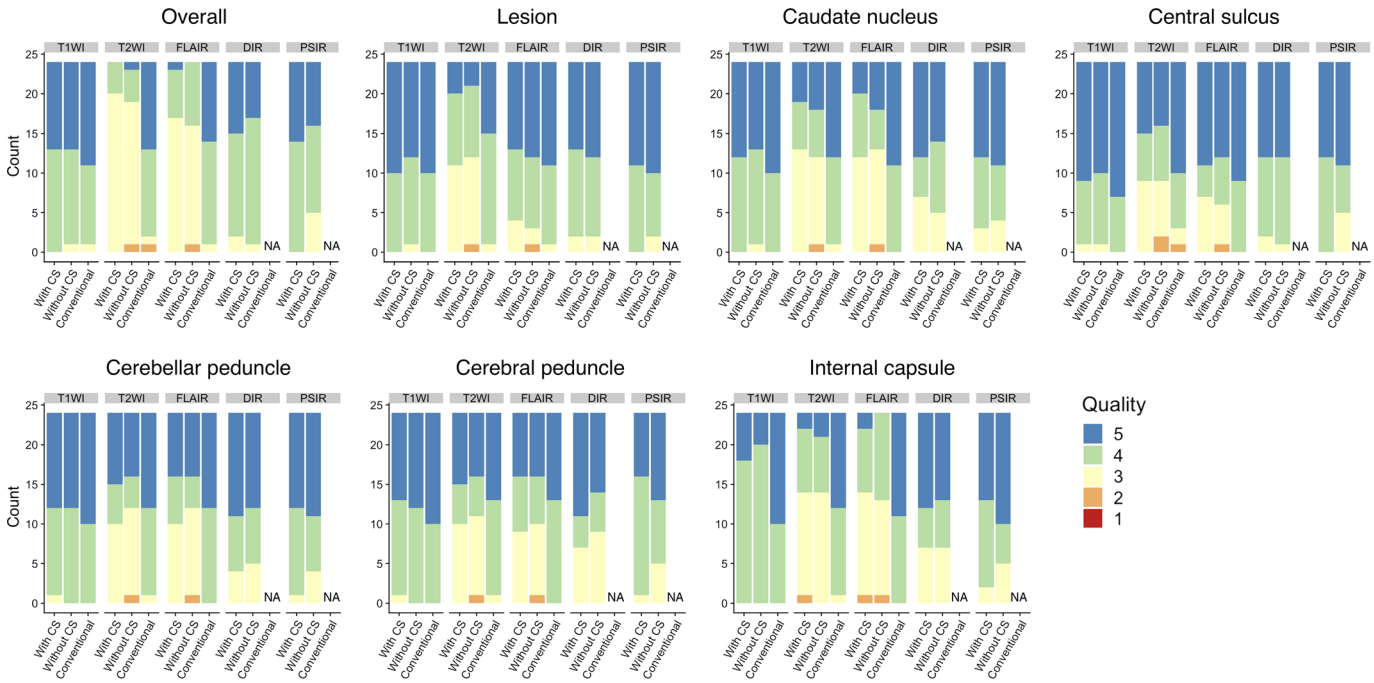

FIGURE 8. Visual assessment of contrast-weighted images generated from 3D-QALAS with and without CS and conventional imaging for patients with multiple sclerosis. Overall image quality and structural delineation scored on a 5-point Likert score by 2 neuroradiologists are shown. T1WI, T1-weighted images; T2WI, T2-weighted images; FLAIR, fluid-attenuated inversion recovery images; DIR, double-inversion recovery images; and PSIR, phase-sensitive inversion recovery images; NA, not applicable.

Although this artifact was readily recognizable by its distinctive appearance and by confirming the lack of such artifact on other contrast-weighted images, additional imaging of conventional FLAIR may be still desirable. The partial volume effect may explain the reason for lower *P* values when comparing the T2-weighted images obtained with and without CS than other contrast-weighted images. Although there were no indications that the application of CS made lesions less visible in the reading sessions, the appearance may be slightly different for T2WI and should be interpreted with caution.

Scan time reduction with CS may enable the incorporation of high spatial resolution multiparametric imaging in routine clinical settings. The rapid acquisition of relaxometry parameters in 6 minutes is comparable to our routine 3D T1WI structural imaging protocol, which requires 4 to 5 minutes. This approach could be particularly effective for pediatric and preoperative imaging, wherein multiple contrast images are needed in a short time.

Traditionally, visual and quantitative assessments have required independent scans, resulting in very long examination times, making them difficult to use simultaneously in clinical practice. The present study showed that 3D-QALAS combined with CS provides information required for both visual and quantitative assessment. For example, scan times for MS lesions and other lesions would be shorter, allowing for more objective clinical management.

The inherent alignment of the maps is a significant advantage of multiparametric mapping techniques. It has been shown that brain segmentation with synthetic T1WI strongly agrees with image segmentation obtained with conventional 3D T1WI.[19] Reliable morphometry metrics with relaxometry parameters would translate this segmentation to reliable VOI data to detect small differences in local tissues; this will further pave the way for combined evaluation of morphometric and quantitative values.[47] Further, image postprocessing, including deep learning, could be performed without the need for image resampling or registration.[43,48] However, simultaneous acquisition of spin parameter maps could also be problematic because all the maps would be degraded if motion corruption occurs at any point during the acquisition. To mitigate this complication, current developments in motion detection or correction[49] could be incorporated into the 3D-QALAS technique in the future, in addition to the further acceleration of acquisition time.

The generalizability of our study results is subject to certain limitations. For instance, we did not compare CS to a standard PI technique, and we have used a fixed undersampling factor in this study. This was chosen based on a preliminary study with a phantom. Although a study that iterates multiple undersampling factors by small steps to explore the highest undersampling factor with tolerable degradation in quantitative values and image quality would be of tremendous interest from the point of view of engineering, it was not feasible to perform such a study on human subjects. Second, the phantom measurements were not verified by conventional quantitative mapping methods, such as variable flip angle gradient echo scan and Carr-Purcell-Meiboom-Gill sequence. Third, this study only included a single group of patients with MS. Relatively young adults, in whom MS is frequently seen, tend to be cooperative during MRI examinations. The results may not be generalizable to patients with other movement disorders and to older patients who may not be cooperative during MRI examinations. Hence, to mimic actual clinical scenarios, inclusion and evaluation of patients with movement disorders and elderly patients may further demonstrate the effectiveness of applying CS to 3D-QALAS.

In conclusion, isotropic 1-mm multiparametric imaging of the whole brain based on 3D-QALAS can be performed in less than 6 minutes using CS, while preserving tissue quantitative values, tissue

segmentation, and contrast-weighted image quality. The image quality of T2WI and FLAIR was inferior to that of conventional contrast-weighted images, and additional conventional imaging may be selected. This technique would further facilitate the use of quantitative imaging in actual clinical settings.

ACKNOWLEDGMENTS

The authors acknowledge Takuya Haruyama and Yuma Nishimura who were helpful with data handling.

REFERENCES

1. Tofts P. *Quantitative MRI of the Brain: Measuring Changes Caused by Disease*. Chichester, West Sussex; Hoboken, NJ: Wiley; 2003.
2. Warntjes JB, Leinhard OD, West J, et al. Rapid magnetic resonance quantification on the brain: optimization for clinical usage. *Magn Reson Med*. 2008;60:320–329.
3. Hagiwara A, Warntjes M, Hori M, et al. SyMRI of the brain: rapid quantification of relaxation rates and proton density, with synthetic MRI, automatic brain segmentation, and myelin measurement. *Invest Radiol*. 2017;52:647–657.
4. Ma D, Gulani V, Seiberlich N, et al. Magnetic resonance fingerprinting. *Nature*. 2013;495:187–192.
5. Blystad I, Warntjes JBM, Smedby O, et al. Quantitative MRI for analysis of peritumoral edema in malignant gliomas. *PLoS One*. 2017;12:e0177135.
6. Lee SM, Choi YH, You SK, et al. Age-related changes in tissue value properties in children: simultaneous quantification of relaxation times and proton density using synthetic magnetic resonance imaging. *Invest Radiol*. 2018;53:236–245.
7. Hagiwara A, Hori M, Yokoyama K, et al. Utility of a multiparametric quantitative MRI model that assesses myelin and edema for evaluating plaques, periplaque white matter, and normal-appearing white matter in patients with multiple sclerosis: a feasibility study. *AJNR Am J Neuroradiol*. 2017;38:237–242.
8. Badve C, Yu A, Dastmalchian S, et al. MR fingerprinting of adult brain tumors: initial experience. *AJNR Am J Neuroradiol*. 2017;38:492–499.
9. Fujita S, Nakazawa M, Hagiwara A, et al. Estimation of gadolinium-based contrast agent concentration using quantitative synthetic MRI and its application to brain metastases: a feasibility study. *Magn Reson Med Sci*. 2019;18:260–264.
10. Warntjes M, Engström M, Tisell A, et al. Modeling the presence of myelin and edema in the brain based on multi-parametric quantitative MRI. *Front Neurol*. 2016;7:16.
11. Chen Y, Chen MH, Baluyot KR, et al. MR fingerprinting enables quantitative measures of brain tissue relaxation times and myelin water fraction in the first five years of life. *Neuroimage*. 2019;186:782–793.
12. Warntjes JBM, Persson A, Berge J, et al. Myelin detection using rapid quantitative MR imaging correlated to macroscopically registered luxol fast blue-stained brain specimens. *AJNR Am J Neuroradiol*. 2017;38:1096–1102.
13. Ouellette R, Mangeat G, Polyak I, et al. Validation of rapid magnetic resonance myelin imaging in multiple sclerosis. *Ann Neurol*. 2020;87:710–724.
14. Saccenti L, Hagiwara A, Andica C, et al. Myelin measurement using quantitative magnetic resonance imaging: a correlation study comparing various imaging techniques in patients with multiple sclerosis. *Cell*. 2020;9:393.
15. Hagiwara A, Hori M, Kamagata K, et al. Myelin measurement: comparison between simultaneous tissue relaxometry, magnetization transfer saturation index, and T1w/T2w ratio methods. *Sci Rep*. 2018;8:10554.
16. Andica C, Hagiwara A, Hori M, et al. Aberrant myelination in patients with Sturge-Weber syndrome analyzed using synthetic quantitative magnetic resonance imaging. *Neuroradiology*. 2019;61:1055–1066.
17. Hagiwara A, Kamagata K, Shimoji K, et al. White matter abnormalities in multiple sclerosis evaluated by quantitative synthetic MRI, diffusion tensor imaging, and neurite orientation dispersion and density imaging. *AJNR Am J Neuroradiol*. 2019;40:1642–1648.
18. Hwang KP, Banerjee S, Zhang T, et al. 3D isotropic multi-parameter mapping and synthetic imaging of the brain with 3D-QALAS: comparison with 2D MAGIC. *In Proceedings of the 27th Annual Meeting of ISMRM*. Montréal, Canada; 2019:5759.
19. Fujita S, Hagiwara A, Hori M, et al. 3D quantitative synthetic MRI-derived cortical thickness and subcortical brain volumes: scan-rescan repeatability and comparison with conventional T_1 -weighted images. *J Magn Reson Imaging*. 2019; 50:1834–1842.
20. Fujita S, Hagiwara A, Hori M, et al. Three-dimensional high-resolution simultaneous quantitative mapping of the whole brain with 3D-QALAS: an accuracy and repeatability study. *Magn Reson Imaging*. 2019;63:235–243.
21. Lustig M, Donoho D, Pauly JM. Sparse MRI: the application of compressed sensing for rapid MR imaging. *Magn Reson Med*. 2007;58:1182–1195.
22. Sagawa H, Kataoka M, Kanao S, et al. Impact of the number of iterations in compressed sensing reconstruction on ultrafast dynamic contrast-enhanced breast MR imaging. *Magn Reson Med Sci*. 2019;18:200–207.
23. Kijowski R, Rosas H, Samsonov A, et al. Knee imaging: rapid three-dimensional fast spin-echo using compressed sensing. *J Magn Reson Imaging*. 2017;45:1712–1722.
24. Seo N, Park MS, Han K, et al. Feasibility of 3D navigator-triggered magnetic resonance cholangiopancreatography with combined parallel imaging and compressed sensing reconstruction at 3T. *J Magn Reson Imaging*. 2017;46:1289–1297.
25. Fushimi Y, Fujimoto K, Okada T, et al. Compressed sensing 3-dimensional time-of-flight magnetic resonance angiography for cerebral aneurysms: optimization and evaluation. *Invest Radiol*. 2016;51:228–235.
26. Okuchi S, Fushimi Y, Okada T, et al. Visualization of carotid vessel wall and atherosclerotic plaque: T1-SPACE vs. compressed sensing T1-SPACE. *Eur Radiol*. 2019;29:4114–4122.
27. Fushimi Y, Okada T, Kikuchi T, et al. Clinical evaluation of time-of-flight MR angiography with sparse undersampling and iterative reconstruction for cerebral aneurysms. *NMR Biomed*. 2017;30.
28. Koolstra K, Beenakker JM, Koken P, et al. Cartesian MR fingerprinting in the eye at 7T using compressed sensing and matrix completion-based reconstructions. *Magn Reson Med*. 2019;81:2551–2565.
29. Mazor G, Weizman L, Tal A, et al. Low-rank magnetic resonance fingerprinting. *Med Phys*. 2018. doi:10.1002/mp.13078.
30. Doneva M, Bornert P, Eggers H, et al. Compressed sensing reconstruction for magnetic resonance parameter mapping. *Magn Reson Med*. 2010;64:1114–1120.
31. King K, Xu D, Brau AC, et al. Compressed sensing description: "a new combination of compressed sensing and data driven parallel imaging". *In: Proceedings of the 19th Annual Meeting of ISMRM*. Stockholm, Sweden; 2010:4881.
32. Takei N, Hagiwara A, Fujita S, et al. Compressed sensing 3D multi-parametric imaging toward isotropic 1mm^3 imaging. *In: Proceedings of the 27th Annual Meeting of ISMRM*. Montréal, Canada; 2019:2981.
33. Brau AC, Beatty PJ, Skare S, et al. Comparison of reconstruction accuracy and efficiency among autocalibrating data-driven parallel imaging methods. *Magn Reson Med*. 2008;59:382–395.
34. Keenan KE, Stupic KF, Boss MA, et al. Multi-site, multi-vendor comparison of T1 measurement using ISMRM/NIST system phantom. *In: Proceedings of the 24th Annual Meeting of ISMRM*. Singapore; 2016:3290.
35. Thompson AJ, Banwell BL, Barkhof F, et al. Diagnosis of multiple sclerosis: 2017 revisions of the McDonald criteria. *Lancet Neurol*. 2018;17:162–173.
36. Hagiwara A, Hori M, Cohen-Adad J, et al. Linearity, bias, intrascanner repeatability, and interscanner reproducibility of quantitative multidynamic multiecho sequence for rapid simultaneous relaxometry at 3 T: a validation study with a standardized phantom and healthy controls. *Invest Radiol*. 2019;54:39–47.
37. Jenkinson M, Beckmann CF, Behrens TE, et al. FSL. *Neuroimage*. 2012;62:782–790.
38. West J, Warntjes JB, Lundberg P. Novel whole brain segmentation and volume estimation using quantitative MRI. *Eur Radiol*. 2012;22:998–1007.
39. Tanenbaum LN, Tsiouris AJ, Johnson AN, et al. Synthetic MRI for clinical neuroimaging: results of the magnetic resonance image compilation (MAGiC) prospective, multicenter, multireader trial. *AJNR Am J Neuroradiol*. 2017;38:1103–1110.
40. Krupa K, Bekiesinska-Figatowska M. Artifacts in magnetic resonance imaging. *Pol J Radiol*. 2015;80:93–106.
41. R Core Team. *R: A Language and Environment for Statistical Computing [computer program]. Version 3.5.1*. Vienna, Austria: R Foundation for Statistical Computing; 2018. Available at: https://www.R-project.org/. Accessed July 2, 2020.
42. Lee SM, Choi YH, Cheon JE, et al. Image quality at synthetic brain magnetic resonance imaging in children. *Pediatr Radiol*. 2017;47:1638–1647.
43. Hagiwara A, Otsuka Y, Hori M, et al. Improving the quality of synthetic flair images with deep learning using a conditional generative adversarial network for pixel-by-pixel image translation. *AJNR Am J Neuroradiol*. 2019;40:224–230.
44. Sharma SD, Fong CL, Tzung BS, et al. Clinical image quality assessment of accelerated magnetic resonance neuroimaging using compressed sensing. *Invest Radiol*. 2013;48:638–645.
45. Hagiwara A, Fujita S, Ohno Y, et al. Variability and standardization of quantitative imaging: monoparametric to multiparametric quantification, radiomics, and artificial intelligence. *Invest Radiol*. 2020;55:601–616.
46. Wang K, Doneva M, Amthor T, et al. High fidelity direct-contrast synthesis from magnetic resonance fingerprinting in diagnostic imaging. *In Proceedings of the 28th Annual Meeting of ISMRM*. Sydney, Australia; 2020:867.
47. Damulina A, Pirpamer L, Soellradl M, et al. Cross-sectional and longitudinal assessment of brain iron level in Alzheimer disease using 3-T MRI. *Radiology*. 2020;296:619–626.
48. Fujita S, Hagiwara A, Otsuka Y, et al. Deep learning approach for generating MRA images from 3D quantitative synthetic MRI without additional scans. *Invest Radiol*. 2020;55:249–256.
49. Takei N, Shin D, Rettman D, et al. Prospective motion corrected 3D multi-parametric imaging. *In Proceedings of the 28th Annual Meeting of ISMRM*. Sydney, Australia; 2020:880.

特集2

最新版 MRIのリスクマネージメント

—安全なMRI検査のために求められる対策—

企画協力：宮地　利明
金沢大学保健学類長

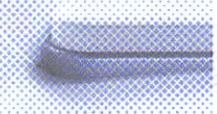

強力な磁場が発生するMRIは，十分な安全を確保した上で検査を施行することが肝要です。特に，近年は植込み型医療機器のMRI検査への対応が進み，検査の適応を広げている一方で，安全管理の複雑化にもつながっています。また，新型コロナウイルス感染症（COVID-19）がまん延する中，感染症対策も重要になっています。加えて，2021年は東日本大震災から10年という節目の年であり，改めて自然災害への対策も問われています。そこで，特集2では，MRI検査におけるリスクマネージメントの最新動向に焦点を当てます。

1. 臨床MRI安全運用のための指針について

平井　俊範　熊本大学大学院生命科学研究部放射線診断学講座

本邦におけるMRI機器の台数は世界平均の約7倍であり，人口に対するMRI機器の比率は世界で最も高い。MRIは大きな静磁場および変化する磁場，高出力無線周波数コイルシステム，および外因性造影剤に関連する安全性リスクがある。画像診断医は，患者，コ・メディカルをMRI検査に伴う危害から守るために，これらのリスクとその低減に注意を払い，安全基準を厳密に順守する必要がある。

日本磁気共鳴医学会（JSMRM）の安全性評価委員会は，2014年に『MRI安全性の考え方』の第2版を発行しているが[1]，本邦のMRI施設において安全管理基準がどの程度順守されているかは不明であった。そこで，厚生労働行政推進調査事業費（地域医療基盤開発推進研究事業）にて，実臨床におけるMRI検査の安全管理の現状を調査することとなった。その結果，本邦におけるMRI検査の安全管理体制は，全体的に不十分である実態が明らかとなった[2]。

この結果を踏まえ，日本磁気共鳴医学会と日本医学放射線学会は，日本放射線技術学会，および日本磁気共鳴専門技術者認定機構の協力の下に，「臨床MRI安全運用のための指針」を設定した。

本稿では，MRI安全運用に関する全国多施設調査の結果と，それを踏まえた指針を紹介する。

MRI安全運用に関する全国多施設調査

MRI安全運用に関する全国多施設調査には，MRI安全管理に関する項目（管理体制・マニュアル整備，検査依頼時の確認，検査前の確認，検査中の体制，点検・記録）と，メジャーインシデントおよびマイナーインシデントの発生に関する質問のほか，MRI機器を保有している施設の種類，MRI機器，1回の

〈0913-8919/21/￥300/ 論文 /JCOPY〉

表1　MRI検査関連のメジャーインシデント（90施設の102症例）

内　訳	症例数（%）
造影剤投与によるショックや死亡	31（30）
入れ墨，アートメイクなどによる火傷	11（11）
体内植込み型医療機器（ペースメーカなど）の故障	10（10）
体外装具（パワーアンクルなど）による組織損傷	3（3）
その他	47（46）

表2　MRI検査関連のマイナーインシデント（519施設の850症例）

内　訳	症例数（%）
体内磁性体の見逃し	242（28）
体外装具（パワーアンクルなど）の見逃し	146（17）
体内植込み型医療機器（ペースメーカなど）の見逃し	127（15）
造影剤投与に関するもの	96（11）
入れ墨，アートメイクなどの見逃し	22（3）
その他	217（26）

MRI検査の平均時間，MRI検査の数，および人員に関する情報も含まれていた。

この調査票を送った5914の医療施設のうち，2015（34%）施設が質問に完全または部分的に回答した。本調査に参加した施設のタイプは，多い順に200床未満の総合病院（35%），特定機能病院および地域医療支援病院（23%），200床以上の総合病院（20%）などであった。参加施設のMRI機器の内訳は，66%は1.5T装置，23%は3T装置，10%は1.5T未満の装置で，1回のMRI検査の平均時間は，49%の施設では30分，33%の施設は20分であった。2018年9月の1か月間に，2015施設のうち28%が最大100件のMRI検査を行い，22%が100～200件，15%が200～300件，残りの34%の施設が300件を超えるMRI検査を実施した。本調査に参加した施設の73%でMRI専門技術者の雇用がなかった。MRI検査業務（プロトコール指示，立ち会い，読影などのいずれか）に携わる常勤の放射線診断専門医がいるのは57%の施設であった。

管理体制・マニュアル整備に関しては，2009施設が回答した。病院内にMRI管理チームがあったのは13%の施設で，また，少なくとも年に1回のMRI検査管理チームの会合を開催したのは9%の施設のみであった。72%の施設で，MRI検査前における安全管理の体制のマニュアルを作成していた。一方，緊急事態発生時に患者と職員の安全を確保するためのスタッフへのトレーニングは，50%の施設で行われていなかった。さまざまな状況に対処するためのマニュアルの保持は，施設によって異なっていた。閉所恐怖症患者の鎮静のためのマニュアルを保持している施設は298施設で，鎮静された小児患者の管理マニュアルの保持は201施設であった。ガドリニウム造影剤およびガドリニウム造影剤以外のMRI検査時に使用する薬剤（リゾビスト，ブスコパン，グルカゴン，ボースデル）に対する市販後安全対策として，薬剤部門と協力し，使用改訂などに関する重要な情報を院内で周知しているのは，2009施設中のそれぞれ46%および37%であった。

MRI検査前の確認に関しては，2006施設の回答があり，83%の施設において医師が検査を依頼する際に，禁忌体内デバイスの有無を確認するシステムを有していた。安全管理のために必要な情報（体内金属の危険性など），経皮パッチ類（使い捨てカイロ，吸湿発熱ウエア・保温性下着を含む）の有無，検査中止の意思を伝える方法（緊急コールの利用法），造影MRI検査前には腎機能やアレルギー（造影剤過敏症や気管支喘息など）の有無，腎性全身性線維症（NSF）防止の対策（腎機能確認，eGFRの制限，造影剤投与量の順守など）の説明や確認は，多くの施設（79～99%）で施行されていた。MRI検査前に，安全管理のために問診票で，体内植込み型医療機器，体内磁性体，入れ墨，手術の既往歴，体外装具（パワーアンクルなど），アートメイクについて，多くの施設で確認していた。体内磁性体の有無を検査前に，医師以外の問診で確認している施設が90%であった。

検査中の体制に関しては，2004施設の回答があり，70%の施設がMRI検査中に心拍数と血中酸素レベルを監視していた。また，騒音低減対策は，85%の施設で実施されていた。MRI機器や検査室の点検や記録に関する質問に対して，約33%の施設が，MRI室の温度，湿度，酸素濃度，およびコンピュータ室内の温度と湿度の記録を保持していた。MRI装置の品質管理のためのファントムについては，2005施設が回答し，83%が保有していた。MRI装置の始業時のファントムスキャンについては，本調査に回答した2015施設のうち58%が画像アーチファクトを評価していた。

MRI検査関連のインシデントの概要を表1，2に示す。2017年10月～2018年9月の期間中に回答があった1954施設のうち5%の施設で患者の健康に影響を与えたMRI関連のメジャーインシデントがあり，27%の施設でマイナーインシデントが見られた。5%の施設で報告された102症例のメジャーインシデントのうち，31症例（30%）は造影剤投与によるショックまたは死亡であった。27%の施設で850症例のマイナーインシデントが発生した。そのうち，242症例（28%）は体内磁性体の見逃しであった。

MRI検査関連のメジャーインシデントと強く関連する質問項目は，影響が大きい順に，1か月間の延べMRI検査件数，MRI検査時に使用する薬剤の重要な情報に対する院内周知に関する質問，条件付き体内植込み型医療機器（ペースメーカなど）の運用マニュアル整備に関する質問，一歩間違えば起こりうる事故（ヒヤリハット）に関する質問，体内磁性体の有無に対する検査前確認に関する質問，および保守点検（メーカー点検，あるいはメーカー以外の資格者による点検）の定期的施行に関する質問であった。1か月間の延べMRI検査件数と部分的依存性（メジャーインシデントのリスク）の間に有意な正の相関が見られた（$r = 0.8558$，$p < 0.0001$）。

今回の調査により，MRIの安全運用に関して，十分な対策が取られていない実態が明らかとなった。MRI安全に関して，学会などで教育や周知を徹底する必要がある。

臨床MRI安全運用のための指針

上記全国調査の結果を踏まえ，日本磁気共鳴医学会と日本医学放射線学会は，日本放射線技術学会，および日本磁気共鳴専門技術者認定機構の協力の下に，「臨床MRI安全運用のための指針」[3]を設定した。

以下に，本指針の内容を記載する。

1. 安全管理体制

施設内にMRI検査を管理するチーム（安全管理責任者*1・安全管理担当者*2チーム）を作ること。本チームは1名の責任医師の下，そのほかの医師，診療放射線技師もしくは臨床検査技師，看護師などで構成される。その構成員には磁気共鳴専門技術者あるいはそれに準ずる者が含まれることが望ましい。本チームの会合は年1回以上行い，施設内での医療従事者への講習を定期的に行うこと。また，安全管理責任者や安全管理担当者は，MRIの関連団体にて安全性に関する講習会に年1回程度，定期的に参加することが望ましい。

2. MRI検査前の安全管理

MRI検査前における患者および医療従事者への安全管理の体制を構築すること。体内植込み型医療機器，体内外金属，入れ墨などを問診票のほか患者の医療機器情報カードや金属探知機などを用いて検査前に把握し，身体への悪影響（臓器損傷や熱傷など）を与える恐れがあるものを適切に管理すること。また，医療従事者および作業従事者*3の金属持ち込みを防止する教育および管理体制（マニュアルづくりなど）を整備すること。MRI検査に重要な情報を共有する医師，診療放射線技師もしくは臨床検査技師，看護師との連携体制を整えること。

3. MRI検査中の安全管理

検査中は患者の状態を監視し，必要に応じて，心拍数，血液酸素飽和度などの観察を行い，患者からの中止要請（患者緊急コール）を伝えるシステムを利用した運用体制を整えること。緊急時のバックアップ体制を構築し，運用マニュアルを整備すること。

4. 安全性情報の関連学会・関連行政機関への報告を行う体制整備

安全性情報の関連学会・関連行政機関への報告を行う体制を整備すること。安全性情報に関しては，関連学会，関連行政機関のホームページ（https://www.pmda.go.jp/safety/reports/hcp/pmd-act/0003.html）などを参考とすること。

5. 鎮静の必要な患者の安全管理

小児や閉所恐怖症の患者を含め鎮静の必要な患者に対しては，緊急時のバックアップ体制を構築すること（小児の場合は「MRI検査時の鎮静に関する共同提言」*4を推奨）。

6. 造影剤使用の安全管理

MRI造影剤の使用においては同意書を取得すること。MRI造影剤の副作用への対応，腎性全身性線維症（NSF）防止の対策の教育や対応へのマニュアルを備えていること。また，安全管理責任者や安全管理担当者は，MRI造影剤に関する講習会に定期的（少なくとも2年に1回）に参加し，MRI造影剤使用上の注意改訂など，重要な情報の周知を図ること。

7. MRI装置の品質管理

始業時・終業時点検ならびに保守点検を適宜実施すること。また，始業時にはファントムなどの撮影を行い，画質の維持・向上に努めること。なお，定期的（少なくとも6か月に1回）に保守点検が行われていることが望ましい。

8. 非常時の安全管理

患者の安全確保，液体ヘリウムの突沸（クエンチ）への対応，地震・火災・浸水・停電などの災害への対応のマニュアルを備えていること。

◎

MRI安全運用に関する全国調査の結果を踏まえ，「臨床MRI安全運用のための指針」が設定された。本指針に準じて管理することで，MRI検査がすべての国民に対してより安全に，精度高く実施されることが期待される。なお，本指針での安全管理を広く実施させるため，令和2年度の診療報酬改定で，画像診断管理加算2および3に関する施設基準に「関連学会の定める指針に基づいて，MRI装置の適切な安全管理を行っていること」[4]が明記された。

〈謝辞〉
平成30年度厚生労働行政推進調査事業費（地域医療基盤開発推進研究事業）「MRI装置の安全な運用に関する調査研究」にご尽力いただいた順天堂大学・青木茂樹先生，隈丸加奈子先生，慶應義塾大学・陣崎雅弘先生，琉球大学・村山貞之先生，および本研究の論文執筆を担当した宮崎大学・東　美菜子先生，Zaw Aung Khant先生，DataRobot社の伊地知晋平氏に感謝申し上げます。
日本磁気共鳴医学会安全性評価委員会のアドホック委員会「臨床MRI安全運用のための指針作成委員会」で本指針作成にご尽力いただいた順天堂大学・青木茂樹先生，金沢大学・宮地利明先生，東海大学・黒田　輝先生，滋賀医科大学・渡邊嘉之先生，北海道大学・工藤與亮先生，岐阜大学・松尾政之先生，弘前大学・掛田伸吾先生，名古屋大学・田岡俊昭先生，熊本大学・米田哲也先生，東京慈恵会医科大学・豊田圭子先生，産業医科大学・林田佳子先生，川崎医療福祉大学・小野　敦先生，山梨大学・本杉宇太郎先生，江田クリニック・内田幸司先生，神戸大学・京谷勉輔先生に，この場を借りて感謝申し上げます。

●参考文献

1）MRI安全性の考え方 第2版．日本磁気共鳴医学会安全性評価委員会 監修，学研メディカル秀潤社，東京，2014.
2）Azuma, M., Kumamaru, K.K., Hirai, T., et al.: A National Survey on Safety Management at MR Imaging Facilities in Japan. *Magn. Reson. Med. Sci.*, 2020（Epub ahead of print）.
3）日本磁気共鳴医学会：臨床MRI 安全運用のための指針．2020.
http://www.jsmrm.jp/modules/other/index.php?content_id＝5
4）保医発0305 第3号　特掲診療料の施設基準等及びその届出に関する手続きの取扱いについて（2020年3月5日）.
https://www.mhlw.go.jp/content/12400000/000603894.pdf

＊1 安全管理責任者は，施設内にてMRI検査の安全管理を統括する医師を指す。
＊2 安全管理担当者は，施設内にてMRI検査の安全管理を担当する医師，診療放射線技師，もしくは臨床検査技師，看護師を指す。
＊3 MRI装置のメンテナンス関係者および室内の修繕などのために検査室内に立ち入る作業者を指す。
＊4 MRI検査時の鎮静に関する共同提言（日本小児科学会・日本小児麻酔学会・日本小児放射線学会，2013年）。